Master's thesis

Materials research

Inorganic materials

Wet chemical etching of AlN and $Sc_{0.2}Al_{0.8}N$ thin films

Konsta Airola

2022

Supervisors: James Dekker, Mikko Ritala

Examiners: Mikko Ritala, Matti Putkonen

University of Helsinki
Faculty of Science

HELSINGIN YLIOPISTO
HELSINGFORS UNIVERSITET
UNIVERSITY OF HELSINKI
MATEMAATTIS-LUONNONTIETEELLINEN TIEDEKUNTA
MATEMATISK-NATURVETENSKAPLIGA FAKULTETEN
FACULTY OF SCIENCE

Tiedekunta – Fakultet – Faculty	Koulutusohjelma – Utbildningsprogram – Degree programme
Faculty of Science	Master's programme of materials research

Opintosuunta – Studieinrikting – Study track
Inorganic materials

Tekijä – Författare – Author
Konsta Petteri Airola

Työn nimi – Arbetets titel – Title
Wet chemical etching of AlN and $Sc_{0.2}Al_{0.8}N$ thin films

Työn laji – Arbetets art – Level	Aika – Datum – Month and year	Sivumäärä – Sidoantal – Number of pages
M.Sc. thesis	25.4.2022	82

Tiivistelmä – Referat – Abstract

Aluminium nitride is a piezoelectric material commonly used in piezoelectric microelectromechanical systems (MEMS) in the form of thin films deposited by sputtering. AlN-based devices are found in wireless electronics in the form of acoustic filters, but they also have prospective applications in a wide variety of sensor systems. To enhance the piezoelectric properties of AlN, some of the Al can be replaced with scandium, which is required for next-generation devices. However, addition of Sc makes both the deposition and patterning of the film more difficult.

This work focuses on patterning of AlN and $Sc_{0.2}Al_{0.8}N$ thin films with wet etching. Both materials are etched anisotropically, which in theory enables etching the materials with little deviation from the mask dimensions. However, in practise, undercutting at the mask edges occurs easily making the structures narrower compared to the etch mask.

This work investigates and compares the mechanisms and etch rates of AlN and $Sc_{0.2}Al_{0.8}N$. Tetramethyl ammonium hydroxide was mostly used for etching, but also H_3PO_4 and H_2SO_4 were tested. Addition of 20 atom-% Sc lowered the etch rate of the material and resulted in more undercutting. The causes behind mask undercutting were examined by using 11 differently deposited etch masks, and the undercutting was minimized by optimizing the mask deposition, using thermal annealing, and optimizing the etching temperature. Finally, the work identifies and discusses the relevant factors in depositing and patterning the AlN, $Sc_xAl_{1-x}N$ and mask films.

Avainsanat – Nyckelord – Keywords
AlN, ScAlN, thin film, wet etching, MEMS, sputtering

Säilytyspaikka – Förvaringställe – Where deposited
E-thesis

Muita tietoja – Övriga uppgifter – Additional information
This thesis was done at VTT Technical Research Centre of Finland Ltd

Preface

This work was conducted at VTT Technical Research Centre of Finland Ltd as a part of the project *Beyond SOI* funded by VTT and Business Finland.

I'd like to thank James Dekker for supervising the work, feedback on the thesis and many helpful discussions along the way. A large thank you to professor Mikko Ritala not only for feedback on the thesis, but for teaching many courses and a lot of other support during my studies. I certainly wouldn't be here without him. I am also extremely grateful to Tomi Salo and Tuomas Pensala for giving me the opportunity to work on this project and for always being supportive and trusting. Thanks to Stefan Mertin and Enni Hartikainen for doing most of the AlN, $Sc_{0.2}Al_{0.8}N$ and Mo thin film depositions as well as many discussions related to the topic. Thanks to Abhilash Thanniyil Sebastian for some of the film depositions and for guidance with many of the processing steps. Thanks to Jari Likonen and Kenichiro Mizohata for performing SIMS and ERDA measurements, respectively. Kristiina Rutanen and Kirsi Järvi deserve a thank you as well for doing PECVD, ALD and lithography steps. Thanks to Marcelo Rizzo Piton for assistance with EDX measurements. Finally, a big thanks to all other VTT Micronova personnel for giving me tool trainings, helping with tool-related issues or any other questions, and being good co-workers. Finally, I'd like to thank my family for supporting my endeavours over the years. Without their support, I would hardly be here today.

Konsta Airola

List of abbreviations

AC	Alternating current
ALD	Atomic layer deposition
ALE	Atomic layer etching
AOG	Abnormally oriented grain
BAW	Bulk acoustic wave
BHF	Buffered hydrogen fluoride
CCP	Capacitively coupled plasma
CMUT	Capacitive micromachined ultrasonic transducer
CRF	Coupled resonator filter
CVD	Chemical vapour deposition
DC	direct current
DI	De-ionized
DMD	Digital micromirror device
DRIE	Deep reactive ion etching
EDTA	Ethylenediaminetetraacetic acid
EDX	Energy-dispersive X-ray spectroscopy
HDMS	hexamethyldisilazane
IBE	Ion beam etching
ICP	Inductively coupled plasma
IDT	Interdigital transducer
LIDAR	Light detection and ranging
MBE	Molecular beam epitaxy
MEMS	Microelectromechanical systems

MOCVD	Metalorganic chemical vapour deposition
PECVD	Plasma-enhanced chemical vapour deposition
PLD	Pulsed laser deposition
PMUT	Piezoelectric micromachined ultrasonic transducer
PVD	Physical vapour deposition
PZT	Lead zirconate titanate
RF	Radio frequency
RIE	Reactive ion etching
SAW	Surface acoustic wave
SC-1	Standard clean 1
SEM	Scanning electron microscope
SIMS	Secondary ion mass spectrometry
TEOS	Tetraethyl orthosilicate
TMAH	Tetramethyl ammonium hydroxide
TOF-ERDA	Time-of-flight elastic recoil detection analysis
UV	Ultraviolet
XRD	X-ray diffraction

Table of Contents

1. Introduction

Aluminium nitride (AlN) and scandium aluminium nitride ($Sc_xAl_{1-x}N$) are piezoelectric materials which are highly interesting for applications in piezoelectric microelectromechanical systems (piezo-MEMS). The main application of these materials is in acoustic filters for telecommunications, but many other MEMS devices based on them are emerging. Replacing some of the aluminium with scandium increases the piezoelectric properties, but it also makes the deposition and patterning of the films more challenging. The aim of this thesis was to develop a patterning process for $Sc_xAl_{1-x}N$.

The literature review starts with a discussion on the properties of AlN and $Sc_xAl_{1-x}N$. Then the basics of wet and dry etching processes are introduced. Next, the application of plasma-based chemical processes for etching and depositing materials are discussed. Deposition of AlN and $Sc_xAl_{1-x}N$ thin films with reactive magnetron sputtering is described briefly, and their etching is discussed in detail. Together these chapters cover the basic information required for understanding the results presented in the experimental section. Finally, applications of $Sc_xAl_{1-x}N$ thin films are discussed. For a more in-depth discussion on the deposition and properties of the $Sc_xAl_{1-x}N$ and molybdenum films similar to those used in this work, the reader is referred to Enni Hartikainen's M.Sc. thesis.[1]

The focus of the experimental work was the development of wet etching processes for $Sc_xAl_{1-x}N$ thin films deposited with reactive magnetron sputtering. $Sc_xAl_{1-x}N$ can be etched with both acidic and alkaline solutions. For this study, solutions of tetramethyl ammonium hydroxide (TMAH), H_3PO_4 and H_2SO_4 were chosen. The primary research questions were:

1. How does the addition of ScN to AlN change the etching properties of the material?
2. How can $Sc_xAl_{1-x}N$ be etched as anisotropically as possible?

The majority of the results presented in this thesis have been already published.[2]

2. Structure and properties of AlN and $Sc_xAl_{1-x}N$

AlN is an inorganic material with the hexagonal wurtzite crystal structure which exhibits piezoelectricity. When strain is applied to a piezoelectric crystal, an electric field is generated in the crystal resulting in a voltage between the opposing surfaces. The effect also works in the converse: a voltage applied to the crystal causes stress and strain (Figure 1). Some of the most common applications of piezoelectric materials are quartz crystal resonators found in timing applications such as quartz clocks, piezoelectric crystals in lighters for spark generation, and ultrasonic elements in sonars and in medical ultrasound imaging.

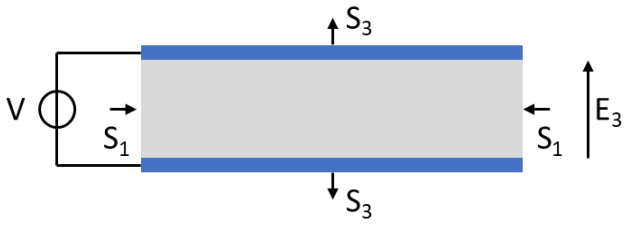

Figure 1. A schematic displaying the strain in a piezoelectric material in an electric field.

The structure of AlN consists of Al- and N-ions with slightly distorted tetrahedral coordination.[3] In Figure 2a, the bond between atoms 1 and 3 is slightly longer compared to bond between atoms 3 and 4. Lattice constants of AlN are a = 3.11 Å and c = 4.98 Å. AlN is rotationally symmetrical threefold along the c-axis but it cannot be inverted along the a-axis. Compressing the structure of AlN along the c-axis causes the positively charged Al-ions and the negatively charged N-ions to move to the opposite directions, which results in the generation of the electric field. This is likely due to rotation of the bonds and the bond lengths are not changed significantly. The ions are also moved sidewards, but due to the symmetry, no electric field is generated perpendicular to the c-axis.

The (0001) and (000–1) surfaces of AlN are structurally and chemically different due to the directionality of the material. Starting from the surface, if the bond along the c-axis goes from Al to N, that is the N-polar (000–1) surface. The (0001) surface is called Al-polar, or III-polar in the case of other nitrides with the same structure. Under compression along the c-axis, the Al-polar surface is charged negatively, while the opposite is true for the N-polar surface (Figure 2b).

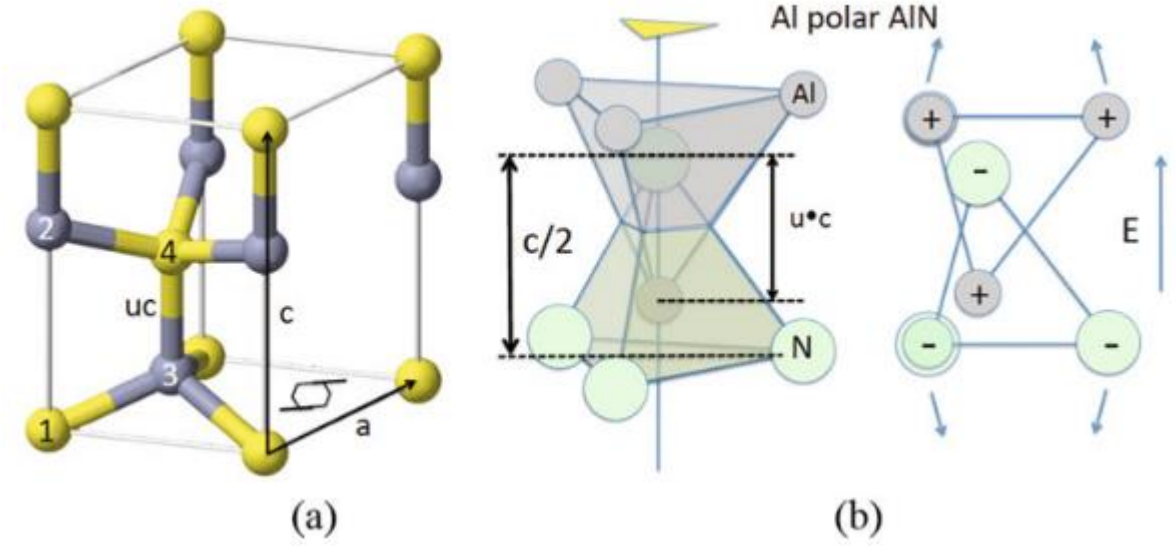

Figure 2. (a) Crystal structure of AlN, (b) a diagram showing the polarity of the structure and the deformation under an electric field. Adapted from[3], copyright 2017 Springer International Publishing.

AlN is a very thermally stable material with a melting point of approximately 2200 °C.[3] The bandgap of AlN is 6.15 eV making it an insulator. AlN also has high hardness, high sound velocity and its thermal conductivity is extraordinarily high at 3.19 W/cmK, exceeding that of most metals.[4] These properties make AlN especially well-suited for use in acoustic filters, which are described in detail in Chapter 8.1.

For each piezoelectric material, the strength of the piezoelectric effect depends on its rigidity, piezoelectric polarizability, and permittivity. The various piezoelectric coefficients originate from these. There are several different piezoelectric constants for each material which are typically described as tensors. For AlN, there are three independent piezoelectric coefficients: e_{33}, e_{31} and e_{15}. e_{33} describes the stress along the c-axis when the electric field is applied along the same axis. e_{31} describes the stress perpendicular to the c-axis with the electric field along the c-axis. e_{15} corresponds to shear stress when the electric field is perpendicular to the c-axis. Deformations along the c-axis or perpendicular to it are the most commonly utilized modes, and those coefficients can readily be measured from thin films sandwiched between electrodes. For films on a substrate, the coefficients are denoted with a suffix f. For the longitudinal effect, the strain coefficient $d_{33,f}$ is typically used. $d_{33,f}$ can be determined by compressing the film and measuring the generated voltage, while e_{31} can be determined by fabricating a cantilever and measuring its deflection as a function of applied voltage.

$d_{33,f}$ is defined as

$$d_{33,f} = e_{33}/c_{33}^{E}, \quad (1)$$

where $c_{33}^{E}$is stiffness along the longitudinal axis in a constant electric field. The stress caused by applying an electric field to a piezoelectric material is

$$T = Sc - eE, \quad (2)$$

where T is stress, S is strain, and E is the electric field.[5] If the material is not clamped and can deform freely, the stress is zero, and the strain along the longitudinal axis is

$$S_3 = e_{33}E_3/c_{33} = E_3 d_{33}, \quad (3)$$

and perpendicular to it

$$S_1 = e_{31}E_3/c_{11}. \quad (4)$$

The electromechanical coupling coefficient k^2 describes how much of the electric energy is transformed to mechanical energy by a piezoelectric material or by a piezoelectric device. For AlN, it can be up to 7 %, while it is of course lower for devices.[3] The coupling coefficient is very similar for single-crystal and high-quality polycrystalline AlN.

The piezoelectric effect of AlN can be increased by substituting some of the Al with other elements. Scandium has so far been the most promising, but other interesting approaches include using for example yttrium[6], ytterbium[7], tantalum[8], or using two elements, such as magnesium and titanium, zirconium, hafnium or tantalum.[9] The high piezoelectric response of $Sc_xAl_{1-x}N$ was first demonstrated by M. Akiyama. *et. al* in 2009.[10]

The piezoelectric response of $Sc_xAl_{1-x}N$ increases with increasing Sc-concentration as long as the material remains in the metastable wurtzite crystal structure. According to calculations, the wurtzite structure is no longer metastable at x = 0.64 and it transforms to the cubic rock salt structure of ScN, which is no longer piezoelectric.[11] However, deposition of $Sc_xAl_{1-x}N$ films with x = 0.64 and a well-ordered wurtzite structure is practically impossible. The cubic phase begins to appear around x = 0.4–0.45, which has been the limit for high-quality films. Even small cubic grains degrade the microstructure of the film, which is discussed in Chapter 5. Compared to pure AlN, at high Sc-levels of x = 0.40–0.45 the longitudinal piezoelectric coefficient $d_{33,f}$ is increased from 8.4 pC/N to approximately 27 pC/N.[10,12,13] The transversal piezoelectric coefficient $e_{31,f}$ is increased from –1.05 C/m^2 up to –3.16 C/m^2.[14] The

electromechanical coupling coefficient is also increased by the addition of Sc, and it has been calculated to reach 15 % at x = 0.3.[15]

Addition of Sc increases the lattice constant *a*, but it has little effect on the lattice constant *c*.[16] Also, Sc is a larger ion and it is typically found in sixfold coordination instead of the fourfold coordination in AlN, which results in a frustrated system.[17] Together these effects reduce the stiffness of the material, which results in the larger piezoelectric effect due to the reduced resistance to deformation. High Sc-content also makes the material ferroelectric, meaning the polarity of the material can be changed by applying a strong electric field across it.[18]

Addition of Sc also modifies some other properties of AlN significantly. With increasing x, $Sc_xAl_{1-x}N$ is more prone to oxidation on the surface and in the grain boundaries.[13,19] Exposure to atmospheric air can cause four times more surface oxidation at x = 0.44 compared to AlN resulting in a native oxide layer thickness up to 10–15 nm.[13,19] Addition of Sc also decreases the bandgap linearly from approximately 6.15 eV for pure AlN to 2.94 eV at x = 0.34.[16]

3. Etching of materials in microfabrication

Deposition and patterning of various materials are the two basic steps that are repeated over and over again to fabricate any MEMS device. The various patterning steps define the final dimensions of the device. In addition to other patterning techniques, such as area-selective deposition, accurate etching methods are necessary for the ever-shrinking devices. Etching can be done with chemical solutions in wet etching or with gases and vapours in a variety of gas-phase etching techniques. Dry etching typically refers only to plasma-based etching techniques, although other gas-phase etching techniques are available, which makes the terminology quite confusing.

Etching of materials starts with lithography. First, a thin layer of resist is coated on a wafer surface. Resists are typically organic polymers with good thermal stability and high resistance to etching processes. Resist thicknesses vary from tens of nanometres to tens of micrometres depending on the application. The resist is sensitive to some external stimuli, which enables its patterning. Photolithography is the most common technique where the photoresist is sensitive to ultraviolet (UV) light. Selected areas of the resist are exposed to the light, through a photomask for example, and developed with a suitable solvent or solution. There are two types of resists: positive-tone and negative-tone resists. With positive resists, the exposed area

becomes more soluble in the developer, while with negative resist the exposed area is hardened and becomes insoluble.

After the resist is patterned, it acts as an etching mask and the pattern is transferred to the underlying material by etching. Reactive ion etching (RIE) is the most common gas-phase etching technique, and it is discussed in detail in the next chapter. Some other etching techniques are for example ion beam etching (IBE), which uses ion bombardment to erode material, atomic layer etching (ALE), which enables etching of materials one atomic layer at a time, and hydrogen fluoride (HF) vapour and XeF_2 vapour etching which are used to etch SiO_2 and Si, respectively. Common examples of wet etching include etching of Al with a mixture of H_3PO_4, HNO_3 and acetic acid, etching of SiO_2 with buffered hydrofluoric acid (BHF, a 1:7 mixture of 50 % HF and 45 % NH_4F), and etching of Si with potassium hydroxide (KOH) or tetramethyl ammonium hydroxide (TMAH).

The photoresist is often a suitable etch mask for patterning thin layers with RIE and for some wet etching processes. However, sometimes it is necessary to etch the pattern first to an intermediate hard mask before etching the pattern into the target material. Utilizing a hard mask increases the selectivity of the etching process. Any compound or metal can be used as a hard mask in principle, some common examples being SiO_2 and Cr.

The most important factors in an etching process are the uniformity, selectivity, and the resulting profile after etching of the material. Etch processes should be as uniform as possible to enable precise patterning across entire wafers. This helps ensure similar performance between fabricated devices. Selectivity of etching is the etch rate of the target material compared to the etch rate of the other exposed materials (Figure 3c). The selectivity to the mask material should be quite high to enable the use of thin mask layers, as thinner masks enable higher resolution and lower roughness. High selectivity to the bottom layer is also often important (Figure 3d). Many etching processes require some over etching to ensure full patterning of the film, but the etch should not attack the material below too rapidly.

Etching processes can be isotropic or anisotropic (Figure 3a, b). Isotropic etch processes etch material evenly in every direction, while anisotropic etching proceeds ideally in one direction only. Most wet etching processes are isotropic, while most RIE processes are anisotropic. Anisotropic processes are obviously preferred for high-fidelity patterning. Isotropic etching processes will etch material laterally from below the mask material, which is called

undercutting. Sidewall angle is the angle between the substrate plane and sidewall. For ideal anisotropic etching it is 90 °.

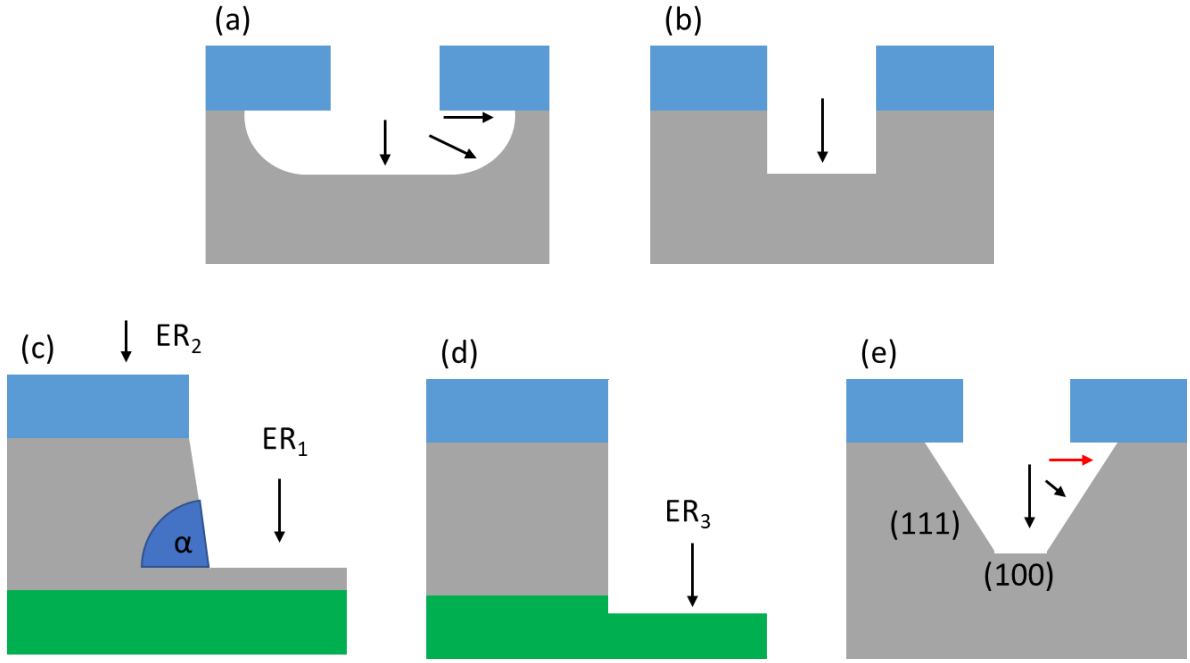

Figure 3. (a) Ideal isotropic etching proceeds evenly in every direction. (b) Ideal anisotropic etching proceeds one direction. (c) Anisotropic etching with a sidewall angle α. The selectivity between etching of the target material and the mask is ER_1:ER_2. (d) Etching into underlying the material with and etch rate ER_3. (e) Wet etching defined by crystalline planes, mask undercut due to interface defects is highlighted with red.

Wet etching of Si with KOH or TMAH is an important example of anisotropic wet etching and it is widely used for fabrication of various structures and devises from Si.[20] Different crystalline planes of Si have different reactivities leading to different etch rates (Figure 3e). Si{110} planes are etched very rapidly, while the etch rate of {111} planes is the slowest, and etch rate of {100} planes is intermediate.[21] Activation energies for the etching of the different planes is also different, with the activation energy for etching {111} planes being the highest.[21] Etching of Si thus forms structures defined by the {111} planes while the other planes are etched away. This results in a sidewall angle of 57.74 °. Etching of AlN and $Sc_xAl_{1-x}N$ with alkaline and acidic etchants is also anisotropic. Despite the name, anisotropic wet etching often results in some mask undercut. It can for example be caused by etching of the most stable plane, or by defects at the interface between the mask and the etched material.

Wet etching and dry etching have the almost opposite pros and cons. Wet etching is typically quite cheap and large batches of wafers can be processed at the same time. Wet etching solutions

are often highly selective towards the desired material. The largest disadvantage is that wet etching is typically isotropic, so the sidewall angle is difficult to control, and undercutting causes the pattern to deviate from the mask. Also, capillary forces can be an issue in wet etching, and they can cause very fine features to collapse or stick to each other. Finally, the high selectivity of wet etching can cause unreliability in initiation of the etching if native oxide or other residues are present. On the other hand, dry etching techniques require expensive equipment. In RIE and IBE, typically only a single wafer can be processed at a time, and the selectivity can be an issue, as they will etch various materials quite rapidly. However, with RIE and IBE, undercutting rarely occurs and the sidewall angle can be controlled by tuning the etch recipe. ALE and other chemical vapour etching techniques lie in between. They require expensive equipment, but they can be built to accommodate large batches. They are isotropic but no capillary forces are present, which enables some unique applications such as etching of narrow cavities.

4. Reactive ion etching and plasma enhanced chemical vapour deposition

Chemical plasma processing techniques are crucial for the modern semiconductor industry. Reactive ion etching (RIE) enables precise anisotropic etching of many materials which makes it a necessity in the fabrication of almost every semiconductor device. Plasma enhanced chemical vapour deposition (PECVD) enables deposition of various materials from less reactive precursors or at lower temperatures compared to thermal chemical vapour deposition (CVD). PECVD is also a very widely used technique, especially for the deposition of SiO_2 and SiN_x thin films.

In this chapter, the basics of the plasma processing equipment and plasma generation are discussed. Then RIE is discussed in more detail, with an explanation of the various gases used, as well as a brief discussion on the different mechanisms involved in RIE. Finally, basics of PECVD are introduced. Both techniques were used in the experimental work.

4.1. Plasma processing equipment

Plasma processes are low to medium vacuum technologies, with pressures ranging from 1 mbar to $1*10^{-3}$ mbar. Process gasses are admitted to a process chamber while the chamber is also

pumped at a high rate to achieve the desired pressure. Electric fields are applied to the system, which causes partial ionization of the gas. The electrons and ions are accelerated to high speeds generating a glow discharge. The power can be applied either in the form of direct current (DC), alternating current (AC) at radio frequency (RF), or microwaves. In PECVD and RIE, the power is typically generated by a 13.56 MHz RF power source. The high frequency alternating electric field does not significantly affect ions, but it accelerates electrons to high speeds. The electrons collide with neutral gas molecules which can be ionized or split to radicals. The fast-moving electrons also collide with the chamber walls that are thereby charged negatively compared to the plasma. This generates a DC component between the plasma and the electrodes, which accelerates the ions to the substrate.

Two types of plasma sources are commonly used in RIE and PECVD: capacitively coupled plasmas (CCP) and inductively coupled plasmas (ICP).[22] The main practical difference between the plasma sources is that in the CCP the electron paths are straight, while in the ICP the electron paths are circular and thus much longer. This allows lower pressures while still sustaining the plasma and the degree of ionization in ICP systems is 100-1000 times larger compared to CCP systems.[22] ICP is also called high-density plasma, while CCP is referred to as low-density plasma. The main advantage of the lower pressure in the ICP is that the ions accelerated towards the substrate collide and scatter less due to the lower pressure. The ion bombardment is more energetic and perpendicular to the substrate surface, which results in faster etching and reduces the effect of the aspect ratio on the etch rate.

A CCP system consists of an electrode on which the substrate is placed (figure 4). The electrode is powered, while the rest of the chamber is connected to the ground. The electrode is further separated from the power source with a capacitor, which acts as a closed circuit for the high-frequency AC voltage, but as an open circuit to the DC component. This enables the DC voltage to reach –100 to –1000 V during normal plasma processes. This voltage is called either as the DC bias or the RF bias.

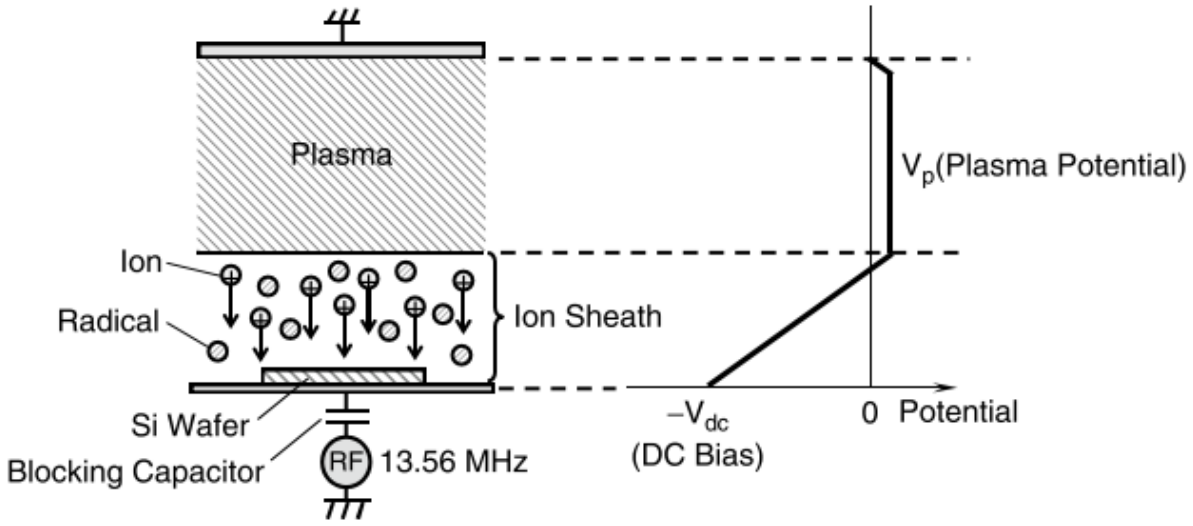

Figure 4. The structure of a CCP system with the potential plotted as a function of the chamber position. Adapted from[22], copyright 2015 Springer International Publishing.

In an ICP system (Figure 5), the plasma is generated by a coil placed outside the chamber. Applying RF-power to the coil induces magnetic fields, which in turn induces a circular current in the plasma. A separate bottom electrode is used like in the CCP system. Power applied to this electrode controls the DC bias independently of the ICP power. This allows better control over the DC bias and ion current compared to the CCP.

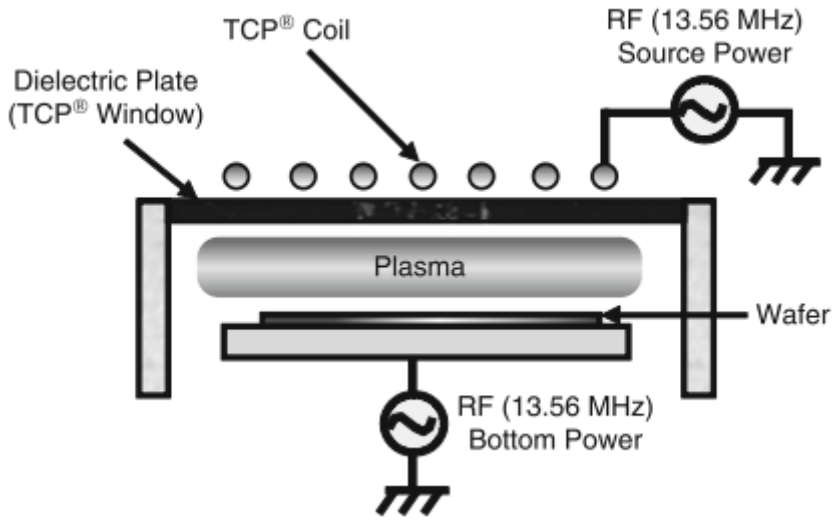

Figure 5. The structure of an ICP-RIE. TCP refers to transformer coupled plasma, which an ICP using a planar coil instead of a helical coil. Adapted from[22], copyright 2015 Springer International Publishing.

4.2. Reactive ion etching

In RIE, materials are etched via a combined effect of reactive radicals and ion bombardment. RIE is widely used as it enables anisotropic patterning of many materials which would not be possible with wet etching. If no ion bombardment is directed towards the substrate, the technique is known as plasma etching, although the terms RIE and plasma etching are often used interchangeably.

In RIE, gases admitted to the chamber form reactive radicals and ions due to the collisions with the electrons. The radicals move randomly while the ions are accelerated towards the substrate by the DC bias. Etching by radicals only would lead to a formation of volatile species on the surface and isotropic etching. Pure ion bombardment on the other hand would lead ideally to anisotropic etching by causing ejection of atoms from the target material, which is called sputtering. The combination of chemical reactions and ion bombardment leads to enhanced etch rates and anisotropic profiles.

There are four basic steps that are involved in etching with RIE: generation of reactive species, their adsorption on the substrate, reaction between the adsorbed species and the substrate, and desorption of the products.[22] Any of them can be etch rate limiting depending on the process. Ion bombardment can assist with generating adsorption sites, with driving the reactions on the surface or with the desorption of the products.

A wide variety of gases are used in RIE, and a specific mixture of them is used in each application to tune the etch rate, selectivity, and sidewall profile. The most important ones and their functions are described here briefly. Ar and sometimes He are used as inert gases. They do not react but they contribute to the ion bombardment. CF_4, SF_6 and NF_3 act as fluorine source gases. They dissociate easily to form F-radicals which react with Si and some metals, such as Mo and W, to form volatile fluorides. Si etching with F-based plasmas is especially rapid and anisotropic, and thus not suitable for all applications. CHF_3 and C_4F_8 act also as F-sources, but their more important function is the generation of CF_2 and other C_xF_y radicals. The CF-radicals react on surfaces to form fluorocarbon polymer. This polymer forms mainly on the sidewalls as it is eroded from horizontal surfaces by the ion bombardment (Figure 6). This aids in getting the anisotropic etch profile by preventing radical reactions on the sidewalls. Cl_2 and BCl_3 are used in etching metals, such as Al, Cr, and others from groups 4–6, and their compounds. Cl_2 and HBr are also used especially for etching polysilicon with better control compared to F-based

plasmas. The main functions of O_2 and H_2 are controlling the plasma composition. H_2 scavenges F-radicals by forming HF, while O_2 reacts with carbon and sulfur releasing more F-radicals.

A good example of the different processes involved in RIE is comparing the etching of Si and SiO_2 in F-based plasmas.[23] SiO_2 is etched with gases containing C, H and F with Ar for additional ion bombardment. During etching, CF-species are deposited on the SiO_2 surface. Due to ion bombardment, these species react forming SiF_4, CO and CO_2. However, on Si-surfaces, the etching reaction is much slower due to the lack of oxygen, and a CF-polymer layer may begin to deposit instead. This enables a high etching selectivity between SiO_2 and Si. Si on the other hand can be etched very rapidly in plasmas which produce more F radicals and less CF-species.[22] In the deep reactive ion etching (DRIE) process, Si is etched with a gas containing SF_6 and O_2. This generates a large amount F-radicals which react very rapidly with Si but much less with SiO_2. Due to the isotropic nature of this etching, a separate CF-polymer deposition step based on C_4F_8 is applied. This protects the sidewall from etching. The process is cycled between the SF_6/O_2 and C_4F_8, which enables uniform etching through entire Si-wafers rapidly and with steep sidewall angles. The DRIE process is used for example in releasing MEMS devices from the substrate.

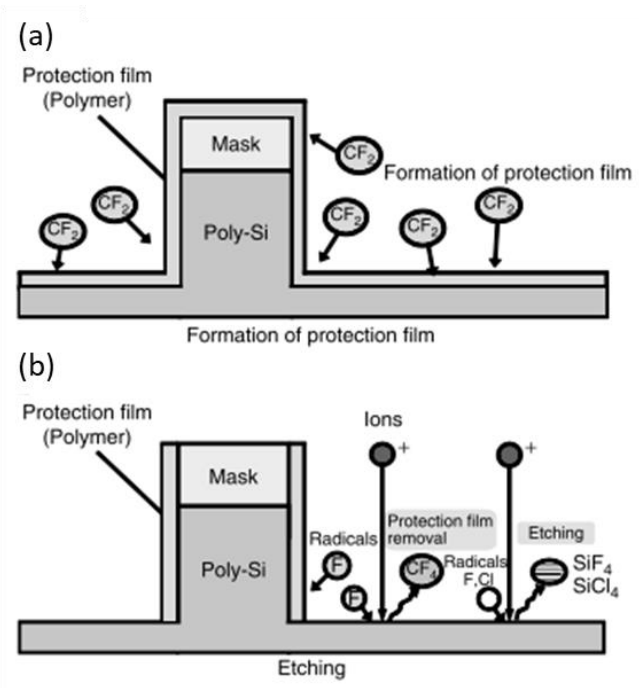

Figure 6. (a) Deposition of a fluorocarbon polymer. (b) Anisotropic etching where the polymer is removed from horizontal surfaces while the sidewall is protected by the polymer. Typically, polymer deposition and etching occur at the same time. Adapted from[22], copyright 2015 Springer International Publishing.

4.3. Plasma enhanced chemical vapour deposition

PECVD is especially used for the deposition of amorphous Si, SiO_2, SiN_x, SiC and diamond-like carbon. The main advantage of PECVD is that much lower deposition temperatures can be used compared to thermal CVD. Deposition temperature can be as low as 180 °C for PECVD SiO_2, while the temperature in thermal CVD of SiO_2 is around 700 °C. A disadvantage of PECVD-deposited films is that they contain large amounts of hydrogen and other impurities depending on the precursors.

For deposition of SiO_2 and SiN_x, SiH_4 is often used as the Si-precursor. The second precursor for SiO_2 is O_2 or N_2O, and for SiN_x, it typically is NH_3. Ar or N_2 is added as an inert gas for dilution and additional ion bombardment. Same principles apply in PECVD as in RIE. The precursors form more reactive radicals due to collisions with electrons in the plasma. These species are adsorbed on the surfaces and react to form the desired product. Ion bombardment enhances the reactions on the surface. However, due to the directional ion bombardment, often less deposition occurs on vertical walls compared to horizontal surfaces, meaning the step coverage can be poor. Pressures are typically higher in PECVD compared to RIE, and the plasma powers are lower.

SiO_2 is also often deposited with tetraethyl orthosilicate (TEOS) and O_2 as the precursors. TEOS-based SiO_2 offers better step coverage compared to the SiH_4-based SiO_2 but it requires higher temperatures.

5. Deposition of AlN and $Sc_xAl_{1-x}N$ thin films with sputtering

AlN and $Sc_xAl_{1-x}N$ thin films for MEMS applications are deposited almost exclusively with reactive magnetron sputtering. Other techniques are available for AlN, such as atomic layer deposition (ALD)[24], metalorganic chemical vapor deposition (MOCVD)[24], molecular beam epitaxy (MBE)[25] and pulsed laser deposition (PLD)[26], but these techniques are poorly suited for MEMS except for PLD. ALD typically results in films with poor piezoelectric response, MOCVD requires high temperatures and MBE is slow and best suited for deposition on single-crystal substrates. However, deposition of $Sc_xAl_{1-x}N$ with these techniques is being developed for other applications.[27–29]

Sputter deposition, or often just sputtering, is a physical vapor deposition (PVD) technique. It is commonly used for depositing thin films of various metals and their compounds. Sputtering enables depositing a wide range of materials with a single tool, the films are often dense and have good crystalline quality even at low deposition temperatures, and optimizing the film deposition is usually fairly simple.

In sputtering, a target consisting of a metal, a metal alloy or an inorganic compound is bombarded with ions from a plasma discharge. The ions colliding with the target cause atoms to be sputtered from it. The sputtered atoms land on the substrate resulting in thin film growth. Mainly Ar is used as the sputtering gas, but if a reactive gas, such as O_2 or N_2 is introduced to the plasma, it will react with the target and the film being deposited. The reactive gas forms the respective compound on the target surface, but still a large portion of the material is sputtered as single atoms, and the final compound formation occurs on the substrate surface.[3]

The structure of a magnetron sputtering system is similar to the CCP system described earlier, but the main power is applied to the target instead of the substrate (Figure 7). Magnets are placed behind the electrode, which results in magnetic fields perpendicular to the electric field. This causes the electrons paths to curve leading to more collisions between the electrons and the gas molecules. This results in a higher degree of ionization in the plasma, and lower pressures can be used. Power source in magnetron sputtering is typically DC, pulsed DC or RF. A second smaller RF power source is connected to the substrate, which causes a small DC bias voltage towards it. This results in some ion bombardment also towards the film being deposited, which helps controlling the structure and stress of the film.

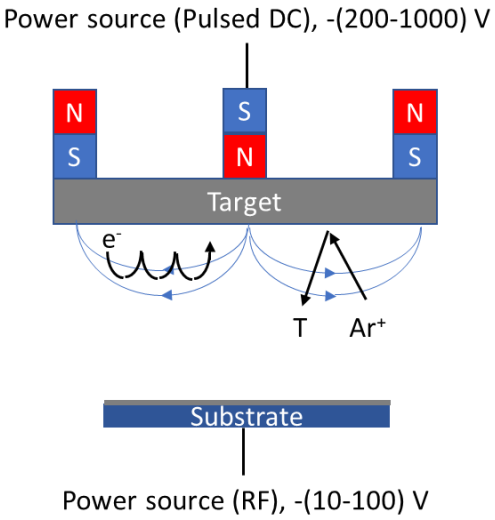

Figure 7. A schematic of the magnetron sputtering system used in this work.

Sputtering processes are often single wafer processes, but the deposition rates are relatively high. Typical deposition rates in microelectronics fabrication are in the range of 1–5 nm/s depending on the material and the deposition power.

Deposition of AlN and $Sc_xAl_{1-x}N$ under the proper conditions yields polycrystalline films consisting of columnar grains, all of the which are oriented in the <0001> direction with the same polarity. However, the addition of Sc makes the deposition of well oriented films considerably more difficult due to the formation of abnormally oriented grains (AOGs) (Figure 8). AOGs have the correct wurtzite structure but they are misoriented in relation to the original {0001} texture. The number of AOGs increases with the Sc content and they do not occur in AlN.[30] AOGs can originate from the substrate interface or nucleate during the film growth.[19] Nucleation of AOGs in the middle of the film is likely caused by accumulation of Sc in the grain boundaries, where it can then form cubic grains.[19] New misoriented wurtzite $Sc_xAl_{1-x}N$ grains then nucleate on these cubic grains. The AOGs grow faster compared to the rest of the film and become wider and more prominent with increasing film thickness. Formation of AOGs degrades the piezoelectric properties of the film, which consequently reduces device performance.[31,32]

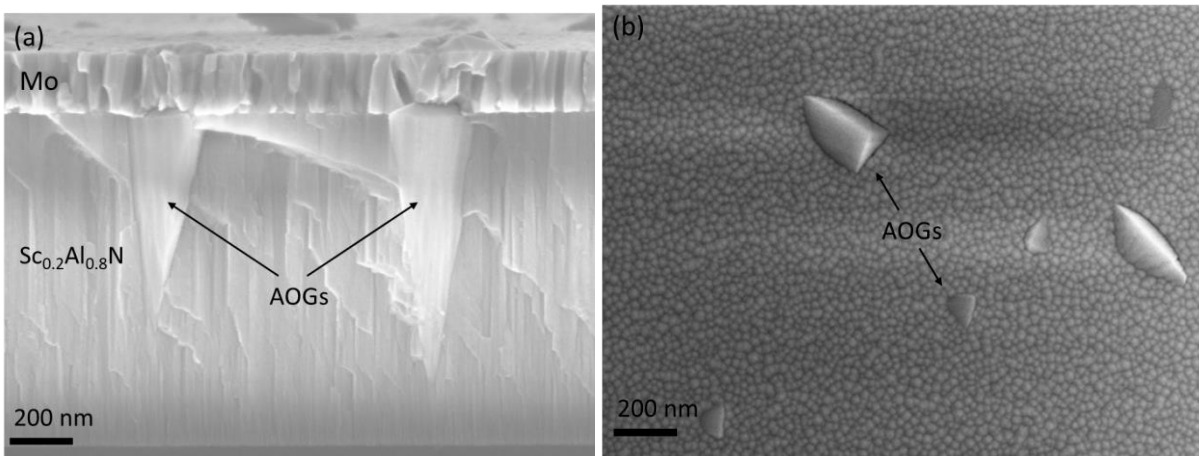

Figure 8. (a) Cross-sectional image of AOGs in a $Sc_{0.2}Al_{0.8}N$ film with a Mo top electrode, (b) top-down image of a $Sc_{0.2}Al_{0.8}N$ film with AOGs.

Deposition of high-quality $Sc_xAl_{1-x}N$ films also requires a suitable substrate material. The substrate and its microstructure can have a significant effect on the structure and properties of the $Sc_xAl_{1-x}N$ films.[33,34] $Sc_xAl_{1-x}N$ can be deposited directly on Si (100) but typically a metallic bottom electrode is required. The most common metal is Mo, but Pt is also used. The bottom electrode is grown on a sub-layer to control its microstructure and increase its adhesion to the substrate. For Mo, AlN and Ti are common sub-layer materials.[33,34]

AlN and $Sc_xAl_{1-x}N$ are deposited in approximately 1:2 Ar:N_2 atmosphere to ensure formation of a stoichiometric nitride. $Sc_xAl_{1-x}N$ can be either deposited using an Al-Sc alloy target, or by reactive co-sputtering. In co-sputtering, two separate targets consisting of different materials are used. The sputtering power can be controlled for each target individually which enables controlling the composition of the deposited film. This is extremely useful for depositing $Sc_xAl_{1-x}N$ with varying x for research purposes. For mass production, single-target deposition is preferred because the deposition rate with co-sputtering is typically much lower due to the smaller target sizes which limits the sputtering power. With the tool used in this work, the co-sputtering deposition rate was only about 1/5 compared to the single-target deposition rate.

Evolution of thin film structure during deposition can be explained with structure zone models. These are qualitative models, where the film microstructure is depicted as a function of the deposition temperature of the material compared to the melting temperature. In addition to temperature, many other factors can affect the resulting microstructures. Different structure zone models have been developed, an example being the model by P. Barna and M. Adamik which takes impurities into account.[35] A model for sputtering was developed by J. Thornton which accounts for ion and atom bombardment.[36,37]

Thornton's structure zone model consists of four zones (Figure 9).[37] In zone I at low temperatures of approximately $T/T_m < 0.2$, the growth of thin films is governed by low surface diffusion. Films deposited under these conditions are porous, and the structure consists of thin crystalline or amorphous columns. The second zone called zone T occurs approximately at $0.2 < T/T_m < 0.3$. It is defined by surface diffusion and competitive grain growth. This results in denser films and increasing grain widths with increasing thickness. The surface diffusion can be induced by temperature and by ion and atom bombardment. More energetic bombardment increases the surface atom mobility which enables T-zone growth at lower temperatures. In zone II at temperatures of $0.3 < T/T_m < 0.5$, surface diffusion and grain boundary migration become increasingly important, and the grains grow larger. At even higher temperatures in the zone III, bulk diffusion becomes the dominating factor. In this zone, the structure of the thin film is determined by the surface energy of the resulting crystals. Growth in the zone T is required for AlN and $Sc_xAl_{1-x}N$, as it enables the growth of dense and well-oriented grains at low temperatures.

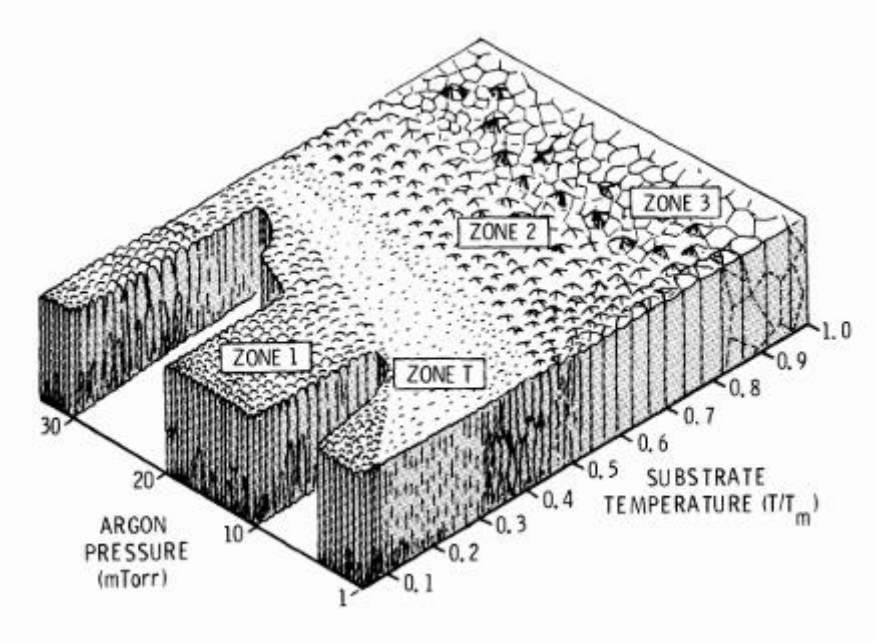

Figure 9. Thornton's structure zone model where microstructural evolution is described as a function of temperature and sputtering pressure. Adapted from[37], copyright 1987 SPIE.

6. Etching of AlN

AlN can be etched with both dry etching and wet etching. Dry etching of AlN is done with Cl_2/BCl_3 plasmas, with a possible addition of Ar.[38–42] Etch rates can be up to 400 nm/min. The sidewall angle is typically 70–80 °, and it can be controlled by tuning the etch parameters. Cl-plasma etches AlN by forming volatile Al_2Cl_6 and N_2. However, the selectivity can be an issue, since Cl-based plasmas etch many materials quite rapidly, such as photoresist, Si, SiO_2 and Mo.

AlN can be wet etched with both acidic and alkaline solutions. It dissolves in acidic solutions according to reaction (5) and in alkaline solutions according to reaction (6).

$$\mathrm{AlN_{(s)} + 4\ H^{+}_{(aq)} \rightarrow Al^{3+}_{(aq)} + NH^{+}_{4\,(aq)}} \quad (5)$$

$$\mathrm{AlN_{(s)} + \ OH^{-}_{(aq)} + 3\ H_2O \rightarrow Al(OH)^{-}_{4\,(aq)} + NH_{3\,(aq)}} \quad (6)$$

Aqueous solutions of KOH, TMAH and H_3PO_4 are used commonly, as they are typical chemicals in microelectronics manufacturing. Both KOH and TMAH are used for anisotropic etching of Si and as photoresist developers. TMAH is highly toxic, but it does not contain metal ions. This makes it usable in environments where highly sensitive semiconductor devices are fabricated and contamination with harmful metals cannot be allowed. H_3PO_4 is used for example etching Si_3N_4 selectively over SiO_2 and as a part of Al-etch solutions.

Wet etching of AlN is highly anisotropic. Firstly, etching of the N-polar surface with KOH is approximately 1000 times faster than etching of the Al-polar surface.[43] Due to the orientation dependent etching of AlN, low-quality films may be difficult to etch as Al-polar grains can result in unetched areas in N-polar films. On the other hand, wet etching can be used to reveal these grains or distinguish the film polarity.[44,45]

Secondly, etching AlN leads to structures with tilted sidewalls (Figure 10) as the tilted planes are etched slower compared the other planes.[46] These tilted planes are collectively called as pyramidal planes. Also, the etching of N-polar AlN does not proceed evenly on the (000–1) plane, but AlN forms cones which are etched slowly (Figure 10). The formation of cones occurs with both single-crystal and polycrystalline AlN.[43,47] In polycrystalline films, the cones are round. With single crystal AlN, they are typically hexagonal. The sidewall defining planes can be for example the {10–1–1} or {10–1–2} families of planes.[43,48]

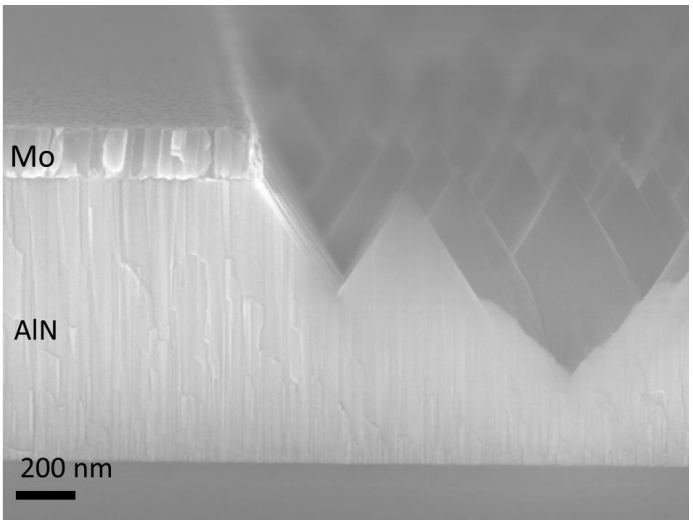

Figure 10. Partially wet etched AlN showing the formation of cones and a tilted sidewall due to the slow etch rate of the pyramidal planes.

The anisotropic etching can be exploited for the fabrication of AlN-structures. When partially masked AlN is wet etched, the very reactive (000–1) plane is rapidly etched in areas where it is not protected by the mask, while the sidewall-forming pyramidal planes are etched slowly.[46] This enables the fabrication of AlN structures with dimensions close to the original mask and with steep sidewalls. However, if the interface between the mask and AlN is poor, the lateral etch rate can be much higher than just the etch rate of the pyramidal planes. Lateral etching by either mechanism leads to the AlN being etched from below the mask. Significant undercutting has often been reported for wet etched AlN.[49–51] Techniques for minimizing undercutting are

crucial for high-fidelity patterning of AlN with wet etching, but detailed studies on the topic are lacking. Minimization of undercutting during wet etching of AlN and $Sc_xAl_{1-x}N$ is one of the main topics of the experimental section.

Reported etch rates of N-polar AlN vary significantly between studies for several reasons, and thus they are poorly comparable to each other. Firstly, determining the etch rate can be difficult due to the formation of cones as discussed earlier. This makes measuring the etch rate ambiguous, and the exact measurement procedure has often not been reported. Secondly, the etch rate of AlN depends highly on the crystalline quality and grain size of the film.[49] Etching of single-crystal AlN can be several orders of magnitude slower compared to polycrystalline AlN.[51] For sputtered AlN, the sputtering conditions affect the crystalline quality and consequently the etch rate.[47,52] The etch rate can also depend on the substrate material and quality.[47,51]

Etching N-polar AlN with alkaline solutions is very fast. For example, the etch rate of sputtered AlN with 15 % KOH at room temperature was 2.5–10 nm/s.[52] With 85 % H_3PO_4 the etch rate was be much slower, reaching 7–30 nm/s only at 80 °C.[52] In a second study, the etch rate of sputtered AlN was 8000 nm/min with 25 % TMAH at 82 °C, and 90 nm/min with a solution of 80 % H_3PO_4, 16 % H_2O and 4 % HNO_3 at 90 °C.[48]

Etching Al-polar AlN with wet etching is much less practical. In single crystal Al-polar AlN, deep etch pits are formed likely due to dislocations in the crystals.[53] This leads to uneven and uncontrollable etching.[49] UV-assisted and electrochemical etching have been developed to enhance the etch rate of Al-polar AlN.[54,55]

Despite the broadly varying etch rates, the activation energy of AlN wet etching has been quite similar in most studies (Table 1). The values vary between 57 and 77 kJ/mol. The activation energy does not seem to depend significantly on the film quality, crystalline structure, or deposition technique.[51,52] However, due to the limited number of reported values, it is unclear whether the activation energy varies between different etchants. The activation energy can be determined with the Arrhenius equation (7)

$$k = Ae^{\frac{-E_a}{RT}}, \tag{7}$$

where k is the reaction (etch) rate, A is the rate constant, E_a is the activation energy, R is the universal gas constant, and T is the absolute temperature.

Table 1. Activation energies for AlN wet etching.

Activation energy (kJ/mol)	Etchant	AlN deposition technique	Single crystal	Reference
67	AZ400K developer (2 % KOH)	Sputtering	No	[51]
67	AZ400K developer (2 % KOH)	MBE	Yes	[51]
77	85 % H_3PO_4	Sputtering	No	[52]
57	1 % KOH	Physical vapor transport	Yes	[45]
68.5 (lateral etching)	85 % H_3PO_4	MOCVD	No	[55]

7. Etching of $Sc_xAl_{1-x}N$

Since $Sc_xAl_{1-x}N$ consists mostly of AlN, its etching techniques have been developed from those used for AlN. Both wet and dry etching of $Sc_xAl_{1-x}N$ have been reported, but no detailed studies on wet etching of $Sc_xAl_{1-x}N$ have been published.

Dry etching of $Sc_xAl_{1-x}N$ with Cl_2/BCl_3 plasmas is much more difficult compared to pure AlN. $ScCl_3$ is not nearly as volatile as Al_2Cl_6, and the etch rate of $Sc_xAl_{1-x}N$ slows down with increasing x. The etch rate at just x = 0.2 has often been 4–5 times lower compared to AlN.[13,56] Table 2 summarizes and compares reported etch rates for $Sc_xAl_{1-x}N$, AlN, and some mask materials.

Table 2. Etch rates for different $Sc_xAl_{1-x}N$ compositions and some mask materials in dry etching.

Material	Gas composition (sccm)	RIE type	Etch rate (nm/min)	Power (ICP/RF) (W)	Reference
AlN	$Cl_2/BCl_3/Ar$ (15/5/5)	CCP	104.1	25	[13]
$Sc_xAl_{1-x}N$ (x=0.04)			90.7		[13]
$Sc_xAl_{1-x}N$ (x=0.14)			29		[13]
$Sc_xAl_{1-x}N$ (x=0.22)			17.3		[13]
$Sc_xAl_{1-x}N$ (x=0.31)			4.5		[13]
AlN	$Cl_2/BCl_3/Ar$ (25/5/70)	ICP	200	400/125	[56]
$Sc_xAl_{1-x}N$ (x=0.2)			50		[56]
SiO_2			~100		[56]
$Sc_xAl_{1-x}N$ (x=0.2)	$Cl_2/BCl_3/Ar$ (25/15/70)	ICP	150	600/350	[56]
$Sc_xAl_{1-x}N$ (x=0.15)	$Cl_2/BCl_3/He$	ICP	160	550/150	[57]
Hard baked photoresist			~400		[57]
AlN	$Cl_2/BCl_3/Ar$ (90/30/70)	ICP	300	400/120	[58]
$Sc_xAl_{1-x}N$ (x=0.36)			40	550/150	[58]
$Sc_xAl_{1-x}N$ (x=0.36)			90	600/250	[58]
AlN	$SiCl_4$	ICP	24	150/225	[59]
$Sc_xAl_{1-x}N$ (x=0.27)			10		[59]
Si_3N_4			20		[59]

Wet etching of $Sc_xAl_{1-x}N$ has been reported using KOH, TMAH and H_3PO_4, but very few details have been published as of writing. The cases where the etch rate was reported are presented here. The etch rates are poorly comparable due to the varying experimental conditions and possible differences in the measurement procedure. With 25% KOH, removal of a 500 nm $Sc_{0.36}Al_{0.64}N$ film took only 15 s at 80 °C.[18] With 85 % H_3PO_4 in 15 min at 80 °C, the same film was etched only partially with a large amount of cones remaining, indicating a much slower

etch rate. In another study, the etch rate of $Sc_{0.35}Al_{0.65}N$ with 20:80 H_2O:H_3PO_4 at 80 °C was 38.5 nm/min, which correlates with the previous result.[60] For 1 µm $Sc_{0.2}Al_{0.8}N$ film, the required time to fully etch the film was 7 min with 25% KOH at 40 °C and 25 min at room temperature.[61] With MIF-319 developer containing 2.2 % TMAH, the etch rate of $Sc_{0.15}Al_{0.85}N$ was reported to be about 50 nm/min at 60–70 °C, while the etch rate of AlN was four times larger.[57]

No details on the anisotropy of $Sc_xAl_{1-x}N$ wet etching have been reported, but polarity dependence has been observed similar to AlN. N-polar $Sc_xAl_{1-x}N$ is etched much faster than III-polar $Sc_xAl_{1-x}N$.[18]

A significant difference to wet etching of AlN is that Sc is poorly soluble in strong alkaline solutions.[62–64] Instead of dissolving as $Sc(OH)_4^-$, Sc easily precipitates as $ScO_x(OH)_y$. This occurred when $Sc_{0.2}Al_{0.8}N$ was etched with TMAH during the experimental part and it will be discussed in Chapter 10.7.

8. Piezo-MEMS technology and applications of $Sc_xAl_{1-x}N$ thin films

Piezoelectric MEMS devices, as the name suggests, employ a piezoelectric material to translate electric signals to mechanical motion and vice versa. Piezo-MEMS devices have been separated here to two sections: devices which act as electric components and are not intended to interact with the surroundings in typical applications, and devices that interact with the surroundings. In the first category, the most important devices are the bulk acoustic wave (BAW) resonator and the surface acoustic wave (SAW) resonator, which rely on the piezoelectric effect for their operation. On the other hand, the second category includes devices which can be realized either with piezoelectric or electrostatic actuation.

8.1. MEMS resonators

The BAW and SAW resonators are the most successful piezo-MEMS devises. Their main application is in acoustic filters for telecommunication and other wireless communications. An acoustic filter is a device which consists of several BAW or SAW resonators combined together on a single chip (Figure 11). They are used in nearly every wireless device for selecting the transmission and reception frequencies, up to frequencies of several GHz. Each smartphone

can contain dozens of filter elements, meaning that billions of BAW and SAW resonators are fabricated each year just for smartphones alone.[65]

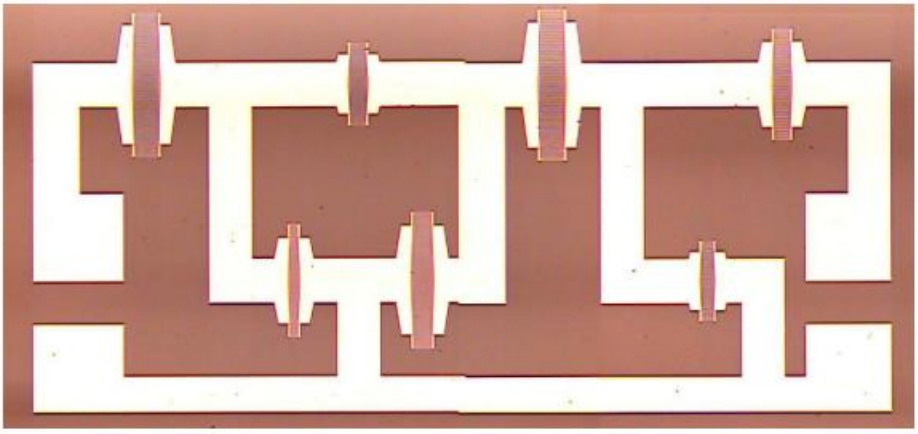

Figure 11. A ladder filter consisting of 7 SAW resonators. Adapted from[66], copyright 2007 IEEE.

The basic idea of piezoelectric resonators is that they transform the electric signal to a motion of the piezoelectric material and back to an electric signal, acting as impedance elements in the process. The electric response of a piezoelectric resonator is similar to a capacitor, but they exhibit a resonance-antiresonance behaviour.[67] At most frequencies, the signal is attenuated by the impedance, but at the resonance frequency, the impedance of the device vanishes. At the antiresonance frequency the impedance is increased. The antiresonance frequency is higher than the resonance frequency, and the difference between them depends on the electromechanical coupling coefficient of the piezoelectric material.

The operation of acoustic filters can be explained using Figure 12 which shows the topology of a ladder filter consisting of several resonators tuned either to a slightly higher (HI) or lower (LO) frequency. At low and high frequencies, the signal is only partially passed by both HI and LO filters. The signal is partially blocked and partially grounded, which results in low transmission. When the frequency approaches the resonant frequency of the LO resonator, the signal is completely grounded as the impedance of the LO filter reaches its minimum. As the frequency increases towards the antiresonance frequency of the LO resonator, its impedance is increased, which prevents the signal from being grounded. Instead, the signal passes through the HI resonators. At the resonant frequency of the HI resonators, the signal is easily passed through them. At the antiresonance frequency of the HI resonators, the signal is blocked by their high impedance.

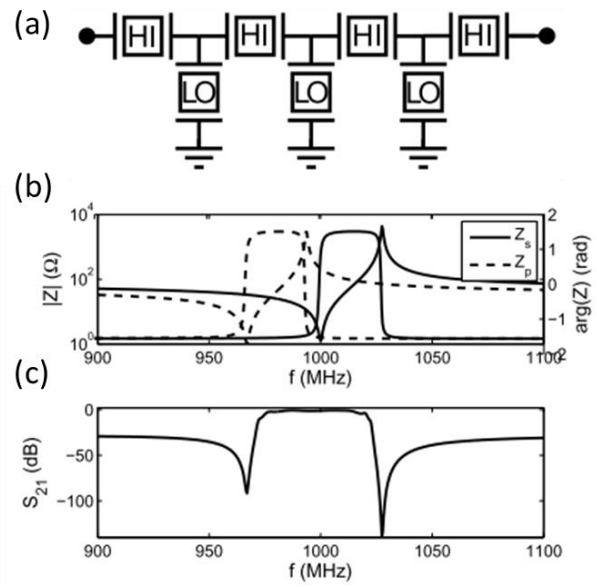

Figure 12. (a) A schematic showing the topology of a 3½-stage ladder filter. The resonators labelled HI have higher frequency and the resonators labelled LO have lower frequency, (b) the impedances of the HI and LO filters, (c) the transmission of a filter made from the HI and LO resonators. Adapted from[67] with permission.

Resonators require a piezoelectric material with good mechanical quality, as otherwise there will be significant losses in the device. A large electromechanical coupling coefficient is also crucial for resonators in filter applications. The bandpass of a filter depends on the difference of the resonance and antiresonance frequencies of the resonators which increases with the coupling coefficient. Broader bands and thus faster communications can be achieved with higher coupling coefficients.

A BAW resonator consists of a piezoelectric thin film sandwiched between two electrodes. When a high-frequency AC voltage, a signal for example, is applied to the BAW resonator, the piezoelectric material is deformed. If the frequency of the voltage is close to a resonance frequency of the device, the deformation is more significant, and the device starts to oscillate at the resonant frequency. This does not occur at other frequencies, and the signal is attenuated. To prevent the escape of the acoustic vibrations to the substrate, the resonator is either grown on an acoustic reflector stack or it is released from the backside by removing the substrate or using a sacrificial layer (Figure 13).

BAW devices are fabricated by depositing and patterning a stack of thin films on a Si substrate. A BAW device may require 10 or more thin films and several lithography steps.[68] This makes BAW devices more complicated to manufacture compared to SAW devices. For a BAW device,

the piezoelectric material must be deposited with thin film deposition techniques, and additionally it must have low losses and a high electromechanical coupling coefficient. This leaves only AlN, ZnO and more recently also $Sc_xAl_{1-x}N$ as reasonable choices.[67] Out of these, AlN and $Sc_xAl_{1-x}N$ are applied commercially.

SAW devices utilize propagating or standing waves on the surface of a piezoelectric material. The SAW is generated by applying an AC voltage to a pair of comb-shaped electrodes called as an interdigital transducer (IDT) (Figure 14). SAW devices consist of either one or two pairs of transducers which are called as one-port and two-port resonators, respectively. The one-port resonator functions similarly to the BAW resonator, and one-port SAW filters can be combined to form a ladder filter for example (Figure 11). The two-port resonator acts as a filter in itself, and it is called as a coupled resonator filter (CRF). For each application, the structure of the IDTs is modified and reflectors are added to enhance the performance. In the two-port resonator, the IDTs can also be separated by a significant distance, in which case the device is no longer a filter but a delay line.

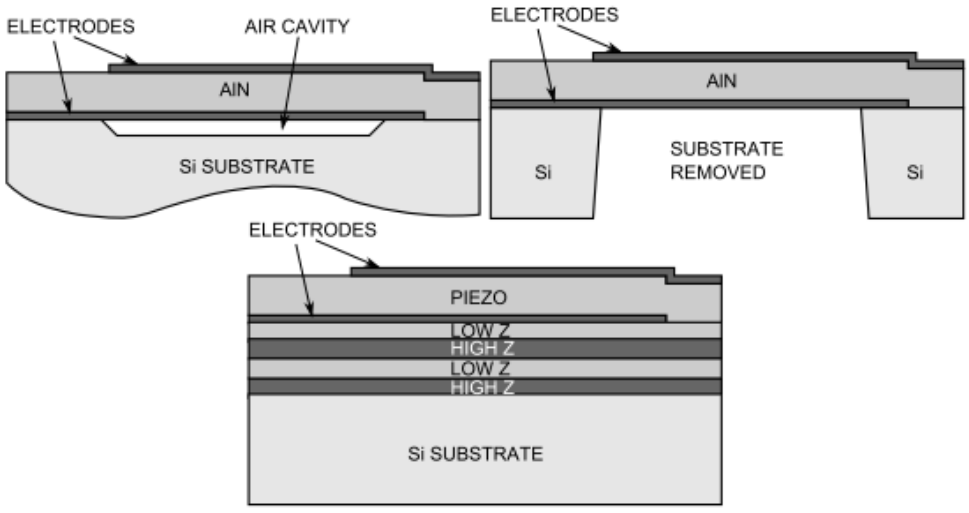

Figure 13. Different BAW resonator structures: suspended over a cavity made by removing a sacrificial layer (top left), suspended by removing substrate from the backside (top right) and mounted on a reflector (bottom). Adapted from[67] with permission.

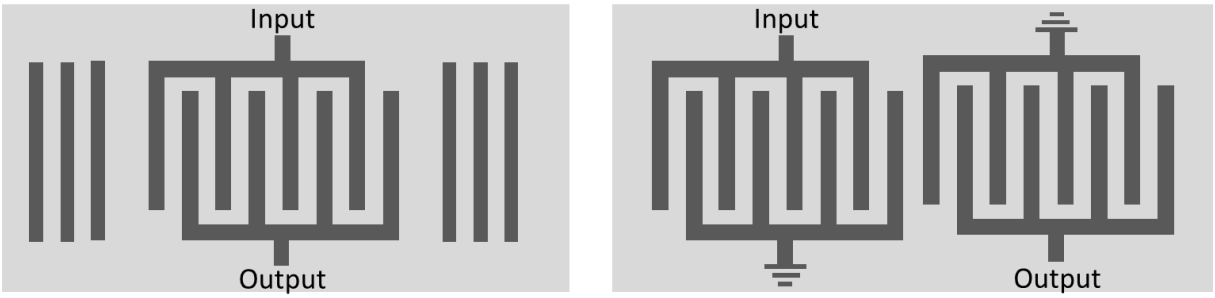

Figure 14. IDT structure of a one port SAW resonator with two reflectors (on the left), and a CRF (on the right).

SAW devices are usually fabricated on piezoelectric single-crystal substrates, such as lithium niobate ($LiNbO_3$), lithium tantalate ($LiTaO_3$) and quartz (SiO_2).[68] Polycrystalline thin films, such as AlN and $Sc_xAl_{1-x}N$ can also be used for SAW devices.[69,70] However, these are not suitable for demanding applications such as telecommunications, but there are other emerging possibilities. An advantage of SAW devices is that they are much simpler to fabricate compared to BAW devices. In the simplest case, they require only an electrode metal deposited and patterned on the substrate.

In addition to the fabrication complexity, there are significant differences in the performance between BAW and SAW filters.[68] The maximum frequency of SAW filters is more limited compared to BAW filters. With SAW resonator, the frequency depends on the acoustic wave velocity and the pitch between the fingers of the transducer. With BAW resonators, it is dependent on the acoustic wave velocity and thicknesses of the piezo and electrode layers. Reaching high frequency and performance with SAW resonators is challenging due to the required small pitch, which makes consistent fabrication difficult and expensive, and the device more prone to failures. BAW resonators on the other hand can be fabricated to reach higher frequencies. They are used for example in the 5G bands which go up to 6 GHz, while SAW filters are typically limited to frequencies below 2.5 GHz.[68]

SAW and BAW devices can also be applied for various sensing applications. Both resonator types can be designed to have their resonant frequency depend on some external stimuli. For example, the frequency of a SAW device is dependent on the temperature, strain of the substrate, and the surface condition of the device. Thus SAW devices are a small and cheap solution for temperature sensing as well as for measuring physical deformation, such as torque in a shaft or bending of a diaphragm for pressure sensing (Figure 15).[71] $Sc_xAl_{1-x}N$-based SAW temperature sensors have been demonstrated for temperatures of over 800 °C.[72] An additional

advantage is that SAW sensors can be wireless. When the sensor is connected to an antenna, it can be read wirelessly with a suitable RF signal without any additional power applied to the sensor.[71]

SAW devices can also be utilized for sensing of gases, chemical species in liquid, or biological agents.[73,74] When the target molecule is attached to an adsorbent on the device surface, the resonant frequency of the devise changes. SAW devices can also be applied for microfluidics.[73] A fluid on the surface can be manipulated with the SAW, some applications being atomization or aerosolization of the fluid, or separation of particles from it. BAW devices on the other hand are especially sensitive to mass loading which makes them very attractive for mass sensing in chemical and biological applications.[75] Additionally, BAW sensors have been demonstrated for measuring infrared or ultraviolet light, and magnetic fields.[76–78]

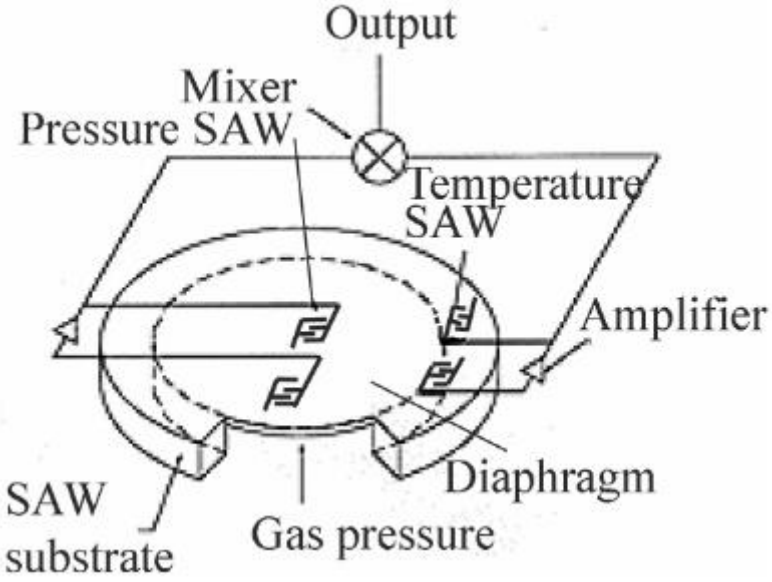

Figure 15. A temperature compensated SAW pressure sensor. Adapted from[71] under the CC BY-NC-ND license.

In addition to the BAW and SAW resonators, MEMS resonators can be based on other structures vibrating at the resonant frequency, such as cantilevers. The cantilever is actuated either piezoelectrically or electrostatically. These kinds of MEMS resonators are available for timing and frequency control as competitors for quartz crystal oscillators for example.[79,80] MEMS resonators can offer smaller device footprint and improved performance compared to quartz resonators.

8.2. Piezoelectric actuation

The second way to utilize piezoelectric materials in MEMS devices is using them in actuating components of the MEMS device or using the converse effect for sensing motion of the device. As the piezoelectric material deforms due to an applied electric field, it can be used for bending, extending or contracting various structures, such as beams and diaphragms (Figure 16a). The most common method of actuation in MEMS devices is electrostatic actuation, but piezoelectric actuation is rising as a competitor.[5]

Piezoelectric actuation has some significant differences compared to electrostatic actuation.[5] Piezoelectric actuators have a much smaller footprint because the piezoelectric materials are integrated with the beams or springs which enable the motion of the device. With electrostatic actuation, large parallel plate or comb drive actuators are required to drive the motion (Figure 16b). Also, with electrostatic actuation only attractive force can be obtained, while a single piezoelectric actuator can deflect in both negative and positive directions. Piezoelectric materials can generate high forces but the strain they can generate is quite small. This limits the extent of motion that can be obtained unless it is amplified by using a cantilever structure for example (Figure 16a). As a rule of thumb, devices with in-plane motion are easier to realize with electrostatic actuators, while out-of-plane motion is easier to fabricate with piezoelectric actuators.

Piezoelectric ultrasonic transducers are some of the most common piezoelectric devices. They are used for both generating and sensing ultrasounds, and they are applied in various measuring applications, such as ultrasound imaging in medicine, sonars, ultrasound testing of steel and parking sensors in cars. Piezoelectric transducers are mostly based on bulk ceramic piezoelectric materials, such as lead zirconate titanate (PZT). Ultrasonic transducers can however be miniaturized with MEMS technology, and these devices are called either as piezoelectric or capacitive micromachined ultrasonic transducers (PMUT, CMUT). PMUTs are based on a vibrating diaphragm which is actuated with a piezoelectric thin film deposited on it (Figure 17a). Introduction of $Sc_xAl_{1-x}N$ has brought significant increases to the performance of PMUTs, as both the transmission and receiving capabilities are increased by the increased piezoelectric responce.[57] PMUT-based distance sensors are already commercially available and other emerging applications medical *in vivo* imaging, air flow measurements and fingerprint sensors.[82–85]

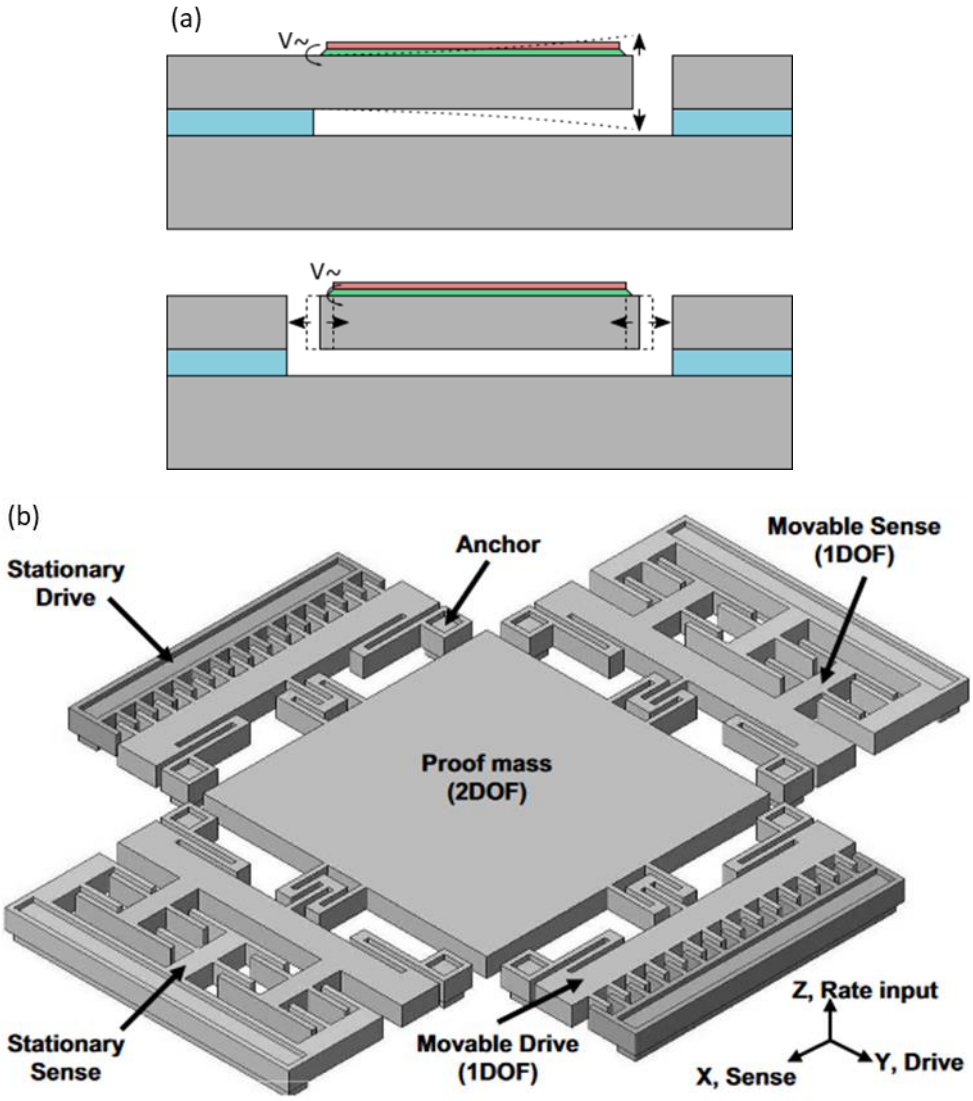

Figure 16. (a) A schematic showing flexural and extensional actuation. The actuation mode depends on whether the operating frequency is close to the resonant frequency of the flexural or the extensional mode. Figure courtesy of Tuomas Pensala. (b) A MEMS gyroscope with electrostatic actuation. Comb actuators are used for driving the device, while plate capacitors are used for sensing the motion induced by rotation around the Z-axis. Adapted from[81], coupyright 2006 IEEE.

For a long time, it has been envisioned that small energy harvesting devices could be used to capture energy from excess motions and vibrations in everyday life. Piezoelectricity is perhaps the phenomenon with the highest potential for accomplishing this task.[86] Piezoelectric energy harvesters could potentially be used for powering *in vivo* medical devices such as pacemakers but also other wireless devices. Due to the good piezoelectric properties, $Sc_xAl_{1-x}N$ is a highly

interesting material for piezoelectric MEMS energy harvesters.[87–89] These devices have been based on micromachined Si-cantilevers which makes their fabrication simple (Figure 17b).

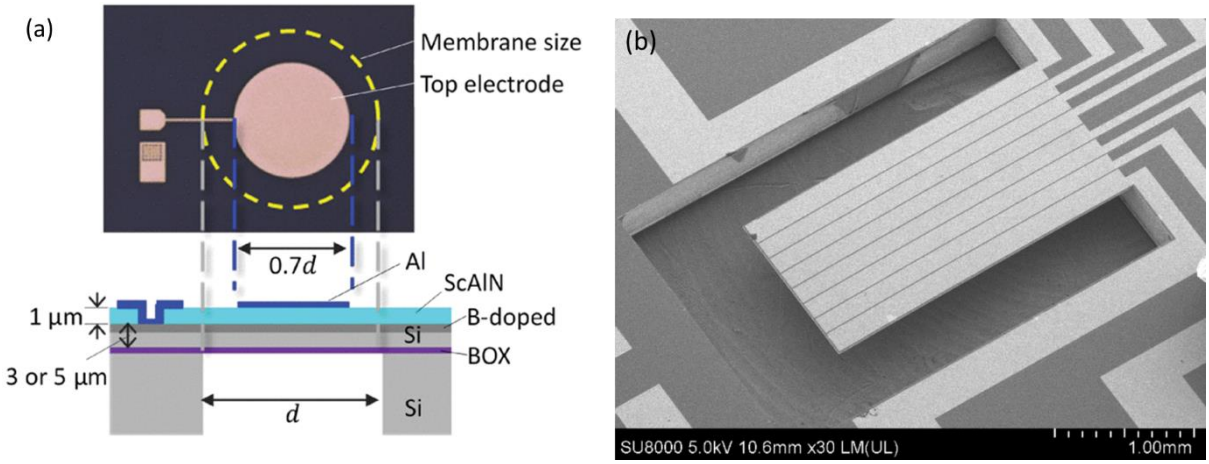

Figure 17. (a) The structure of a PMUT, adapted from[58], copyright 2019 IEEE. (b) A piezoelectric MEMS energy harvester, adapted from[88], copyright 2017 IEEE.

A third example of piezoelectric MEMS is the MEMS mirror. Electrostatic MEMS mirrors have been used for decades, for example in digital micromirror devices (DMD) found in projectors.[5,90] A lamp with a colour filter shines light on the DMD which reflects the light to the canvas. Each mirror is repeatedly turned on and off to control the intensity and colour of the pixel. The DMD has a mirror for each pixel resulting in about two million mirrors at the 1920 x 1080 resolution. A more recent development of the technology are piezoelectric MEMS mirrors in the millimetre scale.[91,92] They have been especially developed for applications in light detection and ranging (LIDAR) devices where they promise small form factor and low price. For example, a mirror with a diameter of 4 mm and ±15 ° tilt angles has been demonstrated with AlN as the piezoelectric material (Figure 18).[91] The device required only 2 V driving voltage.

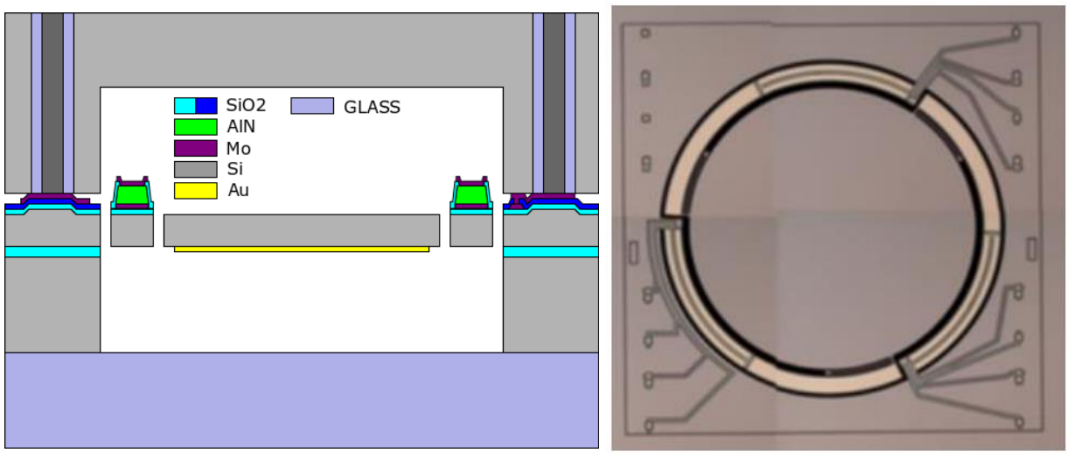

Figure 18. A cross sectional schematic (on the left) and an image from the actuator side (on the right) of a MEMS mirror with 4 mm diameter. The mirror is actuated by up and down bending of the three supporting beams. Adapted from[91], copyright 2017 IEEE.

Experimental

9. Experimental methods

In this section, the sample preparation, etching, and characterization are discussed. The main focus of the experimental work was developing optimized patterning processes for AlN and $Sc_{0.2}Al_{0.8}N$ films. Especially undercutting during etching, its causes, and techniques for minimising it were studied. The etching of $Sc_{0.2}Al_{0.8}N$ was studied in more detail compared to AlN, as optimizing the process for it was more challenging.

9.1. Thin film depositions

150 mm p-type (100) Si-wafers were used as substrates in all experiments. The AlN and $Sc_{0.2}Al_{0.8}N$ films were deposited directly on the Si-wafer, and a mask material was deposited on top. Four mask materials were studied: Mo, SiO_2, SiN_x and TiO_2. SiO_2 was deposited with two processes which used different precursors: SiH_4 and TEOS. It is indicated separately if TEOS was used as the precursor. Also, two different tools were used for Mo deposition with a total of seven different processes. These processes are referred to as Mo-1–7 and they are summarized in Table 3.

The masks were chosen for the following reasons. Mo is commonly used as a top electrode for $Sc_xAl_{1-x}N$-based piezo-MEMS. Using Mo as the mask for $Sc_xAl_{1-x}N$ etching could eliminate

the need for an additional mask and thus reduce processing steps. SiO_2 and SiN_x are very common materials in MEMS manufacturing, and they can be easily removed with HF after the $Sc_xAl_{1-x}N$ etching. TiO_2 was chosen as a comparison to the other films.

AlN and $Sc_{0.2}Al_{0.8}N$ films and most of the Mo mask layers were deposited with an *Evatec Clusterline 200 II* (CLN 200) cluster sputtering system. The deposition tool included an ICP etching chamber which was used to clean the substrate before the film deposition. The aim of the cleaning was to remove any native oxide and organic contaminants providing a repeatable surface for the film deposition. The ICP plasma cleaning was done with Ar as the etching gas and with 100 W RF power.

AlN and $Sc_{0.2}Al_{0.8}N$ thin films were deposited with pulsed DC reactive magnetron sputtering using 304 mm diameter Al and $Sc_{0.2}Al_{0.8}$ targets, respectively. The deposition temperature was 300 °C and the sputtering power was 7.5 kW. The ratio of gas flows was 1:3 Ar:N_2 and the RF bias power was 18 W for AlN and 12 W for $Sc_{0.2}Al_{0.8}N$. Thicknesses of the deposited films were 1000–1040 nm.

A *Von Ardenne CS 730 S* cluster sputtering system was used to deposit Mo on AlN and $Sc_{0.2}Al_{0.8}N$ in the Mo-1 and Mo-2 processes. Before the Mo deposition, the AlN or $Sc_{0.2}Al_{0.8}N$ surface was cleaned using an Ar ion gun included in the tool for 30 s with 200 W RF power. The Mo deposition was done at room temperature with Ar as the sputtering gas and 1 kW sputtering power. In the Mo-2 process, a 25 nm PECVD SiN_x layer was deposited on $Sc_{0.2}Al_{0.8}N$ as an adhesion layer before the Mo deposition. The SiN_x deposition process is described later.

The CLN 200 was used to deposit Mo with five different processes designated as Mo-3–7. Mo was deposited on AlN using only the Mo-3 process, while all five processes were used for depositing Mo on $Sc_{0.2}Al_{0.8}N$. In the Mo-3, 4 and 5 processes, the AlN or $Sc_{0.2}Al_{0.8}N$ film was exposed to air after its deposition for several days prior to the Mo deposition. The Mo-3 process included a 30 s ICP etch clean before the Mo deposition. In the Mo-4 process the etch clean time was increased to 150 s, and in the Mo-5 process the etch clean was omitted. In the Mo-6 and Mo-7 processes, the $Sc_{0.2}Al_{0.8}N$ film was not exposed to air after its deposition and the Mo mask was deposited without breaking the vacuum. The Mo-6 process included the 30 s ICP etch, while the Mo-7 process did not include it. In all processes, the deposition temperature was 200 or 300 °C, the sputtering gas was Ar, and the power was 1 kW. The thicknesses of the Mo films were about 200 nm.

Table 3. A summary of the different Mo deposition processes.

	Mo-1/2	Mo-3	Mo-4	Mo-5	Mo-6	Mo-7
Deposition tool	CS 730 S	CLN 200	CLN 200	CLN 200	CLN 200	CLN 200
Plasma cleaning	Ion gun 30 s	ICP 30 s	ICP 150 s		ICP 30 s	
Air exposure	X	X	X	X		

SiO_2 and SiN_x mask layers were deposited with PECVD using an *Oxford Instruments Plasmalab 100*. SiO_2 masks were deposited from two different precursors: SiH_4 or tetraethyl orthosilicate (TEOS). SiH_4-based SiO_2 masks were deposited at 300 °C using SiH_4 and N_2O as precursors and N_2 as an inert gas. TEOS-based SiO_2 was deposited at 350 °C with TEOS and O_2 as the precursors and Ar as an inert gas. SiN_x mask layers were deposited at 300 °C with SiH_4 and NH_3, as precursors and N_2 as an inert gas. Thicknesses of the PECVD mask layers were 150–200 nm.

TiO_2 was deposited with ALD using a *Picosun Sunale R-150B* reactor. The deposition was done at 200 °C with $TiCl_4$ and H_2O as precursors. A 40 nm thick TiO_2 film was obtained with 1000 deposition cycles.

9.2. Annealing and lithography

Some wafers were annealed after the deposition of the thin film stack. Annealing was done with a *PEO-603* furnace in N_2 atmosphere at atmospheric pressure. Annealing temperature was varied from 450 to 900 °C. An annealing cycle consisted of purging the furnace of air, heating at 15–20 °C/min, holding at the desired temperature for 1 h, and cooling at 15–20 °C/min.

The wafers were patterned with photolithography. Resist coating was done with a *Suss MicroTec Gamma 4* coater-developer. The coating included priming the surface with hexamethyldisilazane (HDMS) in a chamber included in the tool, spin coating AZ5214E photoresist on the wafer to a thickness of 2.5 µm, and soft baking the resist on a 90 °C hot plate for 2 min. The resist was exposed through a photomask with a *Suss MicroTec MA6* mask aligner. Finally, the resist was developed for 1 min with AZ351B diluted 1:3.5 with de-ionized (DI) water.

9.3. Thin film etching and resist stripping

The mask layers were patterned with RIE. Mo and TiO_2 mask were etched using a *Surface Technology Systems Advanced Oxide Etcher* ICP-RIE. The etching gases were SF_6, O_2 and Ar for Mo, and CF_4 for TiO_2. SiO_2 and SiN_x masks were patterned using an *Oxford Instruments Plasmalab 80Plus* CCP RIE with CHF_3 and O_2 as the etching gases. After etching the mask layer, the remaining photoresist was stripped with O_2 plasma using an *Oxford Instruments Plasmalab PRS 900* plasma resist stripper.

$Sc_xAl_{1-x}N$ was etched with 25 weight-% TMAH in water (VLSI grade, MicroChemicals). The TMAH was heated in a quartz tank. Before etching of each sample, the TMAH was stirred manually, but no agitation was applied during the etching. The etching temperature and time were varied. After etching, the wafers were rinsed with DI-water and blown dry with nitrogen. $Sc_{0.2}Al_{0.8}N$ was also etched with 85 weight-% H_3PO_4 and 4.5 mol/l H_2SO_4. Additionally, $Sc_{0.2}Al_{0.8}N$ was etched using TMAH with 15 g/l of ethylenediaminetetraacetic acid (EDTA) dissolved into it. The etching with the acids and TMAH/EDTA done with the same procedure as with TMAH but only at 80 °C.

9.4. Analysis

Thicknesses of $Sc_xAl_{1-x}N$ films before etching were measured with a *FilmTek 2000M* reflectometer. For determination of the vertical etch rates, thicknesses of $Sc_{0.2}Al_{0.8}N$ films was measured again with reflectometry after partially etching the films. Etch depths of $Sc_{0.2}Al_{0.8}N$ films were also measured with a *Bruker DektakXT* profilometer.

Vertical etch rates of AlN films were determined by visually observing the disappearance of the films after immersion in the etchant. For accurate determination of this time, the etching was recorded on video. The vertical etch rates of AlN could not be measured with other methods due to the rapid formation of the cone-like structures described in Chapters 6 and 10.1.

Stresses of the thin films were determined by measuring the wafer curvatures before and after thin film depositions, and before and after thermal annealing. The measurements were done optically with a *Toho Technology FLX 2320-S.*

Etched samples were cleaved for determination of lateral etching and sidewall angle. The cleaved surfaces were imaged with a *Zeiss Supra 35* scanning electron microscope (SEM). The lateral etching and sidewall angle were measured with the SEM software.

Energy dispersive X-ray spectroscopy (EDX) was used to study residues which were deposited on the wafer surface. This was done with an *Oxford Instruments Inca EDX* connected to a *Zeiss Leo 1560* SEM.

The compositions of a $Sc_{0.2}Al_{0.8}N$ reference sample and $Sc_{0.2}Al_{0.8}N$ samples with differently deposited Mo masks were analysed using time-of-flight elastic recoil detection analysis (TOF-ERDA) and secondary ion mass spectrometry (SIMS). TOF-ERDA measurements were done at the University of Helsinki accelerator laboratory with a 5 MeV tandem accelerator using a 35 MeV $^{79}Br^{7+}$ beam with 78 ° sample angle and 40 ° detection angle. SIMS measurements were done with a VG IX70S SIMS instrument using a 11 keV Cs-ion beam. The analysed elements were H, C, O, F, Al, Si, Sc and Mo. Each sample was measured twice.

10. Results

10.1. Etching mechanisms of AlN and $Sc_{0.2}Al_{0.8}N$

Etching of AlN and $Sc_{0.2}Al_{0.8}N$ was a relatively complex process due to the formation of conical features with both films. These cones were etched slower compared to the rest of the film. The etching of these films is therefore described here with three different values: vertical etch rate, time for full film removal, and lateral etch rate. Vertical etch rate describes the time required for most of the film to be etched away exposing the material underneath. Time for full film removal describes the time required to also etch all of the cones. For AlN and $Sc_{0.2}Al_{0.8}N$ films this was approximately 10–15 and 8 times longer than the time indicated by the vertical etch rate, respectively. Lateral etch rate describes how rapidly the etching proceeded below the mask causing the undercut.

AlN and $Sc_{0.2}Al_{0.8}N$ behaved very differently during the etching. AlN formed steep cones very rapidly while $Sc_{0.2}Al_{0.8}N$ was mostly etched evenly and the surface remained flat except for individual cones (Figure 19a, b). For this reason, the etch depth of AlN could not be measured with reflectometry or profilometry. Instead, it was approximated from the time it took for the thin film to visibly disappear during etching. With $Sc_{0.2}Al_{0.8}N$ films, cones were only formed around AOGs which were etched slower due to their misorientation. Two types of AOGs were observed in the $Sc_{0.2}Al_{0.8}N$ films: those with sizes of around 100 nm and those with sizes of over 200 nm when viewed from the top (Figure 19c). Cones were formed around both during the etching (Figure 19d). The sidewall angles of the cones were 57–59 ° with AlN and 45–47 ° with $Sc_{0.2}Al_{0.8}N$.

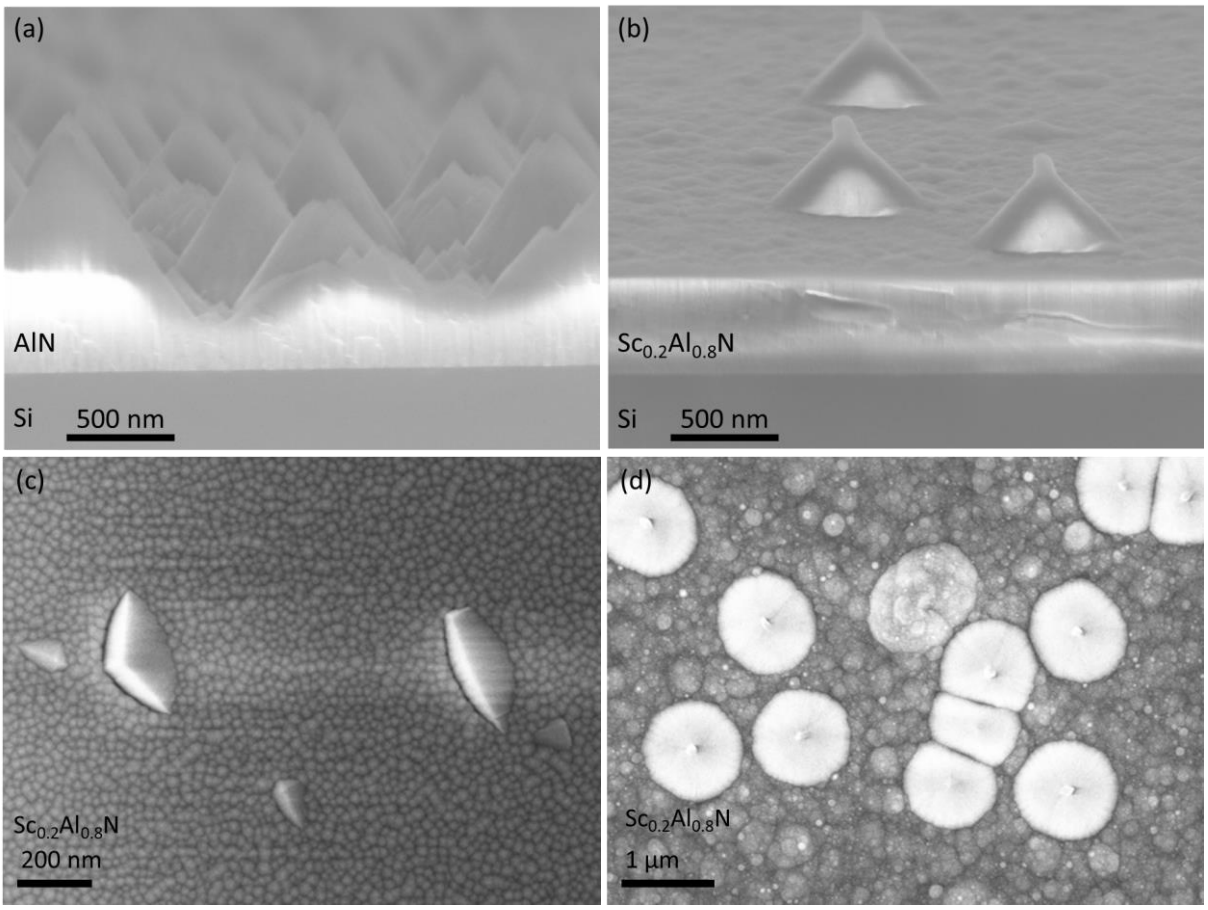

Figure 19. Cross-sectional images of partially etched (a) AlN and (b) $Sc_{0.2}Al_{0.8}N$ films. (c) A top-down image of $Sc_{0.2}Al_{0.8}N$ film with small and large AOGs and (d) $Sc_{0.2}Al_{0.8}N$ film after partial etching.

The full removal of the films was determined by inspecting the samples with an optical microscope, where the cones were visible as black spots (Figure 20a). The cones were not removed at an equal rate, but some of them were removed much faster much faster than others. Initially the density of the cones was typically quite high with both AlN and $Sc_{0.2}Al_{0.8}N$. After the films had been etched through, the density and size of the cones started to decrease. However, once almost all of the cones had been removed, single tall cones were still found, indicating a highly varying removal rate from cone to cone. This occurred with both AlN and $Sc_{0.2}Al_{0.8}N$ (Figure 20b).

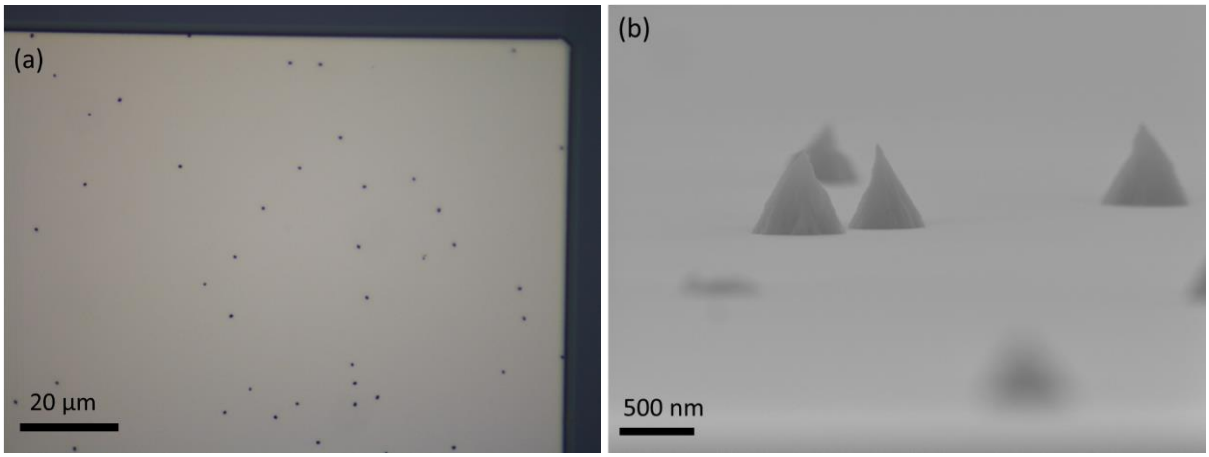

Figure 20. (a) A microscope image of a $Sc_{0.2}Al_{0.8}N$ film after etching the bulk of the film with some cones remaining. (b) SEM image of a partially etched AlN film with a few 600 nm tall cones remaining.

Initially, four possible mechanisms behind lateral etching of AlN and $Sc_{0.2}Al_{0.8}N$ films were identified: etching of the most stable pyramidal planes, etching due to a poor interface between the mask and the AlN or $Sc_{0.2}Al_{0.8}N$ film, etching due to surface oxidation of the film, and etching due to damage of the AlN or $Sc_{0.2}Al_{0.8}N$ suface caused by ion bombardment. To test these mechanisms, AlN and $Sc_{0.2}Al_{0.8}N$ were etched with a wide variety of different mask materials deposited with different techniques. Additionally, $Sc_{0.2}Al_{0.8}N$ was etched under conditions where it was exposed only to air, only to ion bombardment, or neither of them to investigate their effect independently.

Although the AlN and $Sc_{0.2}Al_{0.8}N$ films were deposited on Si, and TMAH etches Si, no Si etching was observed except with overly long etching times. This could have been caused by formation of SiN_x or mixing of Si and AlN or $Sc_{0.2}Al_{0.8}N$ at the interface resulting in a protective layer.

10.2. Vertical etching of AlN and $Sc_{0.2}Al_{0.8}N$ with TMAH

AlN and $Sc_{0.2}Al_{0.8}N$ were etched at temperatures of about 80, 60, 40 and 21 °C to determine the activation energy of the vertical etching (Figure 22). At about 80 °C, the 1 µm thick AlN film took 3 s to visibly disappear, resulting in a calculated etch rate of 330 nm/s. The etch rate of $Sc_{0.2}Al_{0.8}N$ was measured at 20–30 nm/s at 80 °C. The $Sc_{0.2}Al_{0.8}N$ films were visibly etched in 35–45 s indicating that the film disappearance gave a good estimate of the etch rate. At room temperature the vertical etch rate of AlN was lowered to about 7.5 nm/s, and for $Sc_{0.2}Al_{0.8}N$ it

was 0.24–0.36 nm/s. The vertical etching of $Sc_{0.2}Al_{0.8}N$ was very linear when measured with both profilometry and reflectometry (Figure 21).

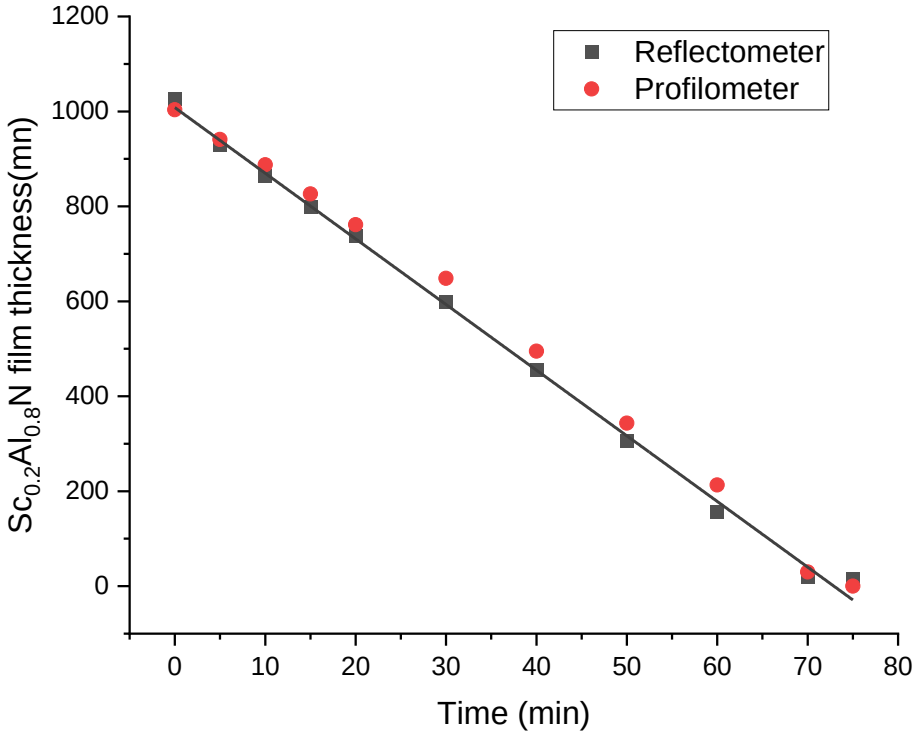

Figure 21. Remaining film thickness of a 1 µm $Sc_{0.2}Al_{0.8}N$ film etched at 21 °C. The line is fitted to the reflectometer data.

Etch rates of different $Sc_{0.2}Al_{0.8}N$ films varied significantly (Figure 22). Possible reasons were that the films were initially used for the deposition process development and thus the deposition conditions were slightly different between them. This could have affected the film microstructure and etch rate as discussed earlier. Film 1 was deposited with more optimized conditions compared to film 2 and film 3. Film 3 was annealed at 700 °C, but the slightly lower etch rate of that film cannot be attributed to the annealing based on these experiments.

From the Arrhenius plots, the activation energy for vertical etching of AlN was 56±8 kJ/mol, and for $Sc_{0.2}Al_{0.8}N$ it was 65±3 kJ/mol. These results were in quite good agreement with the earlier published values. The addition of Sc had only a minor effect on the etching activation energy, and it was the same for the three different $Sc_{0.2}Al_{0.8}N$ films.

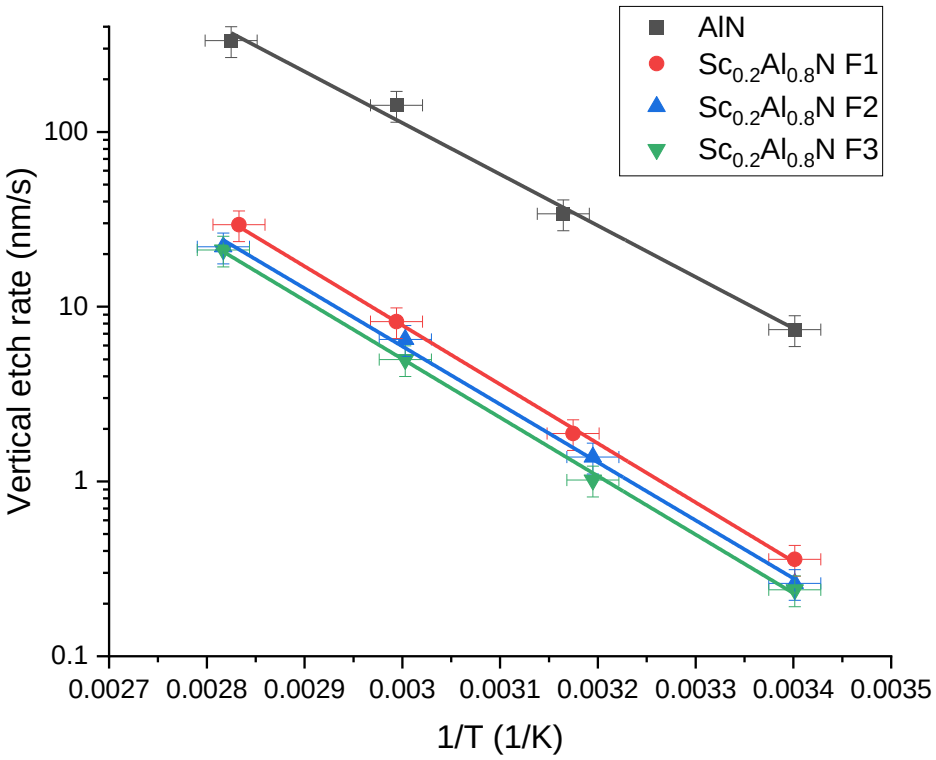

Figure 22. Arrhenius plots of the vertical etch rates of AlN and three different $Sc_{0.2}Al_{0.8}N$ films at temperatures of about 80, 60, 40 and 21 °C with lines fitted to the data points.

For 1 µm AlN films, a minimum etch time of 30 s was required to fully remove the film at 80 °C. For $Sc_{0.2}Al_{0.8}N$, the time was 5 min. At 21 °C, the times were 30 min and 6 h, respectively. For the $Sc_{0.2}Al_{0.8}N$ films annealed at 700 °C (but not at 550 °C), the removal rate of the cones was reduced at low etching temperatures. At an etching temperature of 80 °C, annealing did not affect the etching of the cones, and the full film removal time was still 5 min. However, at 21 °C, the time required to etch all cones was increased to approximately 12 h.

The etch rate of $Sc_{0.2}Al_{0.8}N$ was very uniform across the entire wafer with samples deposited later with more optimized conditions (Figure 23 F1). Films deposited with less optimized conditions (F2 and F3) had sometimes significant nonuniformity in the etch rate across the wafer.

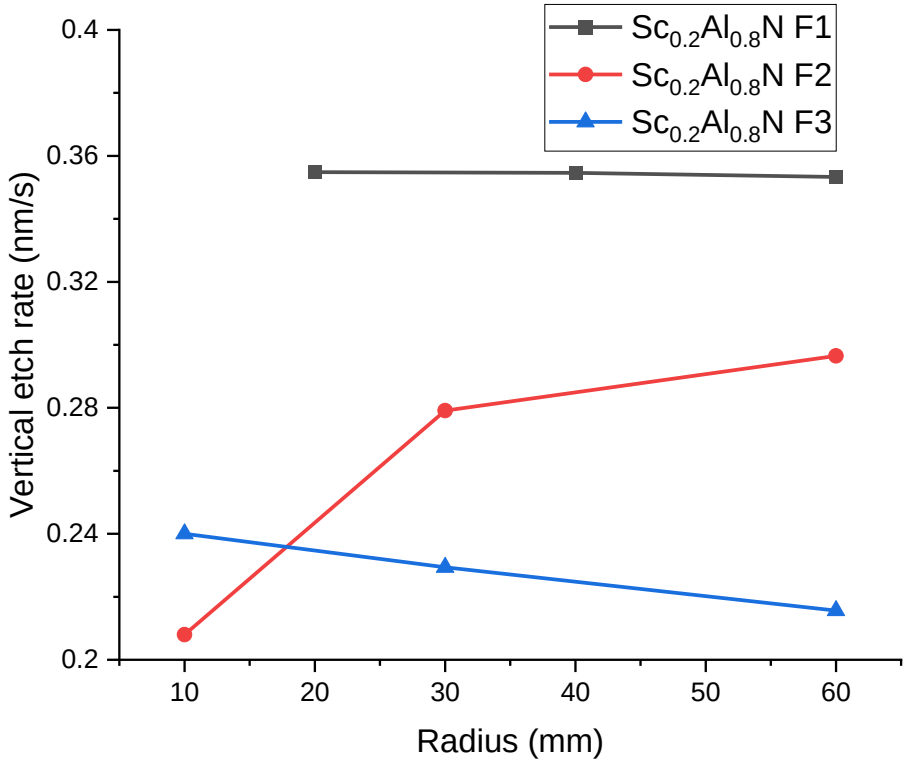

Figure 23. Vertical etch rates at different radii from the wafer centre for three different $Sc_{0.2}Al_{0.8}N$ films etched at 21 °C.

10.3. Lateral etching of AlN with TMAH

Lateral etching of AlN was tested with five different masks: Mo-1, Mo-2, Mo-3, SiO_2 and SiN_x. Table 4 summarizes the results. Sidewall angle of the AlN film after etching with TMAH was always 57–59 °, which corresponds to the {10-1-1} planes (Figure 24a, b). Conical structures formed by these planes were also visible on the sidewall after etching (Figure 24c).

Mo-1 and Mo-2 process were studied first, as they were previously established processes with the older *CS 730 S* sputtering tool. Mo-1 process was used as a baseline process, and it was known to perform poorly. With the Mo-1 mask, the lateral etch rate of AlN with 80 °C TMAH was 7.5 nm/s, which resulted in heavy undercutting (Figure 24a). Mo-2 was an optimization of the Mo-1 process, where a 25 nm SiN_x adhesion layer was added to reduce the undercutting. With the Mo-2 mask, the lateral etch rate was only 0.50 nm/s (Figure 24b).

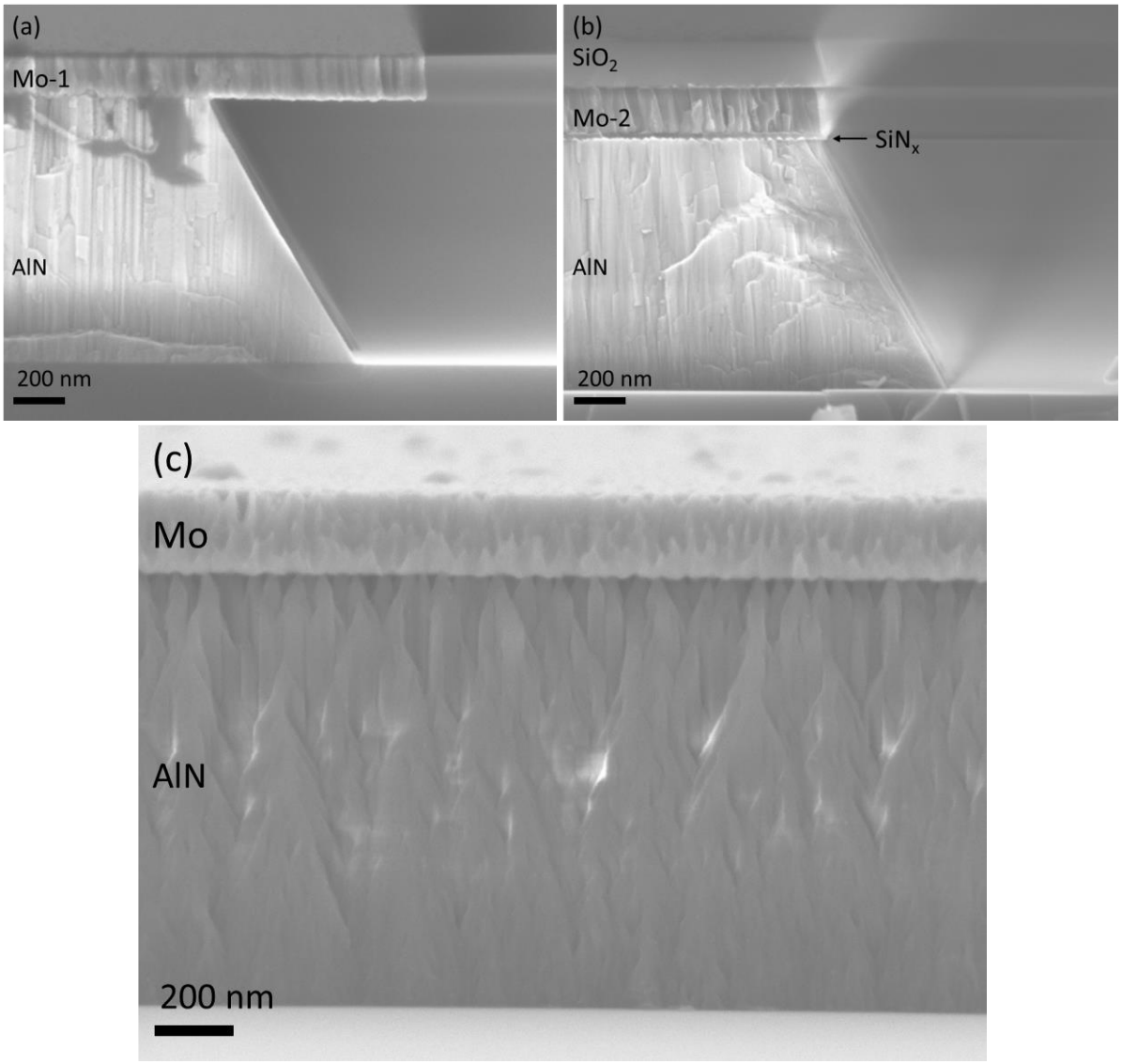

Figure 24. (a) AlN with Mo-1 and (b) Mo-2 mask etched for 2 min at 80 °C. The structure in (b) includes an additional SiO_2 passivation layer. (c) Etched AlN sidewall viewed from the front.

Unexpected results occurred when the study was extended to the Mo-3, SiO_2 and SiN_x masks. Compared to the Mo-1 mask, the lateral etch rate with the Mo-3 mask was lower at 2.1–3.1 nm/s with some variation between different samples. Even more surprisingly, with the SiO_2 and SiN_x masks, the lateral etch rates were 2.8 and 5.0 nm/s, respectively. For the SiN_x mask, this was ten times larger than expected based on the Mo-2 mask, indicating that the SiN_x layer in the Mo-2 mask did not reduce the lateral etching in itself. Instead, somehow the Mo deposition was able to reduce the lateral etch rate when it was done on the thin SiN_x layer.

Using thermal annealing for reducing lateral etching was explored with Mo-3, SiO_2 and SiN_x masks. Annealing at 450 °C reduced the lateral etch rate with the SiO_2 mask to 1.1 nm/s.

Annealing at 550 °C with the Mo-3 mask reduced the lateral etch rate to 0.95 nm/s and with the SiO_2 mask, the lateral etch rate was further reduced to 0.39 nm/s. Annealing at 700 °C reduced the etch rate to negligible with the Mo-3 and SiO_2 masks, and with the SiN_x mask the etch rate was noticeable but small at about 0.2 nm/s. Annealing did not affect the stress of the AlN films significantly.

Table 4. Lateral etch rates (nm/s) of AlN with different mask materials without and with annealing. Etching was done at 80 °C for 3 min ([a] 2 min).

	Mo-1	Mo-2	Mo-3	SiO_2	SiN_x
As deposited	7.5[a]	0.50[a]	2.1–3.1	2.8	5.0
Annealed at 450 °C				1.1	
Annealed at 550 °C			0.95	0.39	
Annealed at 700 °C			0	0	0.22

Based on the results with the annealed SiN_x mask, the decrease in the lateral etching with the Mo-2 mask compared to the bare SiN_x mask was likely due to local heating of the film surface during the pre-deposition cleaning or the Mo deposition itself. As such, there was little benefit from depositing a thin SiN_x layer before a Mo mask, unless it could be locally heated somehow. Therefore, the use of a SiN_x adhesion layer was not investigated with the CLN 200.

It is noted that with the SiO_2 mask the lateral etch was the same regardless if the annealing was done before depositing the mask, after depositing the mask, or after patterning the mask. However, with the Mo-3 mask, only annealing before mask etching was effective. Upon annealing a patterned Mo mask even at 550 °C, the edge of the Mo became damaged leading to increased lateral etching (Figure 25).

The effective lateral etching activation energy of AlN was determined to explore the possibility of reducing the lateral etching by using a lower etching temperature. The term “effective” is used as the activation energy of lateral etching depended on the mask deposition process as shown later. Therefore, it was not an intrinsic material property. With the Mo-3 mask, the effective lateral etching activation energy was 66±5 kJ/mol (Figure 26). This was slightly higher compared to the activation energy for the vertical etching. By lowering the etching temperature from 80 to 21 °C, the selectivity of vertical etching to lateral etching was approximately doubled, meaning that the undercut could be halved.

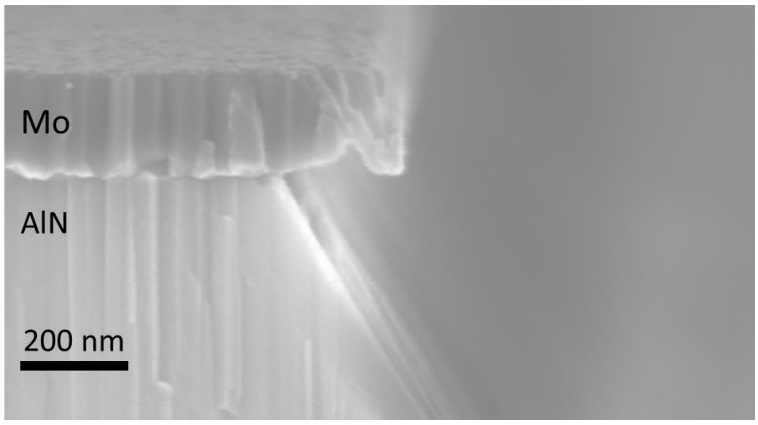

Figure 25. AlN with a Mo mask which was etched and annealed at 700 °C resulting in damage to the edge and increased lateral etching.

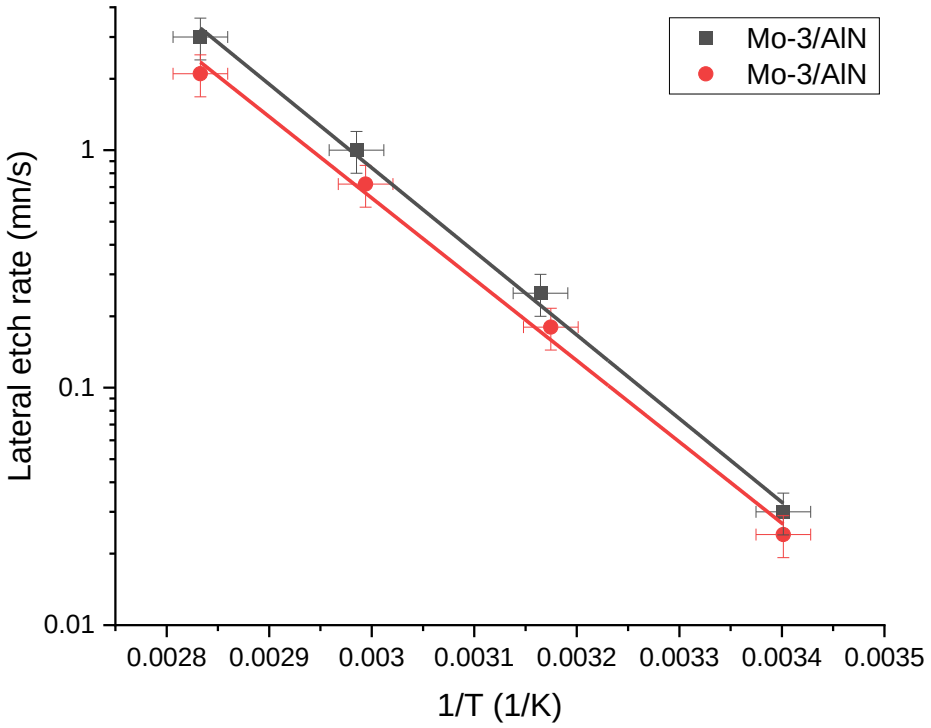

Figure 26. Lateral etch rates of two AlN films with Mo-3 masks at temperatures of about 80, 60, 40 and 21 °C.

The lateral etch rate of AlN had a significant time dependence. Lateral etching did not start immediately, but only after tens of seconds at 80 °C and tens of minutes at 21 °C. With short etching times the lateral etching was much less than indicated in Table 4. With the Mo-3 and SiO_2 masks, the lateral etching was found to be negligible at 30 s and only 50 nm at 60 s (Figure 27). With longer etching times, the lateral etching rate remained constant (2.8 nm/s with 10 min

etching at 80 °C). Due to this time dependence, patterning 1 µm AlN films with minimal undercut was possible without annealing by choosing the minimal etch time required for the film removal (30 s at 80 °C or 30 min at 21 °C).

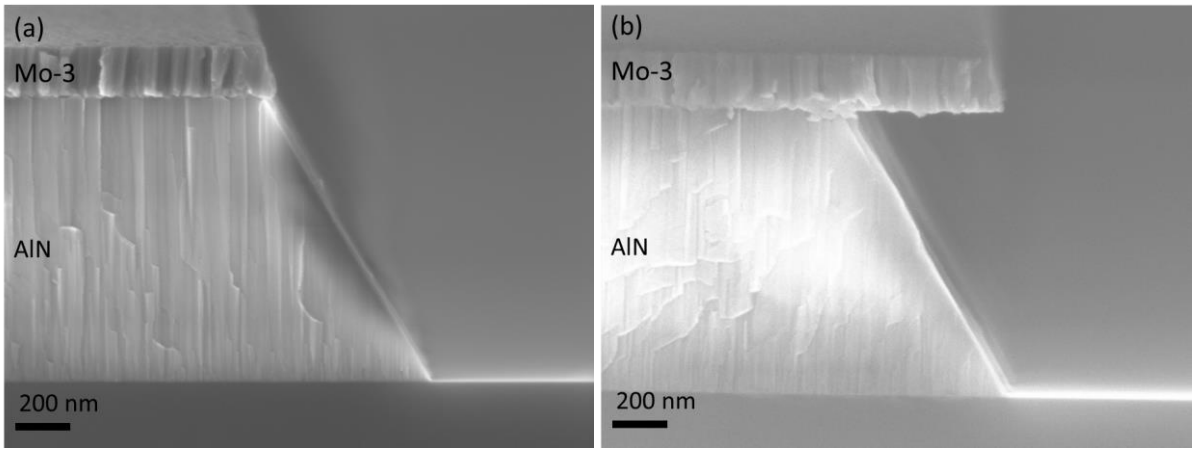

Figure 27. AlN with Mo-3 mask after etching for (a) 30 s and (b) 3 min at 80 °C.

Finally, poor AlN film quality was observed to increase the lateral etch rate of AlN. In a set of experiments where AlN was deposited almost immediately after changing the sputtering target to Al, the film quality was very poor. With these films the lateral etch rates were up to 22 nm/s with the SiO_2 mask even after annealing at 550 °C (Figure 28).

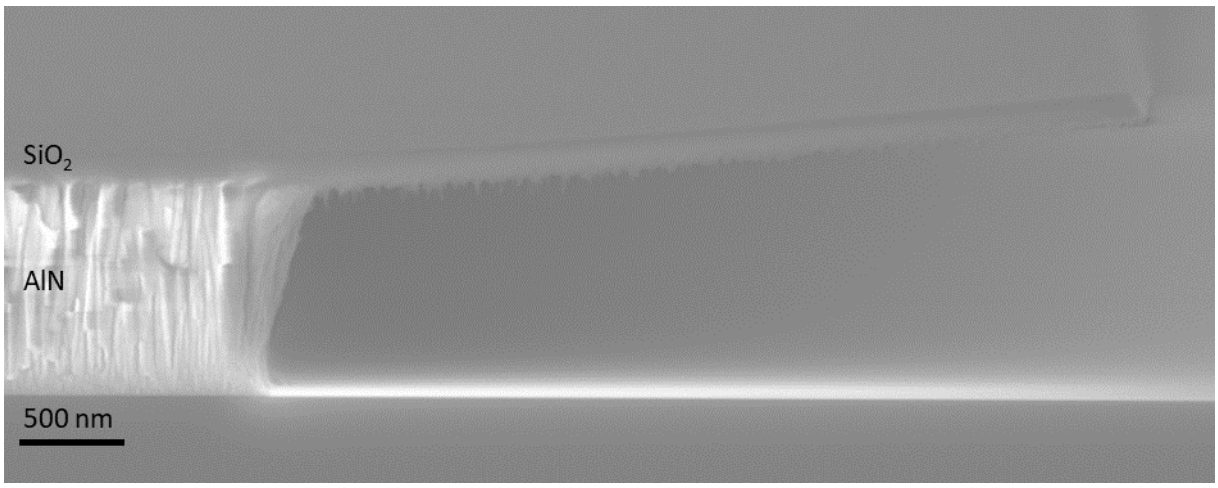

Figure 28. Poor-quality AlN film with the SiO_2 mask annealed at 550 °C and etched at 80 °C for 3 min.

10.4. Lateral etching of $Sc_{0.2}Al_{0.8}N$ with TMAH

Although the vertical etch rate of $Sc_{0.2}Al_{0.8}N$ was about ten times lower compared to AlN, the lateral etch rate was very similar. For this reason the lateral etching was studied in much more detail with $Sc_{0.2}Al_{0.8}N$. A total of 11 different masks were used to further examine how the lateral etching was affected by the mask material, its deposition technique, surface oxidation of the $Sc_{0.2}Al_{0.8}N$ film and surface damage induced by a plasma cleaning step. Table 5 summarizes the results with the differently deposited Mo masks and Table 6 summarizes the results with the other mask materials.

First, the Mo-1 and Mo-2 masks were studied for reference. With them, the lateral etch rate of $Sc_{0.2}Al_{0.8}N$ was 6.0 and 0.66 nm/s, respectively. The effects of surface oxidation and surface damage to the etching of $Sc_{0.2}Al_{0.8}N$ were further studied with the Mo-3–7 masks. The Mo-3 process was the standard process for depositing the Mo top electrode/mask with the CLN 200, and it included exposing the $Sc_{0.2}Al_{0.8}N$ film to air after deposition but applying a 30 s plasma clean before the Mo deposition. With this mask, the lateral etch rate varied from 1.2 to 2.7 nm/s. Increasing the plasma clean time to 150 s in the Mo-4 process yielded a lateral etch rate of 1.1 nm/s, and omitting it in the Mo-5 process resulted in a lateral etch rate of 2.2 nm/s.

$Sc_{0.2}Al_{0.8}N$ films were also deposited so that the Mo mask was deposited immediately afterwards without breaking vacuum. This was done with and without the plasma cleaning. When the plasma cleaning was included in the Mo-6 process, the lateral etch rate was 2.7 nm/s, which was similar to the $Sc_{0.2}Al_{0.8}N$ films which had been exposed to air. However, when the plasma clean was omitted in the Mo-7 process, the lateral etch rate was only 0.37 nm/s (Figure 30a).

Together, these results suggest that the lateral etch rate was significantly increased by both surface oxidation of $Sc_{0.2}Al_{0.8}N$ caused by the exposure to air, and by surface damage caused by a plasma cleaning step. A harsher cleaning step in the Mo-1 process caused increased lateral etching compared to the gentler cleaning in the Mo-3 process. Although the lateral etch rate was similar for the Mo-5 mask which included only the exposure to air, and for the Mo-6 mask which included only the surface cleaning with a plasma, this was likely a coincidence and the main cause for the lateral etching was different.

Table 5. The lateral etch rates (nm/s) of $Sc_{0.2}Al_{0.8}N$ with differently deposited Mo masks with and without annealing. Etching was done at 80 °C for 5 min.

	Mo-1	Mo-2	Mo-3	Mo-4	Mo-5	Mo-6	Mo-7
As deposited	6.0	0.66	1.2–2.7	1.1	2.2	2.7	0.36
Annealed at 550 °C			0.73–1.2				
Annealed at 625 °C			1.5				
Annealed at 700 °C			0.53			0.60	0.45
Annealed at 900 °C			1.3				

The lateral etching of $Sc_{0.2}Al_{0.8}N$ with the Mo-3 and Mo-6 masks was reduced by thermal annealing. Annealing at 550 °C halved the lateral etch rate with the Mo-3 mask but annealing at 625 °C did not reduce the lateral etch rate any further. Annealing at 700 °C reduced the lateral etch rate to 0.53–0.60 nm/s with both Mo-3 and Mo-6 masks, whereas with the Mo-7 mask the lateral etch rate was slightly increased to 0.45 nm/s. Annealing at 900 °C caused grain coarsening in the Mo-3 mask, which increased the lateral etch rate (Figure 29b).

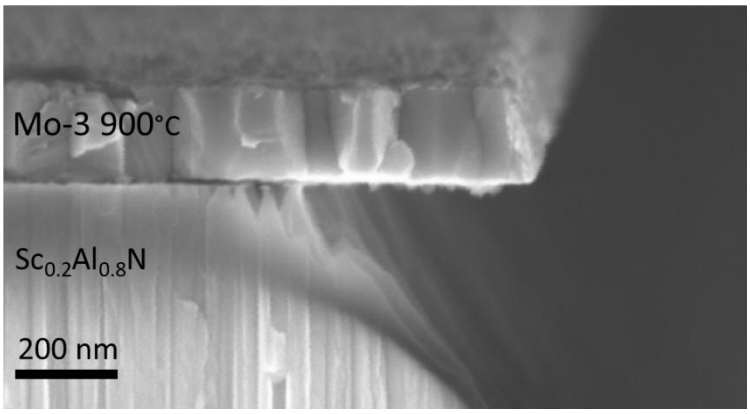

Figure 29. $Sc_{0.2}Al_{0.8}N$ with a Mo mask annealed at 900 °C resulting in Mo grain coarsening and increased lateral etch rate.

The effective lateral etching activation energy was 63±5 kJ/mol with the Mo-3 mask (Figure 30c) both as deposited and after annealing at 550 °C. This was very close to the activation energy of the vertical etching, and the selectivity could not be increased by reducing the etching temperature. Thermal annealing at 700 °C increased the effective lateral etching activation energy to 77±5 kJ/mol with the Mo-3 mask. However, as annealing at 700 °C also increased the full film removal time at low etching temperatures, decreasing the etching temperature could not be used for reducing the lateral etching any further. Instead, the increased effective lateral

etching activation energy and increased full film removal time were likely linked in this case. With the Mo-7 mask, the effective lateral etching activation energy was also 78±5 kJ/mol. In this case, the higher activation energy enabled etching the film fully with only 35 nm of undercut by using an etching temperature of 21 °C (Figure 30b).

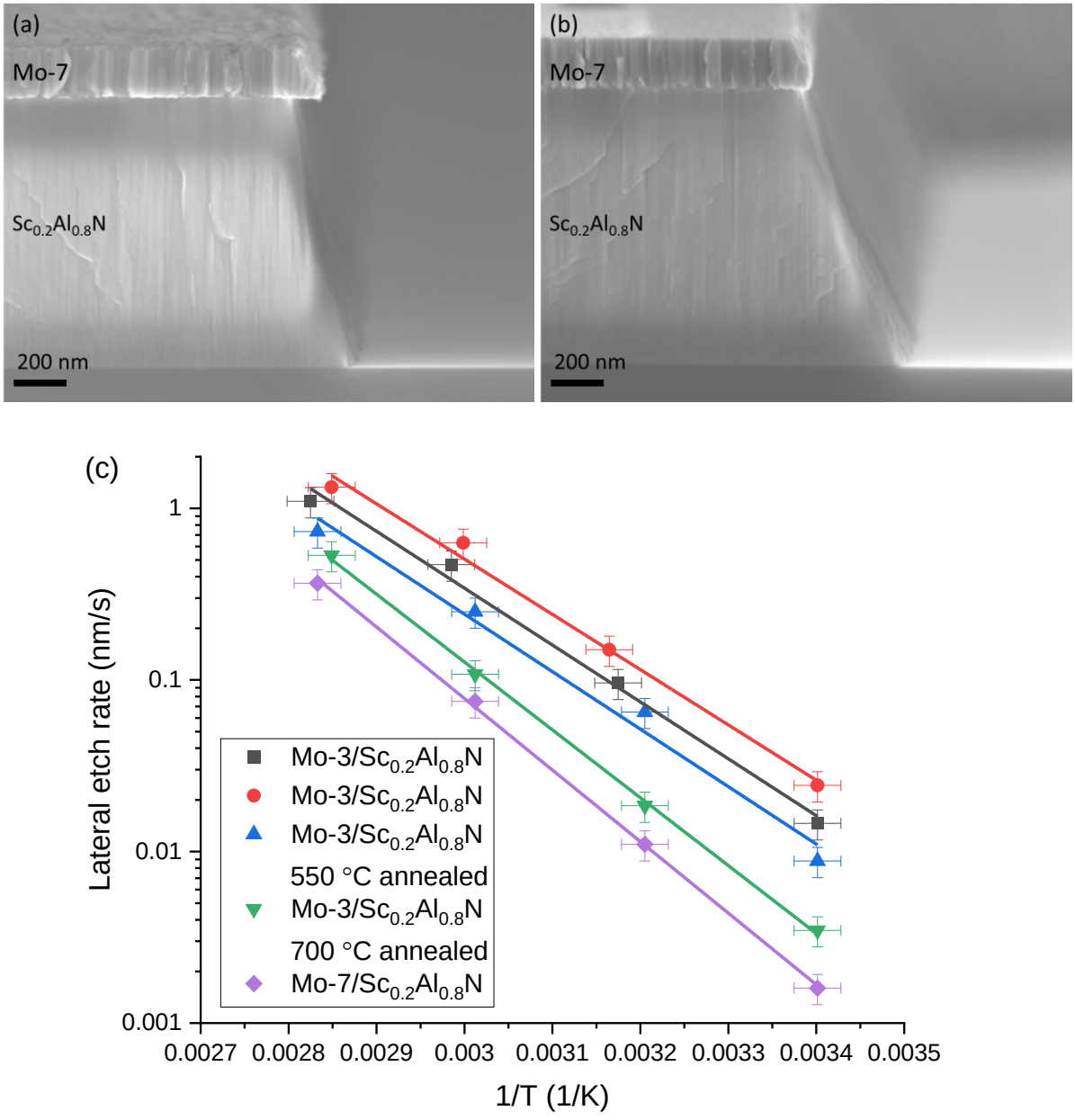

Figure 30. $Sc_{0.2}Al_{0.8}N$ with the Mo-7 mask etched at (a) 80 °C for 5 min, (b) 21 °C for 6 h. (c) Lateral etch rate of $Sc_{0.2}Al_{0.8}N$ at temperatures of about 80, 60, 40 and 21 °C with the Mo-3 mask (2 samples), the Mo-3 mask annealed at 550 ° and 700 °C, and the Mo-7 mask.

Four additional masks were tested for the patterning of $Sc_{0.2}Al_{0.8}N$ films: SiO_2 deposited from SiH_4, SiO_2 deposited from TEOS, SiN_x, and TiO_2. The lateral etch rates with all these masks were strikingly similar at 2.0–3.0 nm/s. Also, annealing at 700 °C reduced the lateral etch rate

with all the masks to 0.57–0.73 nm/s. SiO_2 (SiH_4) was additionally tested after annealing at 550 and 900 °C. Already the lower annealing temperature was enough to reduce the lateral etch rate to 0.60 nm/s and annealing at 700 or 900 °C did not produce significantly different results. The effective lateral etching activation energy was 68±5 kJ/mol both with the SiO_2 (TEOS) mask and SiO_2 (SiH_4) mask annealed at 550 °C, and again it was increased to 77±5 kJ/mol upon annealing at 700 °C (Figure 31).

Table 6. Lateral etch rates (nm/s) of $Sc_{0.2}Al_{0.8}N$ with different mask materials at 80 °C with 5 min etch time.

	SiO_2 (SiH_4)	SiO_2 (TEOS)	SiN_x	TiO_2
As deposited	2.0-2.4	1.9	2.5	3.0
Annealed at 550 °C	0.60			
Annealed at 700 °C	0.60	0.73	0.57	0.73
Annealed at 900 °C	0.53			

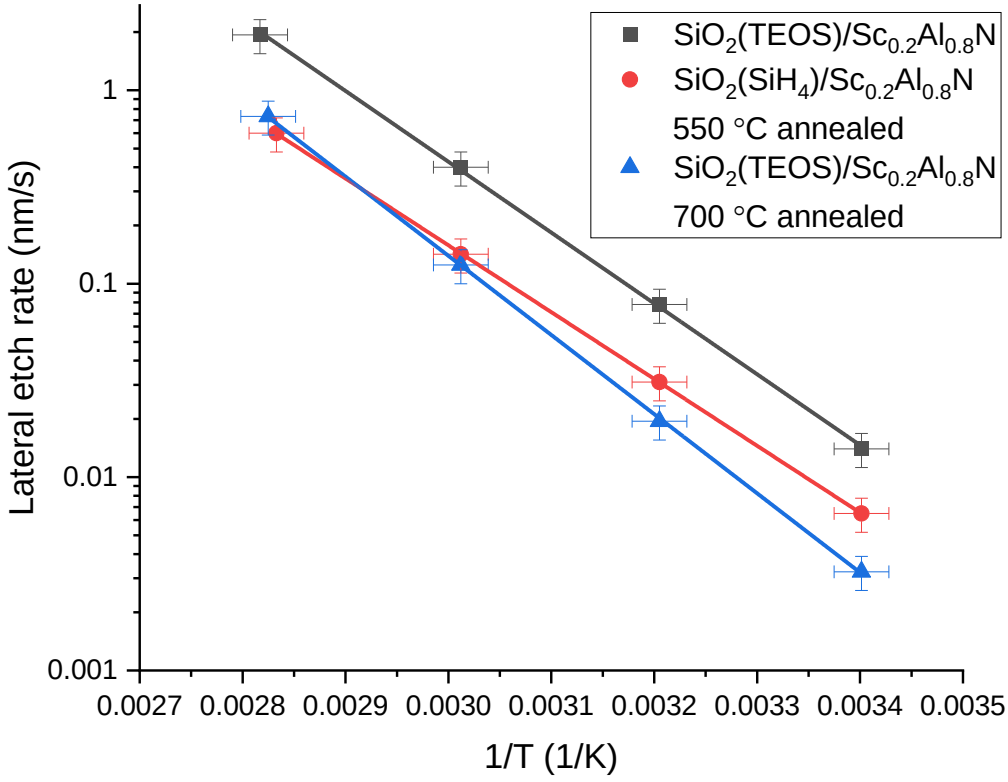

Figure 31. Lateral etch rates of $Sc_{0.2}Al_{0.8}N$ at temperatures of about 80, 60, 40 and 21 °C with the SiO_2 (TEOS) mask as-deposited and annealed at 700 °C, and the SiO_2 (SiH_4) mask annealed at 550 °C.

Thermal annealing caused significant compressive stress to $Sc_{0.2}Al_{0.8}N$ films (Figure 32). Annealing at 550 °C changed the stress by –80 MPa, annealing at 700 °C changed the film stress by –350 to –500 MPa and annealing at 900 °C changed it by approximately –800 MPa. As a reference, the film stress after deposition should preferably be in the range of ±100 MPa, meaning that the stress caused by annealing at 700 °C would be unacceptable in many applications.

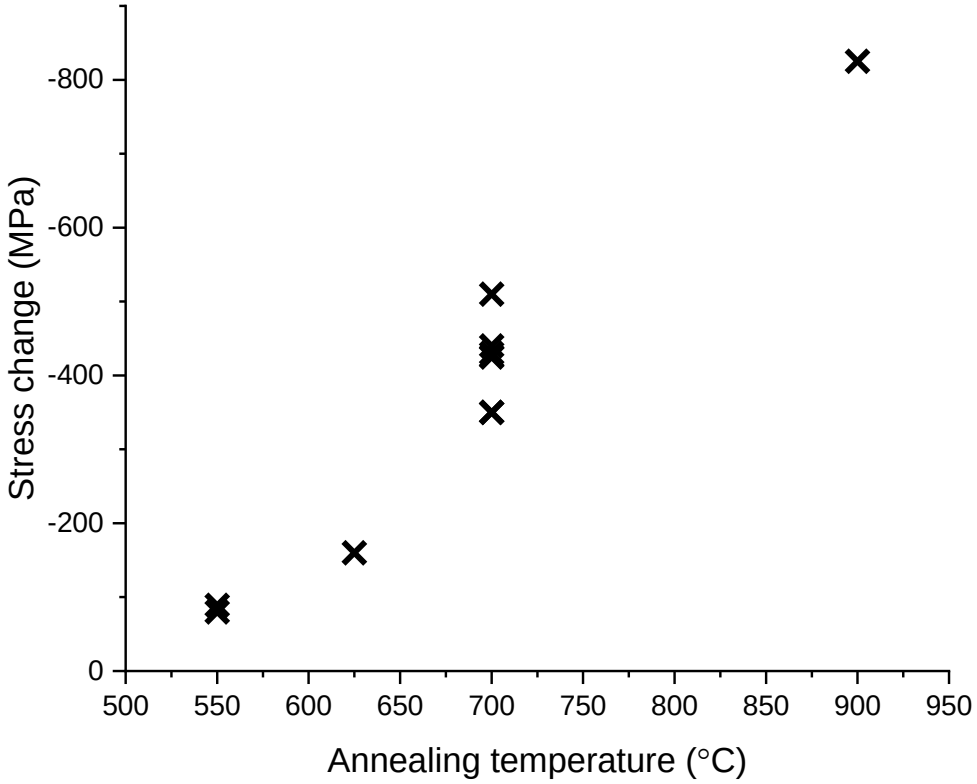

Figure 32. Stress changes of $Sc_{0.2}Al_{0.8}N$ films at different annealing temperatures.

The sidewall angles of the etched $Sc_{0.2}Al_{0.8}N$ structures followed the crystalline planes, but it also partially depended on the lateral etch rate. With the non-annealed films, the sidewall angle was 56–58° corresponding to the {10–1–1} planes (Figure 33a). With annealed films, the sidewall angle was steeper at 75–80° (Figure 33b, c). From the front, etched $Sc_{0.2}Al_{0.8}N$ films exhibited a more columnar and less conical structure (Figure 33c) compared to AlN (Figure 24c). Together with the more even vertical etching, the variation in sidewall angle suggests that the {10–1–1} planes of $Sc_{0.2}Al_{0.8}N$ do not have such low surface energy compared to the other planes under these conditions as is the case with AlN.

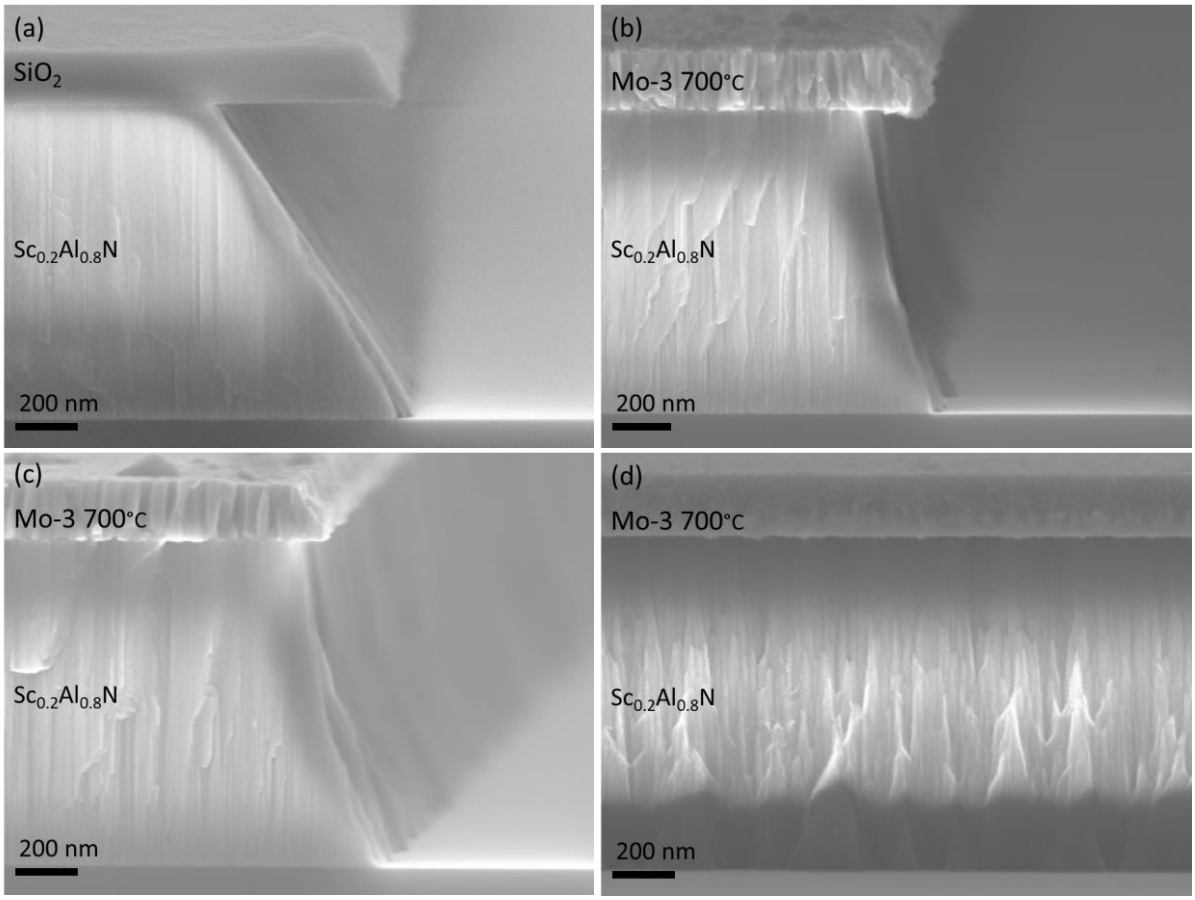

Figure 33. (a) $Sc_{0.2}Al_{0.8}N$ with the SiO_2 mask etched at 80 °C for 5 min. $Sc_{0.2}Al_{0.8}N$ with the Mo-3 mask annealed at 700 °C and etched at (b) 80 °C for 5 min, and (c) 40 °C for 90 min. (d) Annealed and etched $Sc_{0.2}Al_{0.8}N$ viewed from the front.

The lateral etching of $Sc_{0.2}Al_{0.8}N$ also exhibited some time dependence, although it was weaker compared to AlN. The lateral etching started once the vertical etching of the film was finished, meaning about 40 s at 80 °C.

The uniformity of the lateral etching was also examined. With the SiO_2 and annealed Mo-3 masks, the lateral etch rate did not vary at different positions on the substrate. However, with the as-deposited Mo-3 masks, the lateral etch rate increased with increasing distance from the wafer centre, nearly doubling in the worst case (Figure 34). This was likely due to nonuniformity in the plasma cleaning step. In all cases, the standard deviation of measurements made from the same area was typically around 5% indicating little local variation.

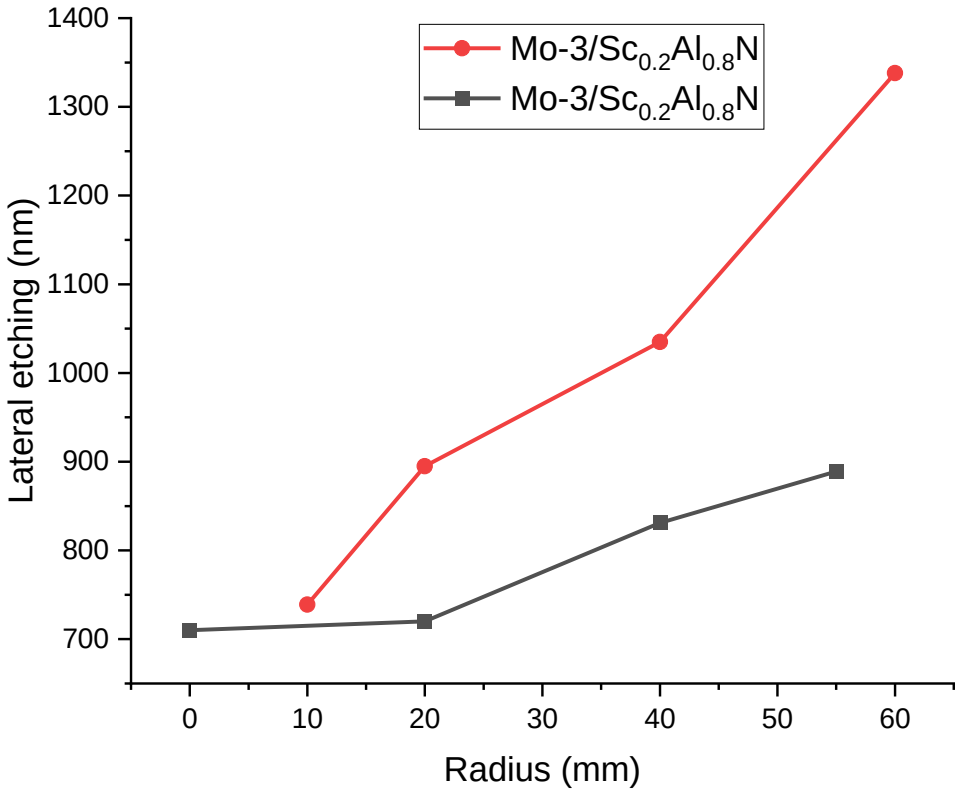

Figure 34. The lateral etching of $Sc_{0.2}Al_{0.8}N$ with the Mo-3 mask at different radii from wafer centre for two different samples. Etching temperature was 80 °C and time was 5 min.

10.5. TOF-ERDA and SIMS measurements

Surface oxidation of $Sc_{0.2}Al_{0.8}N$ was examined with a combination of TOF-ERDA and SIMS. In TOF-ERDA, a sample is bombarded with heavy and very high energy ions at a shallow angle. These ions penetrate micrometres into the sample and collide elastically with sample atoms causing them to recoil. The time-of-flight and energy of these recoiled atoms is measured which yields their mass as a function of energy. The atoms lose energy as they travel through the sample which allows calculating the depth profiles of the elements. TOF-ERDA gives the elemental composition quantitively and accurately to depths of several hundreds of nanometres, and it can measure all elements including hydrogen. It is an extremely powerful analytical technique, but it requires a specialized high-energy particle accelerator making it scarcely available.

In SIMS, a sample is sputtered with an ion beam. Some of the sputtered material is ionized, and those ions are measured. SIMS does not give quantitative information about the elements, as

their probability of ionization depends on the matrix. SIMS also enables depth profiling, and it has higher sensitivity compared to TOF-ERDA.

The samples were from the same wafers as used for the etching experiments, meaning they were patterned. However, this did not have any significant impact on the results. A $Sc_{0.2}Al_{0.8}N$ reference sample and Mo-5/$Sc_{0.2}Al_{0.8}N$ were measured with TOF-ERDA, as they were expected to have higher concentrations of oxygen compared to the other samples. SIMS was used to measure the $Sc_{0.2}Al_{0.8}N$ reference sample, as well as $Sc_{0.2}Al_{0.8}N$ with the Mo-3 (2 samples), Mo-5 (as deposited and annealed at 550 °C), Mo-6 and Mo-7 masks. The Mo-5 samples were taken from the same wafer meaning the annealing was done after film patterning. Therefore, the etching results of the 550 °C annealed Mo-5 sample are lacking.

The TOF-ERDA measurements showed little impurities in the $Sc_{0.2}Al_{0.8}N$ and Mo films, except on the film surface. The $Sc_{0.2}Al_{0.8}N$ film had only 19.2±0.3 % Sc compared to the 20 atom-% expected and the ratio of (Al+Sc)/N was 0.97 (Table 7). The $Sc_{0.2}Al_{0.8}N$ surface had much higher oxygen concentration, corresponding to approximately 7 nm of surface oxide with both samples (Figure 35a, b).

Table 7. TOF-ERDA measurement results of a reference $Sc_{0.2}Al_{0.8}N$ film with the surface excluded, and surface impurity concentrations.

	film (atom-%)	surface (10^{15} atoms/cm^2)
Al	39.53±0.15	
N	50.4±0.2	
Sc	9.41±0.12	
H	0.24±0.03	5.16
O	0.37±0.03	32.14
C	<0.01	0.11

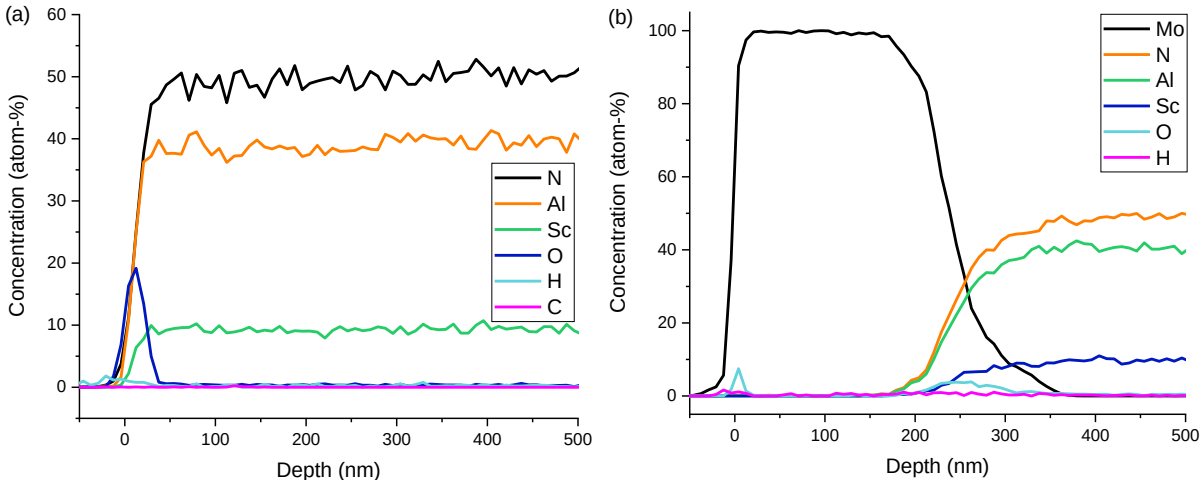

Figure 35. TOF-ERDA elemental depth profiles of (a) a $Sc_{0.2}Al_{0.8}N$ film and (b) Mo-5/$Sc_{0.2}Al_{0.8}N$ sample.

Figure 36 shows raw data of the SIMS measurements of $Sc_{0.2}Al_{0.8}N$ with the Mo-5 and Mo-7 masks. The Mo-5/$Sc_{0.2}Al_{0.8}N$ sample showed strong oxygen peak at the Mo/$Sc_{0.2}Al_{0.8}N$ interface. There was also increased amounts of hydrogen and carbon at the interface, and a strong fluorine peak. However, this was an equal sample to the one analysed by TOF-ERDA, which did not show any fluorine, and therefore the fluorine concentration was assumed to be negligible. The SIMS measurements did not give any substantial Mo-signal from the Mo-layer and only a small Mo-peak was seen on the Mo/$Sc_{0.2}Al_{0.8}N$ interface.

The SIMS results were further analysed by normalising them with the bulk Al-signal of the respective samples. With the Mo-3 and Mo-5 masks, the Al-signal increased slower compared to the Mo-6 and Mo-7 masks (Figure 37a). This was likely due to reduced sputtering rate of the interface oxide. Despite the plasma clean included in the Mo-3 process, both Mo-3 samples had high amounts of oxide at Mo/$Sc_{0.2}Al_{0.8}N$ interface (Figure 37b). First sample, which also had a high lateral etch rate of 2.7 nm/s, had approximately half of the oxide compared to the Mo-5 sample. Second Mo-3 sample with a lateral etch rate of only 1.1 nm/s had approximately one quarter of the oxide compared to the Mo-5 mask. This difference in the interface oxide may be an explanation for the varying etch rates with the Mo-3 masks. With the Mo-6 and Mo-7 masks there was only very minor interface oxide demonstrating that the plasma cleaning did not cause significant additional oxidation.

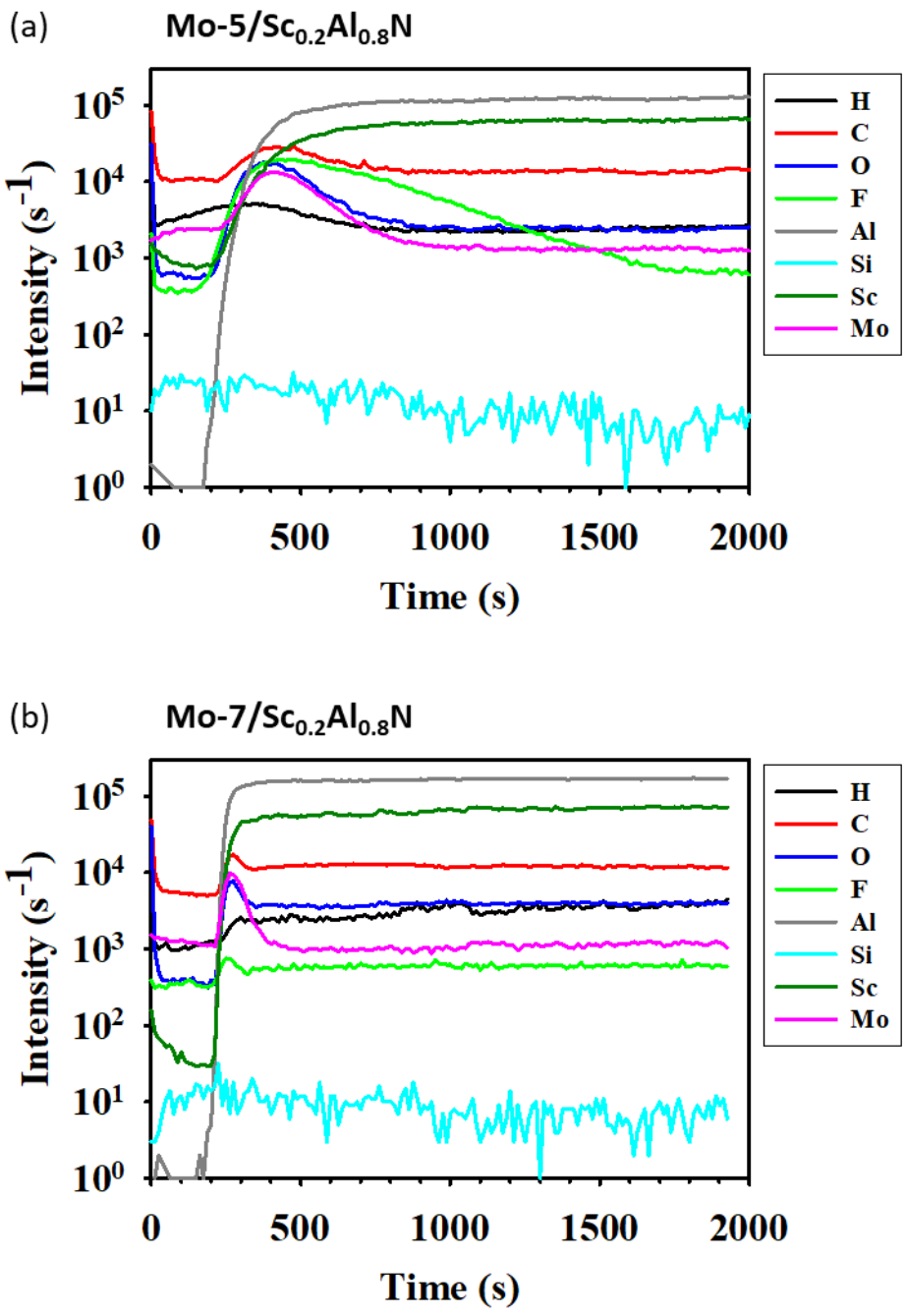

Figure 36. SIMS elemental depth profiles of $Sc_{0.2}Al_{0.8}N$ with (a) Mo-5 and (b) Mo-7 masks.

With most samples, there was little excess hydrogen at the interface compared to the bulk of the film (Figure 37c). A clear hydrogen peak was only seen with the Mo-5 mask. However, there might have also been excess hydrogen with the Mo-3 samples if the peak was masked by the oxide layer and reduced sputtering rate. The Mo-3 sample with high lateral etch rate had much higher amount of hydrogen compared to the other samples, but this could be due to

measurement error as it was the first sample measured. Annealing at 550 °C reduced the hydrogen concentration with the Mo-5 mask by about 75 %.

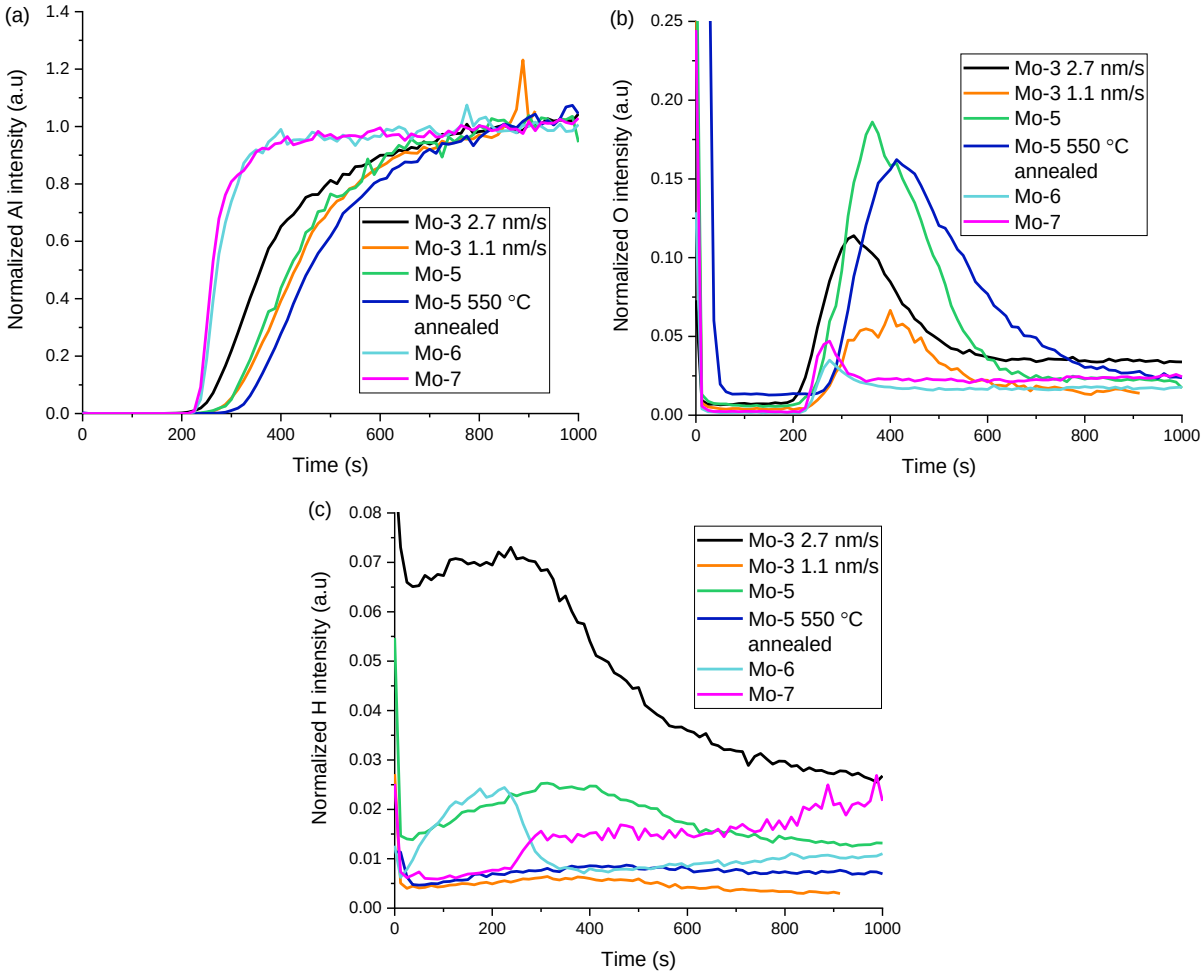

Figure 37. (a) Normalized Al-signal, (b) O-signal, and (c) H-signal of the different samples measured with SIMS.

10.6. Etching of AlN and $Sc_{0.2}Al_{0.8}N$ with H_3PO_4 and H_2SO_4

Etching of AlN and $Sc_{0.2}Al_{0.8}N$ films with the Mo-3 and SiO_2 masks was also studied with 85 % (14.8 mol/l) H_3PO_4 and 4.5 mol/l H_2SO_4 at 80 °C. Etching of both films was significantly slower with the acidic solutions compared to the TMAH. Table 8 summarizes the results of the acid etching.

With H_3PO_4, the etch rate of AlN was about 8–9 nm/s. Etching AlN with a Mo-3 mask for 10 min resulted in the film being completely removed, and the resulting undercut was 50 nm or less. With 1 h etching time the undercut was about 1 µm, which corresponds to a lateral etch rate of 0.28 nm/s. Again, there was significant time dependence as with the short time the lateral

etching was smaller than expected based on the lateral etch rate with the longer time. The SiO_2 mask did not perform as well and it had a lateral etch rate of 1.2 nm/s, which resulted in 700 nm undercut in 10 minutes.

The vertical etch rate of $Sc_{0.2}Al_{0.8}N$ with H_3PO_4 was about 3 nm/s, and with the Mo-3 mask, the lateral etch rate was 5.4 nm/s. The undercut would have been approximately 10 µm for the time required to completely etch the film (Figure 38). With the SiO_2 mask, the lateral etch rate was still 50 % higher at 8.3 nm/s. Thermal annealing at 700 °C reduced the lateral etch rate with Mo-3 to 1.6 nm/s and with SiO_2 to 0.68 nm/s.

Etching with 4.5 mol/l H_2SO_4 was still 10–20 times slower compared to the H_3PO_4. With AlN, removal of the visible film took approximately 30 minutes, corresponding to an etch rate of 0.5 nm/s. Lateral etch rates were 0.017 nm/s with the Mo-3 and 0.05 nm/s with the SiO_2 masks. For $Sc_{0.2}Al_{0.8}N$, the vertical etch rate was 0.31 nm/s and the lateral etch rate was 0.28 nm/s with the Mo-3 mask.

Table 8. Summary of acid etching of 1 µm AlN and $Sc_{0.2}Al_{0.8}N$ films. ([a]Values were estimated by extrapolating from the experimental data, [b]sidewall angle in the annealed sample).

	Mo-3/AlN	SiO_2/AlN	Mo-3/ $Sc_{0.2}Al_{0.8}N$	SiO_2/ $Sc_{0.2}Al_{0.8}N$
H_3PO_4 vertical etch rate (nm/s)	8.3	8.3	2.8	2.8
Full film removal time (min)	10	10	30[a]	30[a]
Undercut with full film removal (nm)	50	700	10000[a]	15000[a]
Sidewall angle (°)	55	55	44[b]	46[b]
H_2SO_4 vertical etch rate (nm/s)	0.5	0.5	0.28	
Full film removal time (min)	180[a]	180[a]	300[a]	
Undercut with full film removal (nm)	180[a]	540[a]	5500[a]	
Sidewall angle (°)	40	40	26	

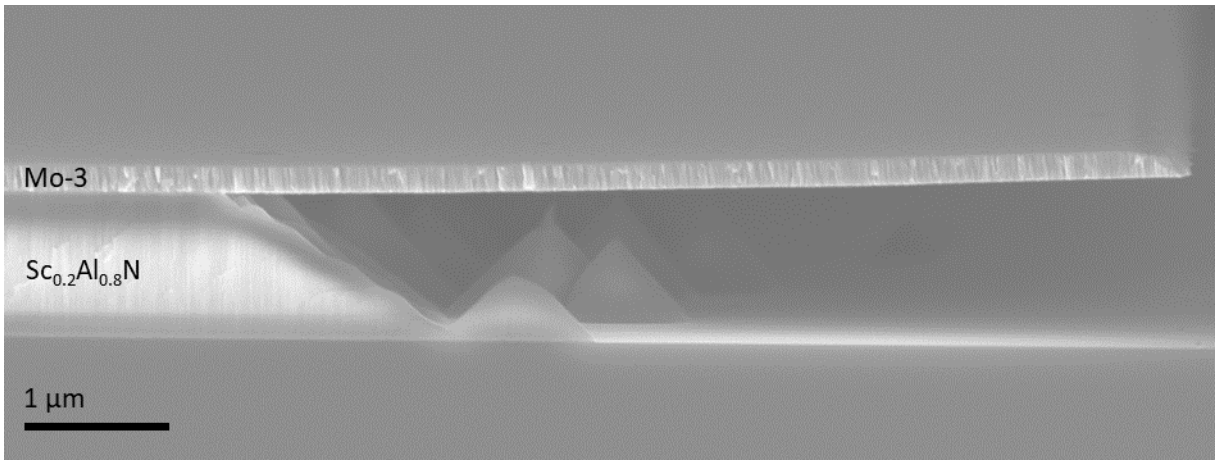

Figure 38. $Sc_{0.2}Al_{0.8}N$ film etched with H_3PO_4 for 20 min resulting in large lateral etching.

Surprisingly, the sidewall angles were different compared to the TMAH etching. When AlN was etched with H_3PO_4, the sidewall angle was approximately 54–56 ° (Figure 39a), so slightly smaller compared to TMAH. With H_2SO_4, the angle was noticeably smaller at approximately 40 ° (Figure 39b). With $Sc_{0.2}Al_{0.8}N$, the angles were approximately 30 and 25–27 ° for H_3PO_4 and H_2SO_4, respectively (Figure 38, Figure 39c). With H_3PO_4, the shallow sidewall was likely caused by the very high lateral etch rate, as with the annealed samples the sidewall was steeper at 42-48 °. This is also seen in Figure 38 where the cones have steeper sidewalls compared to the masked material. However, with H_2SO_4 the small sidewall angle of 25–27 ° occurred both at the mask edges as well as at the cones.

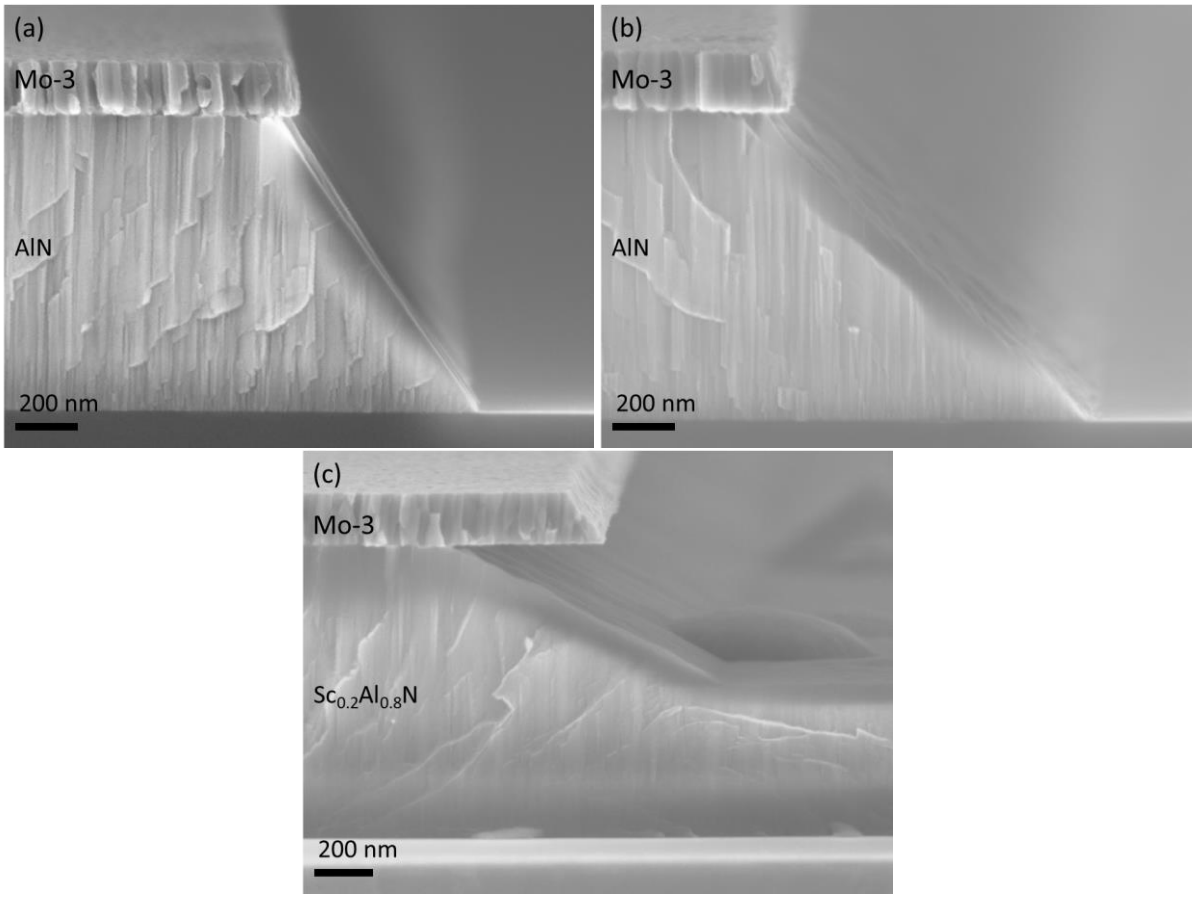

Figure 39. AlN etched with (a) H_3PO_4 for 10 min, (b) H_2SO_4 for 90 min, and (c) $Sc_{0.2}Al_{0.8}N$ etched with H_2SO_4 for 30 min.

10.7. Scandium residue

Scandium is poorly soluble in alkaline solutions which led to the deposition of $ScO_x(OH)_y$-residue on the wafer surface (Figure 40). The composition of the residue was investigated with EDX, but the stoichiometry could not be determined. The residue was measured to contain only scandium and oxygen, as hydrogen cannot be measured with EDX.

All experiments where the residue deposition was investigated were conducted at 80 °C. The residue deposition depended significantly on the sample size and the rinsing of the samples. With smaller 1/8 wafer pieces, deposition was rarely observed. However, with full wafers, the residue was consistently observed on most samples. When a dump rinse was used, which quickly drained and refilled the rinsing bath, large amount of residue was deposited on the lower side of the wafer. Rinsing by overflowing the bath with water coming from the bottom resulted in much less residue. The residue could not be avoided with strong stirring during the etching. The amount of the residue did not depend on the amount of scandium already present in the

TMAH solution. The residue could be partially removed by etching the sample again with TMAH for a short time (30 s) indicating that the residue was slightly soluble in TMAH.

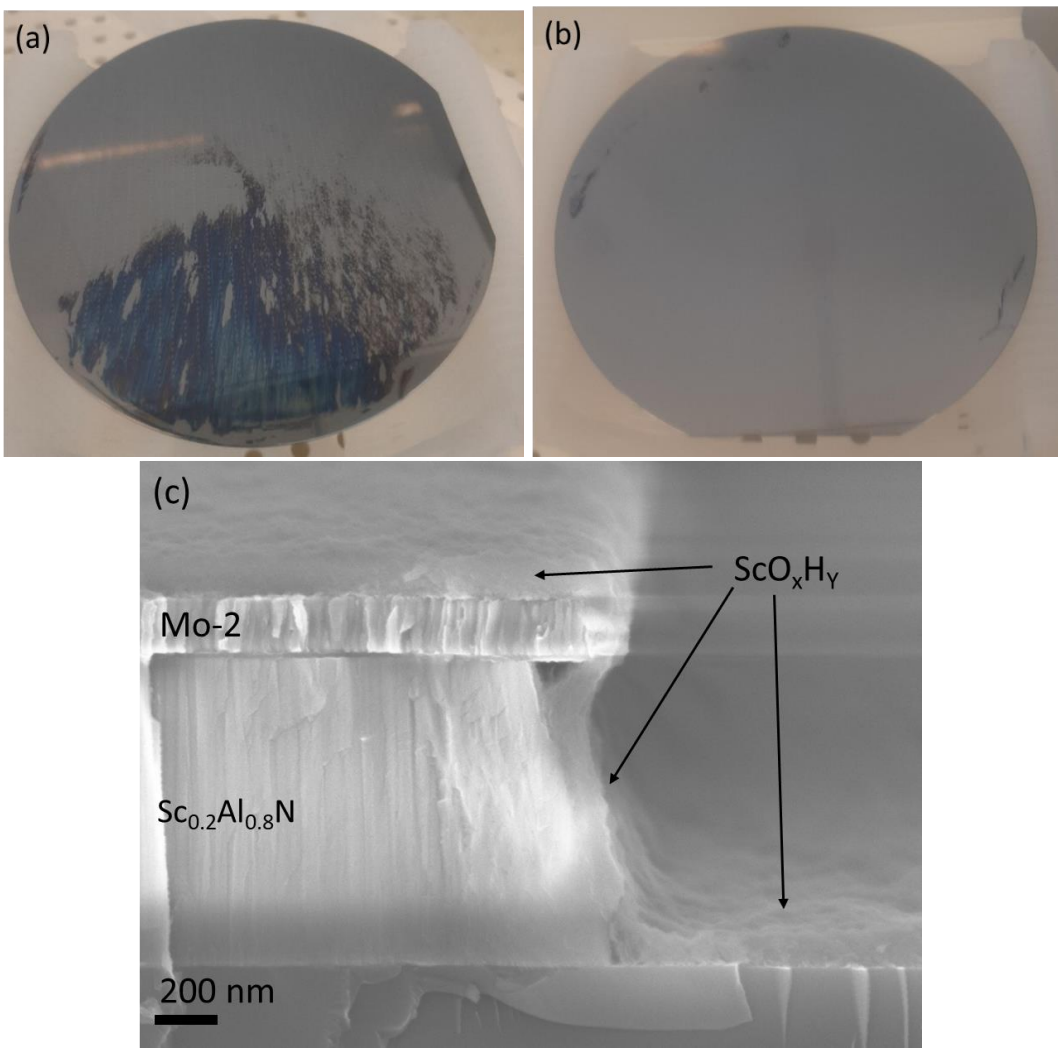

Figure 40. $ScO_x(OH)_y$-residue on a wafer surface after etching and (a) dump rinse or (b) overflow rinse. (c) Cross-sectional image of etched $Sc_{0.2}Al_{0.8}N$ with an uniform 150 nm thick $ScO_x(OH)_y$ layer.

The use of chelation was tested for preventing the residue deposition by adding EDTA to the TMAH. However, even with a large excess of EDTA, it did not form a strong enough chelate with Sc and there still was significant residue deposition. Therefore, a separate cleaning step was developed instead. The $ScO_x(OH)_y$-residue was easily soluble even in weakly acidic solutions. Its removal was tested with the following solutions: 1 % HF, buffered HF (1:7 solution of 50 % HF and 45 % NH_4F), 0.1 % HCl, 0.1 % H_3PO_4 and the standard cleaning solution 1 (SC-1, 1:1:5 solution of 25 % NH_4OH, 30 % H_2O_2, and DI water). All acids dissolved the residue within seconds or minutes at room temperature, but the SC-1 solution had no effect.

11. Discussion and conclusions

Etching of $Sc_xAl_{1-x}N$ presents challenges for both wet and dry etching techniques. Many of the issues related to the wet etching were investigated in the experimental work, and techniques for high-fidelity patterning of $Sc_xAl_{1-x}N$ were developed.

11.1. Discussion on results

The anisotropic wet etching of AlN and $Sc_{0.2}Al_{0.8}N$ films deposited with reactive magnetron sputtering was analysed with three etchants: TMAH, H_3PO_4 and H_2SO_4. TMAH performed clearly the best, and the etching process was further developed with it. The etching was investigated with several different etch masks to identify the mechanisms of mask undercutting during the etching. The masks were Mo deposited by sputtering, SiO_2 and SiN_x deposited with PECVD, and TiO_2 deposited with ALD.

The addition of Sc to AlN changed the etching of the material significantly and reduced the etch rate. This could be due to the lower solubility of Sc, but also due to microstructural effects, such as accumulation of Sc at the grain boundaries. With TMAH at 80 °C, etching through the 1 µm AlN film took only 3 s corresponding to an etch rate of 300 nm/s. Etching of $Sc_{0.2}Al_{0.8}N$ was about ten times slower at 20–30 nm/s. During etching, AlN formed steep cones very rapidly, while the etching of $Sc_{0.2}Al_{0.8}N$ was even, except for the cones formed around AOGs. Removing all cones took approximately ten times longer than etching through the film with both materials. The etch rates and full film removal times measured for AlN and $Sc_{0.2}Al_{0.8}N$ were comparable to those reported previously.

In this work, cones occurred only around AOGs during the etching of $Sc_{0.2}Al_{0.8}N$ films. However, a previous study found the etching behaviour of $Sc_xAl_{1-x}N$ to be similar to AlN.[18] There occurred a much higher number of cones which were not linked to AOGs. This indicates that there may be other mechanisms that result in cone formation during the etching of $Sc_xAl_{1-x}N$.

The more even etching with $Sc_{0.2}Al_{0.8}N$ compared to AlN indicated lower chemical stability and surface energy of the {10–1–1} planes in relation to the other crystalline planes. Also, the sidewall angle could be controlled to some degree by controlling the lateral etch rate, and it was not limited to 59 ° like with AlN.

Due to the formation of the cones, determining the etch rate of AlN is nearly meaningless. The time required for full film removal is a more meaningful measure, as it represents the actual time to etch the film. However, for $Sc_{0.2}Al_{0.8}N$, also the etch rate also yields some meaningful information as the film is etched evenly for the most part.

The rate of mask undercutting was similar with both AlN and $Sc_{0.2}Al_{0.8}N$ at 2–3 nm/s with most masks when etched with TMAH at 80 °C. This resulted in lateral etching of 600–900 nm with $Sc_{0.2}Al_{0.8}N$, while the issue was much smaller with AlN due to the faster vertical etch rate. Best results with a lateral etch rate of 0.36 nm/s were obtained when a Mo mask was deposited on $Sc_{0.2}Al_{0.8}N$ so that the $Sc_{0.2}Al_{0.8}N$ was not exposed to air or ion bombardment.

The results on the lateral etching of AlN and $Sc_{0.2}Al_{0.8}N$ indicate there being two mechanisms behind it: surface modification of the AlN or $Sc_{0.2}Al_{0.8}N$ film by oxidation or damage due to a plasma cleaning process. With the Mo-1, Mo-3, Mo-4 and Mo-6 masks, the lateral etching was mostly caused by surface damage, while oxidation was to blame with all other masks. TOF-ERDA showed a 7 nm oxide layer on untreated $Sc_{0.2}Al_{0.8}N$. When no plasma cleaning was used, the mask material or its deposition technique likely had very little effect on the oxide, which explains the similarity of the lateral etch rates.

When a plasma cleaning process was used with the aim of removing the interface oxide, it caused surface damage to the AlN or $Sc_{0.2}Al_{0.8}N$ film resulting in increased lateral etching. The lateral etch rate was increased more with heavier ion bombardment, and the best results occurred when all surface modifications were eliminated in the Mo-7 process. These results were further backed by SIMS measurements. With the Mo-6 mask, no additional oxidation was caused by the plasma clean compared to the Mo-7 mask which confirms ion bombardment as the cause. Also, the SIMS measurements indicated that a short plasma cleaning step was not sufficient for removing all the surface oxide. More work is needed to develop a plasma cleaning process that would remove all surface oxide on $Sc_xAl_{1-x}N$ while resulting in minimal surface damage.

Thermal annealing after the mask deposition was an effective technique for reducing the lateral etching by up to a factor of five. Again, the lateral etch rates after annealing were very similar with different mask materials. With the SiO_2 masks where the film was exposed to air but no ion bombardment, annealing at 550 °C hardened the interface oxide to etching. However, annealing at 700 °C was required to negate the effect of the surface damage with the AlN and $Sc_{0.2}Al_{0.8}N$ films exposed to ion bombardment. No further improvement occurred with

annealing at higher temperatures. The hydrogen concentration of the $Sc_{0.2}Al_{0.8}N$ film with the Mo-5 mask was reduced by the annealing, which might have been indicative of hardening of the oxide. Unfortunately, the lateral etch rate of $Sc_{0.2}Al_{0.8}N$ film with the 550 °C annealed Mo-5 mask could not be investigated. It is expected that etching behaviour of $Sc_{0.2}Al_{0.8}N$ with an annealed Mo-5 mask would have been similar to the annealed SiO_2 mask.

Based on the results, using a two-layer mask with an adhesion layer below a Mo mask should not offer any benefits. The adhesion layer would protect the surface and native oxide on the AlN or $Sc_xAl_{1-x}N$ from any ion bombardment, meaning it should be equivalent to the Mo-5 process where the plasma cleaning was not applied.

Thermal annealing of $Sc_{0.2}Al_{0.8}N$ caused large compressive stress in the film, especially at 700 °C, while no such changes occurred with AlN. This was quite surprising, as annealing could be expected to cause the films to become denser and result in tensile stress. It is unknown why exactly the stress was developed. In a previous study, the lattice constant *c* of sputtered $Sc_xAl_{1-x}N$ on sapphire was found to decrease with thermal annealing.[93] However, the lattice constant *a* did not change, and the stress did not change significantly when $Sc_xAl_{1-x}N$ on Si was annealed.[93] Still, it is possible that annealing changed the lattice constant *a* of the films used in this work.

Unexpectedly, the acidic etchants had about ten times higher lateral etch rates with $Sc_{0.2}Al_{0.8}N$ compared to AlN. This was in stark contrast to the TMAH, where the lateral etch rates were very close. While this means that $Sc_{0.2}Al_{0.8}N$ cannot be effectively patterned with acids, the high lateral etch rate could enable some niche applications with $Sc_xAl_{1-x}N$ as a sacrificial layer. H_3PO_4 is a poor etchant for nearly all other materials in MEMS manufacturing, but it etched $Sc_{0.2}Al_{0.8}N$ laterally at a rate of over 8 nm/s.

Etching $Sc_{0.2}Al_{0.8}N$ with TMAH often resulted in the deposition of $ScO_x(OH)_y$ -residue on the wafer surface. Using an overflow rinse resulted in lower residue deposition compared to using a dump rinse. The residue was also partially dissolved with repeated etching in TMAH. This indicated that the residue deposition occurred during the rinsing. Likely, the Sc-ions were trapped at the boundary layer during the TMAH etching. A possible mechanism was that due to the poor solubility of Sc, it formed a $ScO_x(OH)_y(H_2O)_z$ gel layer which did not prevent the etching but prevented the diffusion of the Sc-ions away from near the wafer surface. Experiments regarding the residue deposition were only done at 80 °C meaning that using a lower etching temperature could also affect the residue deposition.

Chelation with EDTA was found not to be effective due to the very alkaline conditions favouring the formation of $ScO_x(OH)_y$ over the EDTA complex. Using stronger chelation agents may prevent the precipitation of Sc, but this was not tested as an acid cleaning step was determined to be more practical and reliable.

11.2. Designing an etching process

Choosing the right etchant is the first step in development of an AlN or $Sc_xAl_{1-x}N$ etching process. Overall, TMAH was a much better etchant compared to H_3PO_4 or H_2SO_4. It offered a much higher vertical etch rate and higher selectivity between vertical and lateral etching. Based on this, also NaOH and KOH are potential candidates for etching of AlN and $Sc_xAl_{1-x}N$. However, they cause alkali metal contamination which can be intolerable. On the other hand, they are cheaper and not toxic like TMAH.

Secondly, the etching time needs to be optimized to be as short as possible while still removing the film. Also, a lower film thickness enables faster removal of the film resulting in less undercut. For some applications, removing all of the cones may not be necessary, which would also allow shortening the etching time.

The activation energies for lateral and vertical etching were similar in most cases with both AlN and $Sc_{0.2}Al_{0.8}N$. Therefore, the etching temperature can often be chosen freely with little effect on the undercut if the etching time is adjusted accordingly. Lower etching temperature is beneficial for the lifetime of the etching solution and power consumption.

The quality of the AlN or $Sc_xAl_{1-x}N$ film is important not only for the piezoelectric properties, but also for the etching characteristics. With AlN, the lateral etch rate of the film was increased if the film quality was very poor. However, these films would also likely be unsuitable for device applications. With $Sc_xAl_{1-x}N$, the more AOGs the film had, the more cones were formed. If the number of AOGs is minimized, it could enable reducing the etching time.

The mask material and its deposition technique are relatively unimportant for minimising the lateral etching. More important factors are surface oxidation of the AlN or $Sc_xAl_{1-x}N$ film, ion bombardment before the mask deposition and the deposition temperature of the mask. Increased deposition temperature would likely act like an annealing, while ion bombardment was demonstrated to cause surface damage and increase lateral etching. In an optimal process,

exposing the AlN and $Sc_xAl_{1-x}N$ to both air and ion bombardment should be avoided before the etch mask deposition.

Thermal annealing was an effective method for reducing undercutting with both AlN and $Sc_{0.2}Al_{0.8}N$ films regardless of the mask material. Additionally, annealing has been shown to enhance the piezoelectric properties of $Sc_xAl_{1-x}N$, which makes adding an annealing step even more attractive.[61,93–96] The annealing temperature should be optimized for minimizing the lateral etching while maximizing the piezoelectric response. Still, the generation of stress must be avoided. Also, compressive stress is often more disadvantageous than tensile stress, as it is more likely to cause buckling and collapse of thin devices.

The possible appearance of $ScO_x(OH)_y$ residue must be considered. The rinsing should be optimized for minimal residue deposition but additional cleaning may still be required. A preferential option may be rinsing the wafers with acid immediately after the alkaline etchant, as this could avoid any possibility of generating particles during the rinsing step.

One technique for avoiding the limitations of both RIE and wet etching is to combine them. $Sc_xAl_{1-x}N$ can first be etched with RIE almost through, and then the etching can be finished with wet etching. By this way, overetching to the bottom material during RIE is avoided, while the wet etching time is significantly reduced resulting in lower undercutting. Figure 41 demonstrates this method for patterning AlN.

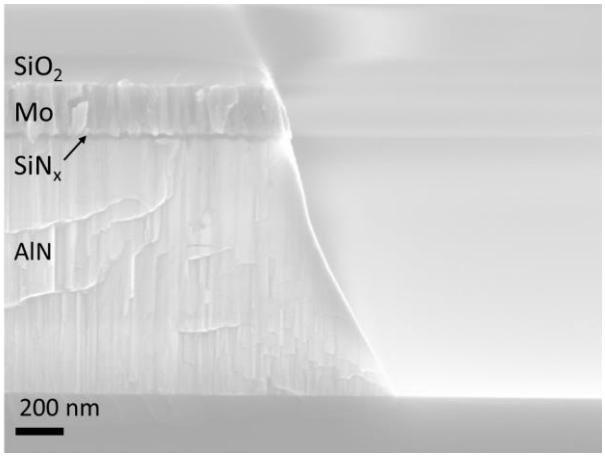

Figure 41. The AlN film was etched first with RIE to a thickness of 300 nm and was finished with TMAH. The RIE was done with a LAM 9600 ICP etcher using Cl_2/BCl_3 plasma.

There are still many questions that should be studied before wet etching is used for patterning AlN or $Sc_xAl_{1-x}N$ in applications where the lateral etching needs to be minimal. Firstly, the effect of the scandium concentration on the etch rate should be studied. Secondly, for device

applications, AlN or $Sc_xAl_{1-x}N$ are typically deposited on a metal bottom electrode. This could affect the etching of the film and formation of cones. Thirdly, the annealing temperature should be optimized for minimizing the lateral etch rate while also optimizing the stress change and piezoelectric properties. Moreover, the origin of stress change during annealing of $Sc_xAl_{1-x}N$ should be studied with varying x and different substrates.

References

1. E. Hartikainen: Magnetron Sputtered Scandium Doped Aluminium Nitride Thin Films with High Scandium Content − Structure and Piezoelectric Properties, M.Sc. thesis, Tampere university, 2021.

2. K. Airola, S. Mertin, J. Likonen, E. Hartikainen, K. Mizohata, J. Dekker, A. T. Sebastian, and T. Pensala: High-fidelity patterning of AlN and ScAlN thin films with wet chemical etching, *Materialia* **22**(March), 101403 (2022). DOI: https://doi.org/10.1016/j.mtla.2022.101403.

3. P. Muralt: AlN Thin Film Processing and Basic Properties, in *Microsystems and Nanosystems* (Springer International publishing, Cham, 2017), pp. 3–37 . DOI: https://doi.org/10.1007/978-3-319-28688-4_1.

4. G. A. Slack, R. A. Tanzilli, R. O. Pohl, and J. W. Vandersande: The intrinsic thermal conductivity of AIN, *J. Phys. Chem. Solids* **48**(7), 641 (1987). DOI: https://doi.org/10.1016/0022-3697(87)90153-3.

5. V. Kaajakari: Practical MEMS (Small Gear Publishing, Las Vegas, 2009).

6. A. Assali, F. Laidoudi, R. Serhane, F. Kanouni, and O. Mezilet: Highly Enhanced Electro-acoustic Properties of YAlN/Sapphire Based Surface Acoustic Wave Devices for Next Generation of Microelectromechanical Systems, *Mater. Today Commun.* **26**(January), 102067 (2021). DOI: https://doi.org/10.1016/j.mtcomm.2021.102067.

7. M. Uehara, Y. Amano, S. A. Anggraini, K. Hirata, H. Yamada, and M. Akiyama: Preparation of YbAlN piezoelectric thin film by sputtering and influence of Yb concentration on properties and crystal structure, *Ceram. Int.* **47**(11), 16029 (2021). DOI: https://doi.org/10.1016/j.ceramint.2021.02.177.

8. H. Liu, F. Zeng, G. Tang, and F. Pan: Enhancement of piezoelectric response of diluted

Ta doped AlN, *Appl. Surf. Sci.* **270**, 225 (2013). DOI: https://doi.org/10.1016/j.apsusc.2013.01.005.

9. K. Hirata, H. Yamada, M. Uehara, S. A. Anggraini, and M. Akiyama: First-Principles Study of Piezoelectric Properties and Bonding Analysis in (Mg, X, Al)N Solid Solutions (X = Nb, Ti, Zr, Hf), *ACS Omega* **4**(12), 15081 (2019). DOI: https://doi.org/10.1021/acsomega.9b01912.

10. M. Akiyama, T. Kamohara, K. Kano, A. Teshigahara, Y. Takeuchi, and N. Kawahara: Enhancement of piezoelectric response in scandium aluminum nitride alloy thin films prepared by dual reactive cosputtering, *Adv. Mater.* **21**(5), 593 (2009). DOI: https://doi.org/10.1002/adma.200802611.

11. K. R. Talley, S. L. Millican, J. Mangum, S. Siol, C. B. Musgrave, B. Gorman, A. M. Holder, A. Zakutayev, and G. L. Brennecka: Implications of heterostructural alloying for enhanced piezoelectric performance of (Al,Sc)N, *Phys. Rev. Mater.* **2**(6), 1 (2018). DOI: https://doi.org/10.1103/PhysRevMaterials.2.063802.

12. O. Zywitzki, T. Modes, S. Barth, H. Bartzsch, and P. Frach: Effect of scandium content on structure and piezoelectric properties of AlScN films deposited by reactive pulse magnetron sputtering, *Surf. Coatings Technol.* **309**, 417 (2017). DOI: https://doi.org/10.1016/j.surfcoat.2016.11.083.

13. R. Petrich, H. Bartsch, K. Tonisch, K. Jaekel, S. Barth, H. Bartzsch, D. Glos, A. Delan, S. Krischok, S. Strehle, M. Hoffmann, and J. Muller: Investigation of ScAlN for piezoelectric and ferroelectric applications, in *2019 22nd European Microelectronics and Packaging Conference & Exhibition (EMPC)* (2019) . DOI: https://doi.org/10.23919/EMPC44848.2019.8951824.

14. S. Fichtner, N. Wolff, G. Krishnamurthy, A. Petraru, S. Bohse, F. Lofink, S. Chemnitz, H. Kohlstedt, L. Kienle, and B. Wagner: Identifying and overcoming the interface originating c-axis instability in highly Sc enhanced AlN for piezoelectric micro-electromechanical systems, *J. Appl. Phys.* **122**(3), 035301 (2017). DOI: https://doi.org/10.1063/1.4993908.

15. G. Wingqvist, F. Tasnádi, A. Zukauskaite, J. Birch, H. Arwin, and L. Hultman: Increased electromechanical coupling in w-$Sc_xAl_{1-x}N$, *Appl. Phys. Lett.* **97**(11), 1 (2010). DOI: https://doi.org/10.1063/1.3489939.

16. R. Deng, S. R. Evans, and D. Gall: Bandgap in $Al_{1-x}Sc_xN$, *Appl. Phys. Lett.* **102**(11), 112103 (2013). DOI: https://doi.org/10.1063/1.4795784.

17. F. Tasnádi, B. Alling, C. Höglund, G. Wingqvist, J. Birch, L. Hultman, and I. A. Abrikosov: Origin of the Anomalous Piezoelectric Response in Wurtzite $Sc_{(x)}Al_{(1-x)}N$ Alloys, *Phys. Rev. Lett.* **104**(13), 137601 (2010). DOI: https://doi.org/10.1103/PhysRevLett.104.137601.

18. S. Fichtner, N. Wolff, F. Lofink, L. Kienle, and B. Wagner: AlScN: A III-V semiconductor based ferroelectric, *J. Appl. Phys.* **125**(11), 114103 (2019). DOI: https://doi.org/10.1063/1.5084945.

19. C. S. Sandu, F. Parsapour, S. Mertin, V. Pashchenko, R. Matloub, T. LaGrange, B. Heinz, and P. Muralt: Abnormal Grain Growth in AlScN Thin Films Induced by Complexion Formation at Crystallite Interfaces, *Phys. status solidi* **216**(2), 1800569 (2019). DOI: https://doi.org/10.1002/pssa.201800569.

20. S. Franssila: Introduction to Microfabrication, 2nd ed. (John Wiley & Sons, Ltd, Chichester, UK, 2010).

21. S. Lamichhane: Thermally Induced Activation Energy of Crystalline Silicon in Alkaline Solution, *Nepal J. Sci. Technol.* **11**(November), 215 (2010). DOI: https://doi.org/10.3126/njst.v11i0.4148.

22. K. Nojiri: Dry Etching Technology for Semiconductors (Springer International publishing, Swizerland, 2015).

23. P. F. Williams, editor : Plasma Processing of Semiconductors (Springer, Dordrecht, 1997).

24. E. Österlund: Deposition and Characterization of Aluminum Nitride Thin Films for Piezoelectric MEMS, doctoral dissertation, Aalto University, 2020.

25. S. Yoshida, S. Misawa, Y. Fujii, S. Takada, H. Hayakawa, S. Gonda, and A. Itoh: Reactive molecular beam epitaxy of aluminium nitride, *J. Vac. Sci. Technol.* **16**(4), 990 (1979). DOI: https://doi.org/10.1116/1.570166.

26. A. K. Sharma and R. K. Thareja: Pulsed laser ablation of aluminum in the presence of nitrogen: Formation of aluminum nitride, *J. Appl. Phys.* **88**(12), 7334 (2000). DOI: https://doi.org/10.1063/1.1329353.

27. S. Leone, J. Ligl, C. Manz, L. Kirste, T. Fuchs, H. Menner, M. Prescher, J. Wiegert, A. Žukauskaitė, R. Quay, and O. Ambacher: Metal-Organic Chemical Vapor Deposition of Aluminum Scandium Nitride, *Phys. status solidi – Rapid Res. Lett.* **14**(1), 1900535 (2020). DOI: https://doi.org/10.1002/pssr.201900535.

28. M. Park, Z. Hao, R. Dargis, A. Clark, and A. Ansari: Epitaxial Aluminum Scandium Nitride Super High Frequency Acoustic Resonators, *J. Microelectromechanical Syst.* **29**(4), 490 (2020). DOI: https://doi.org/10.1109/JMEMS.2020.3001233.

29. M. T. Hardy, B. P. Downey, N. Nepal, D. F. Storm, D. S. Katzer, and D. J. Meyer: (Invited) ScAlN: A Novel Barrier Material for High Power GaN-Based RF Transistors, *ECS Trans.* **80**(7), 161 (2017). DOI: https://doi.org/10.1149/08007.0161ecst.

30. S. Fichtner, T. Reimer, S. Chemnitz, F. Lofink, and B. Wagner: Stress controlled pulsed direct current co-sputtered $Al_{1-x}Sc_xN$ as piezoelectric phase for micromechanical sensor applications, *APL Mater.* **3**(11), 116102 (2015). DOI: https://doi.org/10.1063/1.4934756.

31. C. S. Sandu, F. Parsapour, D. Xiao, R. Nigon, L. M. Riemer, T. LaGrange, and P. Muralt: Impact of negative bias on the piezoelectric properties through the incidence of abnormal oriented grains in $Al_{0.62}Sc_{0.38}N$ thin films, *Thin Solid Films* **697**(January), 137819 (2020). DOI: https://doi.org/10.1016/j.tsf.2020.137819.

32. C. Liu, B. Chen, M. Li, Y. Zhu, and N. Wang: Evaluation of the Impact of Abnormally Orientated Grains on the Performance of ScAlN-based Laterally Coupled Alternating Thickness (LCAT) Mode Resonators and Lamb Wave Mode Resonators, in *2020 IEEE International Ultrasonics Symposium (IUS)* (2020) . DOI: https://doi.org/10.1109/IUS46767.2020.9251507.

33. T. Riekkinen, A. Nurmela, J. Molarius, T. Pensala, P. Kostamo, M. Ylilammi, and S. van Dijken: Influence of the seed layer on structural and electro-acoustic properties of sputter-deposited AlN resonators, *Thin Solid Films* **517**, 6588 (2009). DOI: https://doi.org/10.1016/j.tsf.2009.04.060

34. T. Kamohara, M. Akiyama, N. Ueno, and N. Kuwano: Improvement in crystal orientation of AlN thin films prepared on Mo electrodes using AlN interlayers, *Ceram. Int.* **34**(4), 985 (2008). DOI: https://doi.org/10.1016/j.ceramint.2007.09.051.

35. P. B. Barna and M. Adamik: Growth mechanisms of polycrystalline thin films, in *Science*

and Technology of Thin Films (WORLD SCIENTIFIC, 1995), pp. 1–28 . DOI: https://doi.org/10.1142/9789814261425_0001.

36. J. A. Thornton: Influence of Apparatus Geometry and Deposition Conditions on the Structure and Topography of Thick Sputtered Coatings., *J Vac Sci Technol* **11**(4), 666 (1974). DOI: https://doi.org/10.1116/1.1312732.

37. J. A. Thornton: Structure-Zone Models Of Thin Films, in *Proc. SPIE 821, Modeling of Optical Thin Films* (1988), p. 95 . DOI: https://doi.org/10.1117/12.941846.

38. H. Okumura: Fabrication of an AlN ridge structure using inductively coupled Cl_2/BCl_3 plasma and a TMAH solution, *Jpn. J. Appl. Phys.* **58**(2), 3 (2019). DOI: https://doi.org/10.7567/1347-4065/aaf78b.

39. V. Bliznetsov, B. H. Bin Johari, M. T. Chentir, W. H. Li, L. Y. Wong, S. Merugu, X. L. Zhang, and N. Singh: Improving aluminum nitride plasma etch process for MEMS applications, *J. Micromechanics Microengineering* **23**(11), 117001 (2013). DOI: https://doi.org/10.1088/0960-1317/23/11/117001.

40. F. A. Khan, L. Zhou, V. Kumar, I. Adesida, and R. Okojie: High rate etching of AlN using BCl_3/Cl_2/Ar inductively coupled plasma, *Mater. Sci. Eng. B Solid-State Mater. Adv. Technol.* **95**(1), 51 (2002). DOI: https://doi.org/10.1016/S0921-5107(02)00160-5.

41. H. S. Kim, D. H. Lee, J. W. Lee, T. I. Kim, and G. Y. Yeom: Effects of plasma conditions on the etch properties of AlGaN, *Vacuum* **56**(1), 45 (2000). DOI: https://doi.org/10.1016/S0042-207X(99)00156-6.

42. X. Liu, C. Sun, B. Xiong, L. Niu, Z. Hao, Y. Han, and Y. Luo: Smooth etching of epitaxially grown AlN film by Cl_2/BCl_3/Ar-based inductively coupled plasma, *Vacuum* **116**, 158 (2015). DOI: https://doi.org/10.1016/j.vacuum.2015.03.030.

43. W. Guo, J. Xie, C. Akouala, S. Mita, A. Rice, J. Tweedie, I. Bryan, R. Collazo, and Z. Sitar: Comparative study of etching high crystalline quality AlN and GaN, *J. Cryst. Growth* **366**, 20 (2013). DOI: https://doi.org/10.1016/j.jcrysgro.2012.12.141.

44. J. Jasinski, Z. Liliental-Weber, Q. S. Paduano, and D. W. Weyburne: Inversion domains in AlN grown on (0001) sapphire, *Appl. Phys. Lett.* **83**(14), 2811 (2003). DOI: https://doi.org/10.1063/1.1616191.

45. W. Guo, R. Kirste, I. Bryan, Z. Bryan, L. Hussey, P. Reddy, J. Tweedie, R. Collazo, and

Z. Sitar: KOH based selective wet chemical etching of AlN, $Al_xGa_{1-x}N$, and GaN crystals: A way towards substrate removal in deep ultraviolet-light emitting diode, *Appl. Phys. Lett.* **106**(8), 1 (2015). DOI: https://doi.org/10.1063/1.4913705.

46. S. Saravanan, E. Berenschot, G. Krijnen, and M. Elwenspoek: A novel surface micromachining process to fabricate AlN unimorph suspensions and its application for RF resonators, *Sensors Actuators A Phys.* **130**–**131**(SPEC. ISS.), 340 (2006). DOI: https://doi.org/10.1016/j.sna.2005.09.029.

47. S. M. Tanner and V. V. Felmetsger: Microstructure and chemical wet etching characteristics of AlN films deposited by ac reactive magnetron sputtering, *J. Vac. Sci. Technol. A Vacuum, Surfaces, Film.* **28**(1), 69 (2010). DOI: https://doi.org/10.1116/1.3268620.

48. S. Marauska, V. Hrkac, T. Dankwort, R. Jahns, H. J. Quenzer, R. Knöchel, L. Kienle, and B. Wagner: Sputtered thin film piezoelectric aluminum nitride as a functional MEMS material, *Microsyst. Technol.* **18**(6), 787 (2012). DOI: https://doi.org/10.1007/s00542-012-1493-1.

49. I. Cimalla, C. Foerster, V. Cimalla, V. Lebedev, D. Cengher, and O. Ambacher: Wet chemical etching of AlN in KOH solution, *Phys. Status Solidi Curr. Top. Solid State Phys.* **3**(6), 1767 (2006). DOI: https://doi.org/10.1002/pssc.200565206.

50. C. B. Vartuli, J. W. Lee, J. D. MacKenzie, S. J. Pearton, C. R. Abernathy, J. C. Zolper, R. J. Shul, and F. Ren: Chemical Etching of AlN and InAlN in KOH Solutions, *J. Electrochem. Soc.* **449**, 1017 (1996). DOI: https://doi.org/10.1557/PROC-449-1017.

51. J. R. Mileham, S. J. Pearton, C. R. Abernathy, J. D. MacKenzie, R. J. Shul, and S. P. Kilcoyne: Patterning of AlN, InN, and GaN in KOH-based solutions, *J. Vac. Sci. Technol. A Vacuum, Surfaces, Film.* **14**(3), 836 (1996). DOI: https://doi.org/10.1116/1.580399.

52. A. Ababneh, H. Kreher, and U. Schmid: Etching behaviour of sputter-deposited aluminium nitride thin films in H_3PO_4 and KOH solutions, *Microsyst. Technol.* **14**(4–5), 567 (2008). DOI: https://doi.org/10.1007/s00542-007-0450-x.

53. M. Reiner, M. Reiss, T. Brünig, L. Knuuttila, R. Pietschnig, and C. Ostermaier: Chemical understanding and utility of H_3PO_4 etching of group-III- nitrides, *Phys. status solidi* **252**(5), 1121 (2015). DOI: https://doi.org/10.1002/pssb.201451504.

54. Y. Choi, R. Choi, and J. Kim: Selective electrochemical etching of epitaxial aluminum nitride thin film, *Appl. Surf. Sci.* **509**(September 2019), 145279 (2020). DOI: https://doi.org/10.1016/j.apsusc.2020.145279.

55. Y. ha Choi, K. H. Baik, R. Choi, J. Oh, and J. Kim: Photo-Enhanced Acid Chemical Etching of High-Quality Aluminum Nitride Grown by Metal-Organic Chemical Vapor Deposition, *ECS J. Solid State Sci. Technol.* **8**(3), N42 (2019). DOI: https://doi.org/10.1149/2.0051903jss.

56. L. Colombo, A. Kochhar, C. Xu, G. Piazza, S. Mishin, and Y. Oshmyansky: Investigation of 20% Scandium-doped Aluminum Nitride films for MEMS laterally vibrating resonators, in *2017 IEEE International Ultrasonics Symposium (IUS)* (IEEE, 2017), pp. 1–1 . DOI: https://doi.org/10.1109/ULTSYM.2017.8092916.

57. Q. Wang, Y. Lu, S. Mishin, Y. Oshmyansky, and D. A. Horsley: Design, Fabrication, and Characterization of Scandium Aluminum Nitride-Based Piezoelectric Micromachined Ultrasonic Transducers, *J. Microelectromechanical Syst.* **26**(5), 1132 (2017). DOI: https://doi.org/10.1109/JMEMS.2017.2712101.

58. Y. Kusano, I. Ishii, T. Kamiya, A. Teshigahara, G.-L. Luo, and D. A. Horsley: High-SPL Air-Coupled Piezoelectric Micromachined Ultrasonic Transducers Based on 36% ScAlN Thin-Film, *IEEE Trans. Ultrason. Ferroelectr. Freq. Control* **66**(9), 1488 (2019). DOI: https://doi.org/10.1109/TUFFC.2019.2921983.

59. P. M. Mayrhofer, E. Wistrela, M. Kucera, A. Bittner, and U. Schmid: Fabrication and characterisation of ScAlN -based piezoelectric MEMS cantilevers, in *2015 Transducers - 2015 18th International Conference on Solid-State Sensors, Actuators and Microsystems (TRANSDUCERS)* (IEEE, 2015), pp. 2144–2147 . DOI: https://doi.org/10.1109/TRANSDUCERS.2015.7181383.

60. T. N. Kreutzer, S. Fichtner, B. Wagner, and F. Lofink: A double-layer MEMS actuator based on ferroelectric polarization inversion in AlScN, in *IEEE International Symposium on Applications of Feeroelectric, ISAF 2021* (IEEE, 2021), pp. 2021–2023 . DOI: https://doi.org/10.1109/ISAF51943.2021.9477382.

61. K. Bespalova, E. Osterlund, G. Ross, M. Paulasto-Krockel, A. T. Sebastian, C. B. Karuthedath, S. Mertin, and T. Pensala: Characterization of AlScN-Based Multilayer Systems for Piezoelectric Micromachined Ultrasound Transducer (pMUT) Fabrication,

J. Microelectromechanical Syst. **30**(2), 290 (2021). DOI: https://doi.org/10.1109/JMEMS.2021.3056928.

62. L. A. Pasechnik, A. G. Shirokova, O. V. Koryakova, N. A. Sabirzyanov, and S. P. Yatsenko: Complexing properties of scandium(III) in alkaline medium, *Russ. J. Appl. Chem.* **77**(7), 1070 (2004). DOI: https://doi.org/10.1023/B:RJAC.0000044150.12253.3d.

63. R. C. Vickery: Scandium Hydroxide and Scandate Ions., *J. Chem. Soc.* 251 (1955).

64. P. A. Nikolaychuk: The Revised Potential-pH Diagram of the Sc-H2O System, *Научные ведомости Белгородского государственного университета. Серия: Естественные науки* **25**(37), 70 (2016).

65. C. C. W. Ruppel: Acoustic Wave Filter Technology–A Review, *IEEE Trans. Ultrason. Ferroelectr. Freq. Control* **64**(9), 1390 (2017). DOI: https://doi.org/10.1109/TUFFC.2017.2690905.

66. T. Omori, Y. Tanaka, K. Hashimoto, and M. Yamaguchi: Synthesis of frequency response for wideband SAW ladder type filters, *Proc. - IEEE Ultrason. Symp.* 2574 (2007). DOI: https://doi.org/10.1109/ULTSYM.2007.648.

67. T. Pensala: Thin Film Bulk Acoustic Wave Devices Performance Optimization and Modeling, doctoral dissertation, VTT Publications, 2011.

68. R. Aigner: SAW and BAW technologies for RF filter applications: A review of the relative strengths and weaknesses, in *2008 IEEE Ultrasonics Symposium* (IEEE, 2008), pp. 582–589 . DOI: https://doi.org/10.1109/ULTSYM.2008.0140.

69. A. Ding, M. Reusch, Y. Lu, N. Kurz, R. Lozar, T. Christoph, R. Driad, O. Ambacher, and A. Zukauskaite: Investigation of Temperature Characteristics and Substrate Influence on AlScN-Based SAW Resonators, in *2018 IEEE International Ultrasonics Symposium (IUS)* (IEEE, 2018), pp. 1–9 . DOI: https://doi.org/10.1109/ULTSYM.2018.8579751.

70. W. Wang, P. M. Mayrhofer, X. He, M. Gillinger, Z. Ye, X. Wang, A. Bittner, U. Schmid, and J. K. Luo: High performance AlScN thin film based surface acoustic wave devices with large electromechanical coupling coefficient, *Appl. Phys. Lett.* **105**(13), 1 (2014). DOI: https://doi.org/10.1063/1.4896853.

71. M. F. Hribšek, D. V. Tošić, and M. R. Radosavljević: Surface acoustic wave sensors in mechanical engineering, *FME Trans.* **38**(1), 11 (2010).

72. M. Gillinger, T. Knobloch, M. Schneider, and U. Schmid: Harsh Environmental Surface Acoustic Wave Temperature Sensor Based on Pure and Scandium doped Aluminum Nitride on Sapphire, in *Eurosensors 2017 Proceedings* (2017), p. 341 . DOI: https://doi.org/10.3390/proceedings1040341.

73. D. B. Go, M. Z. Atashbar, Z. Ramshani, and H. C. Chang: Surface acoustic wave devices for chemical sensing and microfluidics: A review and perspective, *Anal. Methods* **9**(28), 4112 (2017). DOI: https://doi.org/10.1039/c7ay00690j.

74. J. Devkota, P. R. Ohodnicki, and D. W. Greve: SAW sensors for chemical vapors and gases, *Sensors (Switzerland)* **17**(4), 13 (2017). DOI: https://doi.org/10.3390/s17040801.

75. Y. Zhang, J. Luo, A. J. Flewitt, Z. Cai, and X. Zhao: Film bulk acoustic resonators (FBARs) as biosensors: A review, *Biosens. Bioelectron.* **116**(February), 1 (2018). DOI: https://doi.org/10.1016/j.bios.2018.05.028.

76. T. Nan, Y. Hui, M. Rinaldi, and N. X. Sun: Self-biased 215MHz magnetoelectric NEMS resonator for ultra-sensitive DC magnetic field detection, *Sci. Rep.* **3**, 1 (2013). DOI: https://doi.org/10.1038/srep01985.

77. Y. Hui, J. S. Gomez-Diaz, Z. Qian, A. Alù, and M. Rinaldi: Plasmonic piezoelectric nanomechanical resonator for spectrally selective infrared sensing, *Nat. Commun.* **7**, 1 (2016). DOI: https://doi.org/10.1038/ncomms11249.

78. X. Bian, H. Jin, X. Wang, S. Dong, G. Chen, J. K. Luo, M. J. Deen, and B. Qi: UV sensing using film bulk acoustic resonators based on Au/n-ZnO/piezoelectric-ZnO/Al structure, *Sci. Rep.* **5**(0002), 1 (2015). DOI: https://doi.org/10.1038/srep09123.

79. MEMS resonator, https://www.murata.com/products/timingdevice/mems-r, accessed 16.9.2021.

80. SiT1252 Embedded MEMS Resonator for Real Time Clocking, https://www.sitime.com/support/resource-library/product-briefs/sit1252-embedded-mems-resonator-real-time-clocking, accessed 16.9.2021.

81. S. E. Alper, K. Azgin, and T. Akin: High-Performance SOI-MEMS Gyroscope with Decoupled Oscillation Modes, in *19th IEEE International Conference on Micro Electro*

Mechanical Systems (IEEE, 2006), pp. 70–73 . DOI: https://doi.org/10.1109/MEMSYS.2006.1627738.

82. D. E. Dausch, K. H. Gilchrist, J. B. Carlson, S. D. Hall, J. B. Castellucci, and O. T. von Ramm: In vivo real-time 3-D intracardiac echo using PMUT arrays, *IEEE Trans. Ultrason. Ferroelectr. Freq. Control* **61**(10), 1754 (2014). DOI: https://doi.org/10.1109/TUFFC.2014.006452.

83. Y. Lu, H. Tang, S. Fung, Q. Wang, J. M. Tsai, M. Daneman, B. E. Boser, and D. A. Horsley: Ultrasonic fingerprint sensor using a piezoelectric micromachined ultrasonic transducer array integrated with complementary metal oxide semiconductor electronics, *Appl. Phys. Lett.* **106**(26) (2015). DOI: https://doi.org/10.1063/1.4922915.

84. C. B. Karuthedath, A. T. Sebastian, J. Saarilahti, T. Sillanpaa, and T. Pensala: Design and Fabrication of Aluminum Nitride Piezoelectric Micromachined Ultrasonic Transducers for Air Flow Measurements, in *2019 IEEE International Ultrasonics Symposium (IUS)* (IEEE, 2019), pp. 2489–2492 . DOI: https://doi.org/10.1109/ULTSYM.2019.8925544.

85. Introducing SmartSonic™, https://invensense.tdk.com/smartsonic/, accessed 21.9.2021.

86. N. Sezer and M. Koç: A comprehensive review on the state-of-the-art of piezoelectric energy harvesting, *Nano Energy* **80**(August 2020), 105567 (2021). DOI: https://doi.org/10.1016/j.nanoen.2020.105567.

87. Y. Liu, B. Hu, Y. Cai, J. Zhou, W. Liu, A. Tovstopyat, G. Wu, and C. Sun: Design and Performance of ScAlN/AlN Trapezoidal Cantilever-Based MEMS Piezoelectric Energy Harvesters, *IEEE Trans. Electron Devices* **68**(6), 2971 (2021). DOI: https://doi.org/10.1109/TED.2021.3072612.

88. P. M. Mayrhofer, C. Rehlendt, M. Fischeneder, M. Kucera, E. Wistrela, A. Bittner, and U. Schmid: ScAlN MEMS Cantilevers for Vibrational Energy Harvesting Purposes, *J. Microelectromechanical Syst.* **26**(1), 102 (2017). DOI: https://doi.org/10.1109/JMEMS.2016.2614660.

89. E. Yarar, Di. Meyners, E. Quandt, S. Fichtner, P. Hayes, A. Piorra, T. Reimer, T. Lisec, P. Frank, B. Wagner, and F. Lofink: MEMS-Based AlScN Resonating Energy Harvester With Solidified Powder Magnet, *J. Microelectromechanical Syst.* **28**(6), 1019 (2019). DOI: https://doi.org/10.1109/JMEMS.2019.2945550.

90. Digital micromirror yields bright array of colors, https://www.laserfocusworld.com/optics/article/16548723/digital-micromirror-yields-bright-array-of-colors, accessed 21.9.2021.

91. T. Pensala, J. Kiihamaki, J. Kyynarainen, J. Dekker, S. Gorelick, P. Pekko, T. Pernu, O. Ylivaara, F. Gao, and D. Morits: Wobbling Mode AlN-Piezo-MEMS Mirror Enabling 360-Degree Field of View LIDAR for Automotive Applications, in *2019 IEEE International Ultrasonics Symposium (IUS)* (IEEE, 2019), pp. 1977–1980 . DOI: https://doi.org/10.1109/ULTSYM.2019.8925660.

92. S. Gu-Stoppel, T. Lisec, M. Claus, N. Funck, S. Fichtner, S. Schröder, B. Wagner, and F. Lofink: A triple-wafer-bonded AlScN driven quasi-static MEMS mirror with high linearity and large tilt angles, in *MOEMS and Miniaturized Systems XIX*, edited by W. Piyawattanametha, Y.-H. Park, and H. Zappe (SPIE, 2020), p. 3 . DOI: https://doi.org/10.1117/12.2542800.

93. P. M. Mayrhofer, P. O. Å. Persson, A. Bittner, and U. Schmid: Properties of $Sc_xAl_{1-x}N$ (x = 0.27) thin films on sapphire and silicon substrates upon high temperature loading, *Microsyst. Technol.* **22**(7), 1679 (2016). DOI: https://doi.org/10.1007/s00542-015-2798-7.

94. P. H. Chen, S. Wu, Y. C. Chen, J. L. Huang, D. F. Lii, and Z. X. Lin: Microstructure and piezoelectric properties of c-axis ScAlN films on the Y-128° $LiNbO_3$ substrate, *Surf. Coatings Technol.* **284**, 129 (2015). DOI: https://doi.org/10.1016/j.surfcoat.2015.08.078.

95. M. Clement, V. F. Jimena Olivares, T. Mirea, J. Olivares, and E. Iborra: Effects of Post-Deposition Vacuum Annealing on the Piezoelectric Properties of AlScN Thin Films Sputtered on 200 mm Production Wafers, in *2018 IEEE International Ultrasonics Symposium (IUS)* (2018) . DOI: https://doi.org/10.1109/ULTSYM.2018.8580177.

96. M. Li, B. Chen, J. Xie, W. Song, and Y. Zhu: Effects of post-annealing on texture evolution of sputtered ScAlN films, in *2020 IEEE International Ultrasonics Symposium (IUS)* (2020) . DOI: https://doi.org/10.1109/IUS46767.2020.9251741.